The Nanostructure of Implant-Induced Fibrosis

Jasminder Kaur Satnam Singh

A thesis submitted to the University of London for the
degree of Master of Philosophy

Supervised by Dr. Himadri S. Gupta

February 2013

School of Engineering and Materials Science

Queen Mary, University of London

Abstract

Fibrosis or the formation of fibrotic tissue is a product of chronic inflammatory reactions induced by a variety of stimuli and occurs when there is a dysfunction in the wound healing process. This typically ensues following mechanical trauma, tissue injury, surgical intervention or implantation. Quantitative analysis of the developing collagen architecture of fibrotic tissue is an important, but so far almost neglected aspect of wound healing research.

Synchrotron X-ray scattering and diffraction techniques are ideally suited for studying structural changes in nanostructured biological tissues. The work presented in this thesis demonstrates the application of a novel technique (microfocus synchrotron scanning Small Angle X-ray Scattering (SAXS) and Wide Angle X-ray Diffraction (WAXD)) in characterizing the presence of collagenous tissue in fibrotic tissue formed surrounding subcutaneous implants. The results of a single (representative) implant type and time point is presented to demonstrate proof-of-principle of the novel technique. This work provides information, for the first time on fibrotic tissue, the nanoscale anisotropy in fibril orientation, the length scale of nanofibrils, the extension of the tropocollagen molecules, and the degree of molecular orientation and crystallinity. These results are, to the best of my knowledge, the first SAXS-model for fibrotic tissue nanostructure and will be the foundation on which subsequent work can be based.

It has been shown that, combining microfocus spatial resolution and the quantitative potential of X-ray scattering and diffraction is a suitable approach for characterizing the hierarchical structure of fibrotic tissue in the nanometre and micrometre scales simultaneously.

Acknowledgements

This thesis could not have been completed without the generous support and encouragement from a multitude of people. A heartfelt appreciation goes to my supervisor, Dr Himadri Shikhar Gupta for his patience, guidance and unwavering encouragement during my entire project. A special word of gratitude goes to my collaborator from the Brunel Institute of Bioengineering, Dr Krishna Burugapalli who provided all the samples examined in this thesis, as well as guidance with the histological aspect of it.

I would also like to express my thanks to the support staff at Queen Mary, University of London. A special thanks to Mr Dougie Thomson from the School of Engineering and Materials Science for his support in designing and manufacturing the micromechanical tester. Also to Dr Michaela Egertova from the School of Biological and Chemical Sciences for providing a great deal of assistance and guidance with sample preparation, without which the experiments would not be possible.

I am most appreciative to Diamond Light Source for supporting the synchrotron experiments; especially Dr Jennifer Hiller, the I22 beamline scientist who provided so much support before and during the synchrotron experiments.

I am grateful to Queen Mary, University of London for the financial support and resources provided which led to the completion of this thesis.

I would also like to thank my family and friends who kept me sane over the past three years. To my brother Ranveer, thank you for believing in me. Special and heartfelt thanks to Umabalan, who has shown me how wonderful life can be. And most importantly, my grateful thanks to my husband, Deepak, who has stood by me and whose love and support will never be forgotten.

A short but significant mention of thanks to God for without His blessings I would not be here.

Table of Contents

List of Figures

List of Tables

List of Abbreviations

AGAG	Anionic glycosaminoglycans
ALCAP	Aluminum calcium phosphate
bFGF	Basic fibroblast growth factor
ECM	Extracellular matrix
ePTFE	Expanded polytetrafluoroethylene
FACIT	Fibril-associated collagen with interrupted triple helices
FBR	Foreign body response
GAG	Glycosaminoglycan
HA	Hydroxyapatite
ILD	Interstitial lung disease
IP	Intraperitoneal
IPF	Idiopathic pulmonary fibrosis
MACIT	Membrane-associated collagen with interrupted triple helices
MI	Myocardial infarction
MULTIPLEXIN	Multiple triple-helix domains and interruptions
PBS	Phosphate buffered saline
PC	Phosphorylcholine

PDGF	Platelet-derived growth factor
PDMS	Polydimethylsiloxane
PEO	Polyethylene oxide
PG	Proteoglycan
PLL	Poly-L-lycine
PU	Polyurethane
PU-S-PEO	Polyurethane with silicone and polyethylene oxide
PVA	Polyvinyl alcohol
SAXD	Small angle X-ray diffraction
SAXS	Small angle X-ray scattering
SC	Subcutaneous
SLRP	Small leucine-rich repeat proteoglycan
TCP	Tricalcium phosphate
TGF-β	Transforming growth factor-beta
VEGF	Vascular endothelial cell growth factor
WAXD	Wide angle X-ray diffraction

1 Introduction

1.1 What is Fibrosis?

Fibrosis or the formation of fibrotic tissue occurs when there is a dysfunction in the wound healing process, such as follows an injury, surgical intervention or implantation. Fibrotic tissue is characterized by a dense collagen-rich extracellular matrix (ECM) which is distinct (structurally and compositionally) to the ECM of normal functional connective tissue types like skin. Occurrence of fibrosis during the healing process can lead to severe lifelong disabilities, with an estimated socio-economic cost of the order of tens of billions of dollars[1]. Fibrosis occurs in a wide range of instances, including myocardial infarction, liver and lung cirrhosis [1], hypertrophic scars due to burn injuries and surgical procedures [2], and in implant/ tissue interfaces [3-7]. Therefore, preventing fibrosis is of great interest in wound repair, regenerative medicine, plastic surgery and implant design [1, 8].

To understand the dysfunctional changes induced by fibrosis, consider two examples. In the case of myocardial infarction (MI), there is damage to the heart wall, typically to the left ventricular chamber which supplies the vital organs with blood. The formation of fibrosis post-MI is detrimental to ventricular function as it impairs mechano-electric coupling of cardiomyocytes (cardiac muscle cells) resulting in congestive heart failure and/or abnormal heart rhythms (arrhythmias) [1, 9-11].

In a second example, liver cirrhosis is an irreversible result of fibrous scarring [12]. Liver fibrosis can occur due to a variety of reasons, including heavy alcohol use, drug abuse, and chronic viral infections including hepatitis [12-13]. Advanced liver fibrosis results in the development of nodules of regenerating hepatocytes, which defines cirrhosis. This in turn produces hepatocellular dysfunction leading to hepatic insufficiency and increased intrahepatic resistance to blood flow resulting in portal hypertension [14-15]. Cirrhosis of the lung (more commonly

known as pulmonary fibrosis) is an age-related lung disease of unknown cause [16] and is characterized by the increase in fibrous tissue throughout the lungs leading to thickening of the alveolar wall making it more difficult to breathe [17].

The implantation of a material (biomaterial) into the body results in a tissue response similar to that seen in wound healing. These materials include cochlear implants, breast implants, drug delivery devices, sensors, prosthesis, hip implants, pacemakers, cardioverter defibrillators and stents. Following implantation surgery, the initial granulation tissue is progressively replaced by collagen and fibroblast-rich fibrotic tissue [18] which undergo controlled developmental changes in size, biochemistry and structure. These changes lead to either resolution (restoration of nonfibrotic tissue) or accumulation of a collagen-dense hypertrophic scar.

Despite major advances in understanding the biochemical aspects of wound healing, little is known about the collagen architecture in the fibrotic tissue which has a distinctive nanostructure compared to normal soft collageneous tissues.

1.2 Synchrotron X-ray Scattering and Diffraction Approach

The conventional technique of real-space imaging using X-rays (such as microradiography) is not capable to resolve structures at the nanometre scale. Using synchrotron X-ray scattering and diffraction, non-destructive quantification of nanostructures in biological systems is possible. High photon flux levels enable short (second to millisecond) X-ray exposure times. Small angle X-ray scattering (SAXS) and wide angle X-ray diffraction (WAXD) measurements, in combination with scanning and microfocusing optics [19] allow the construction of quantitative images of nanostructural parameters with micrometre scanning resolution; making this technique ideally suited for studying nano- and microscale structural changes in anisotropic and inhomogeneous human tissue in which direct spatial resolution is desired.

1.3 Aim and Outline of this Thesis

Quantitative analysis of the developing collagen architecture in healing tissue is an essential, but so far almost neglected aspect of wound healing research. The aim of this work is to provide fundamental understanding of the nano- and microscale structure at the fibrillar level of the fibrotic layer. To achieve this aim, the fibrillar and extrafibrillar architecture of the fibrotic tissue in subcutaneous implants will be characterized quantitatively using high brilliance synchrotron scanning X-ray scattering and diffraction. The nanoscale anisotropy in fibril orientation, the length scale of nanofibrils, the extension of the tropocollagen molecules, and the degree of molecular orientation and crystallinity will be determined. The model system used is of implants in the subcutaneous layer of a murine model (Sprague-Dawley rats). This work will be, to the best of my knowledge, the first to combine microfocus spatial resolution and the quantitative potential of synchrotron X-ray scattering and diffraction techniques to characterize fibrotic tissue formed surrounding subcutaneous implants.

Chapter 2 presents a review of the structure of collagen and the components of the extracellular matrix of soft connective tissues including proteoglycans and elastin. **Chapter 3** gives an overview of normal cutaneous wound healing process and discusses fibrosis from a clinical viewpoint. Implant-induced fibrosis, which is of significant relevance to this thesis, will be discussed. This chapter will also review the current understanding of X-ray scattering and diffraction of fibrotic tissue.

Chapter 4 describes the materials and experimental methods used in this study including sample preparation method, principles of X-ray scattering and the design of synchrotron scanning and in situ X-ray scattering experiments, as well as a background on synchrotron. The design and development of a micromechanical testing rig which will be crucial for future studies into understanding the biophysical aspect of fibrotic tissue is also discussed.

In the next part of this thesis, in **Chapter 5**, the results of the nano- and microstructure analysis of fibrotic tissue are reported and discussed. The last part of this thesis, **Chapter 6** and **Chapter 7**, deal with the conclusions and recommended future work.

2 The Molecular and Supramolecular Components of Soft Connective Tissues

Soft connective tissues, such as tendon, skin, cartilage, ligament and arterial walls, are comprised of proteins including collagen, elastin, fibrillin, proteoglycans (PG) and water [20-23]. These components can vary significantly in their supramolecular architecture and mechanical properties. Connective tissue ECMs cope with tensile and compressive mechanical stresses. Tension is resisted by protein fibres such as collagen and elastin while compression is opposed by water soluble PGs [24]. Collagen is relatively stiff and crystalline [20] whereas elastin and fibrillin are less stiff, amorphous and rubbery [25]. The amorphous ground substance in the ECM consists of proteoglycans (e.g. aggrecan and decorin) in unmineralized collagen, and osteocalcin and osteopontin in mineralized collagen [26-27]. Proteoglycans are highly amorphous, negatively charged, hydrated and appear gel-like [22]. As skin and subcutaneous tissue which is the focus of this thesis are comprised of collagen, proteoglycans and elastin, discussion in this section will be focused on describing these normal building blocks.

2.1 Collagen

Collagen, the English adaptation of the Greek word *kollagene,* (meaning glue forming) was first identified in 1865 [28]. Collagen is one of the most crucial components of the ECM with more than twenty eight different types identified so far [29]. It can be found in abundance in mammals, in tendons, ligaments, bone, skin, dentin, blood vessels, cartilage and in most ECM in general [20].

Collagen can be grouped into several classes based on their molecular structure and supramolecular assemblies - fibril-forming collagens, network-forming collagens, anchoring fibrils, fibril-associated collagen with interrupted triple helices (FACIT), membrane-associated collagen with interrupted triple helices (MACIT) and multiple triple-helix domains and

interruptions (MULTIPLEXIN) [20, 28-31]. The collagen classes, types, molecular compositions and their distribution are summarized in **Table 2.1**. Fibril-forming collagens are of most interest from a biomechanical point of view [32-33]. The classical fibril-forming collagens include; Type I, the most widely occurring collagen present in skin, bone, tendon and cornea; Type II has a more specific tissue distribution which is limited to cartilage, vitrous body and nucleus pulposus; Type III, which is present in relatively elastic tissues such as skin, blood vessels, intestine and reticular fibres of most tissues; Type V is typically found in association with Type I with large amounts present in cornea; and Type XI which found in association with Type II. In cutaneous wound healing, the predominant type of collagen is Type III which typically remodels into Type I collagen [1]. Type I collagen appear to have distinct structural features, e.g. a larger degree of internal crystallinity and a wide distribution of fibril diameters. In skin, Type I-rich fibrils typically contain around 20% (by mass) Type III collagen [20].

Regardless of the specific class or type, all collagen types have certain common features. They are formed of three polypeptide chains (α-chains) which form a triple-helical structure. In collagens Type II, III, VII, VIII, X and some others, the triple-helix might be formed by three identical α-chains (homotrimers), whereas in collagens Type I, IV, V, VI, IX and XI, the helix may be formed by two or more different chains (heterotrimers). Each α-chain is constructed largely from a repeating amino acid motif (Gly-X-Y). In this motif, Gly stands for glycine (the smallest amino acid), which occurs in every third position of the polypeptide chain, and X and Y can be any amino acid but are commonly proline and hydroxyproline. The three chains form a right-handed triple-helical structure around a central axis with glycine occupying the centre of the protein and X and Y positioned on the outer surface. Each chain is staggered by one residue from its adjacent chain to accommodate glycine residues and the three chains are held together by inter-chain hydrogen bonding [20, 23, 28-29, 31-32, 34-36].

The collagen nomenclature rules indicate that individual polypeptide chains are called α chains and are numbered in Arabic numerals for a given collagen type, which is itself indicated by Roman numerals in parentheses [28]. Fibril-forming collagen molecules can be homotrimeric, consisting of up to three identical α chains, or heterotrimeric consisting of three distinct α chains. For example, in homotrimeric collagens like Type II collagen, the chain composition is shown as $\alpha1[II]_3$, whereas in a heterotrimeric collagen like Type I collagen, it is $\alpha1[I]_2$ α2[I]. While Type I collagen only has two different α chains, Type V collagen is made up of three α chains, leading to different chain stoichiometries such as $\alpha1[V]_2$ α2[V] and α1[V] α2[V] α3[V] [20]. The length of triple-helix structures varies between collagen types. In fibril forming collagens like Type I, II and III, the triple-helix structures consist of about 1000 amino acid residues of approximately 300 nm in length [31]. These collagen molecules are staggered axially from their neighbours, leading to an effective periodicity of electron density along the axis, known as the D-periodicity which depends on the tissue as well as its physicochemical condition; collagen Type I for example is 65 nm in dry state and 67 nm when hydrated [20-21]. Collagen Type VI contains triple helices of 200 amino acids long [31] with a periodicity of 110 nm [20], whereas triple helices in collagen Type X are 460 amino acids long [31].

Figure 2.1 illustrates the molecular structure of Type I collagen with the non-collagenous domains which are an integral part of fibrillar collagens. The non-helical regions are called telopeptides, and are about 20 residues in length. Telopeptides play a crucial role in covalent cross-linking of collagen molecules and linking to other molecular structures of the surrounding matrix, which increases their tensile strength [21]. These telopeptides appear at both C-termini and N-termini. Propeptides are inactive peptides that can be turned into an active form by chemical modification. C-propeptides play an important role in the initiation of triple helix formation and are removed during the later stage of biosynthesis by specific metalloproteinases, leaving the short C-telopeptides. N-propeptides are involved in the regulation of primary fibril diameters and are completely removed leaving short N-telopeptides [20, 31]. The telopeptide in

Type III collagen are slightly shorter compared to Type I, though the length of the triple helix is slightly longer [37]. Electron density is clearest at the lateral level of telopeptides and folded telopeptides at the ends of the gap region result in the highest packing density [20].

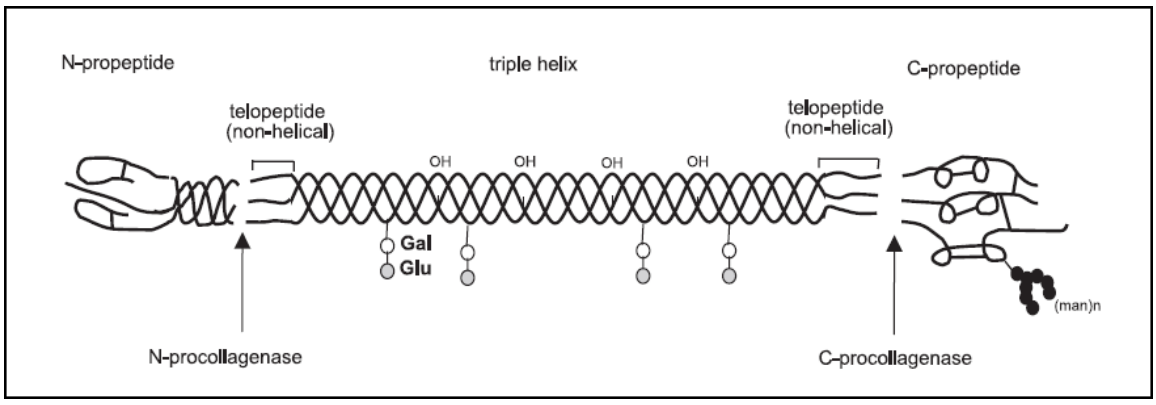

***Figure 2.1**: Type I collagen with the non-collagenous domains [31].*

However, in considering the structure of collagen, it is crucial to note that the molecular level sequence does not fully describe the resulting tissue. Collagenous tissues are hierarchically structured; take tendon for example. It is a vertebrate tissue made up of several levels of organization [20, 27, 38] as shown in **Figure 2.2**, which all contribute to its mechanical properties. At the molecular level it comprises of triple helical collagen molecules, as described above. At the nanometre level the basic building block is collagen fibril which consists of slender rod-like structures with tapered ends having a 65 - 67 nm periodicity. At the micron level it is made up of collagen fibres and fibre bundles that form fascicles [20, 27, 38-39]. The collagen fibrils in Type I collagen in tendon and skin have a wider variation in diameter, are straighter and are not in contact with mineral crystals. In bone and dentin on the other hand, collagen fibrils are rather uniform in diameter, are intertwined and are associated with discretely packed small crystals of carbonate apatite [21].

There has been evidence of a subfibrillar structure of 4 nm lateral periodicity that lies between molecular and fibrillar levels in certain fibril types [40-41]. This structure may help provide

crucial information regarding the nucleation and growth processes of fibril formation as well as improve overall fibril mechanical properties by preventing crack propagation [20]. The collagen molecules are tilted with respect to the fibril axis in fibrils found in tissues that resist uniaxial stress, such as tendon, ligament and bone [42]. A molecular tilt of approximately 18° is seen in fibrils from tissues such as skin [43] and cornea [44-45]. Fibril diameters are relatively uniform in these tissues and typically small (less than 100 nm), which result in a shortening of the axial spacing from 67 nm to 65 nm (67 cos 18°) [20].

Fibril property and morphology along with its internal organization provide important information of the collagen. The interaction between fibrils and the partner macromolecule environment are determined by collagen molecules and a variety of PGs present in the surface of the fibril. They also play a crucial role in restricting fibril growth and allowing/ restricting fibril fusion to occur. PGs interact with collagen through globular protein cores that recognize specific sequences in the collagen composition. PGs such as decorin, lumican and fibromodulin are involved in intrafibrillar connectivity and matrix-cell communication. These PGs are essential modulators of the interfacial shear between fibrils (discussed in **Section 2.2**). Decorin, lumican and fibromodulin are also known to coat the surface of fibrils and may restrict further growth. [20]. Collagen and PG interactions determine the diameter, length and the slender tapering of collagen fibrils, which in turn determine the macroscopic mechanical properties of the tissues [20]. Fibril diameter distribution has also been associated with overall mechanical properties [46]. The presence of Type III collagen is often associated with tissues with regulated fibril diameters [47]. Fibril diameters range from above a micron in tendon to below 40 nm in cornea and about 10 nm fine filaments of cartilage. Tendon contains a wide variety of fibril dimensions which may relate to the tapered nature of fibrils. Fibril size distribution is determined by the N-terminal propeptide. Although Type III collagen can be buried within the fibril, slowly processed N-terminal propeptides may persist on its surface. In collagens Type V or XI, partial removal of

the bulky propeptide units may lead to a decoration of the fibril surface with globular protein domains [20].

Collagen fibre orientation varies in different tissues. In cornea, collagen fibrils are of uniform diameter and are regularly arranged within a matrix of proteoglycans. However, the fibre direction is not uniform and is made up of superposed layers of fibrils with different orientations. This is crucial for tissue transparency [45]. In articular cartilage, collagen fibrils in the superficial zone are compactly arranged into layers of intersecting flat ribbons [48-49].

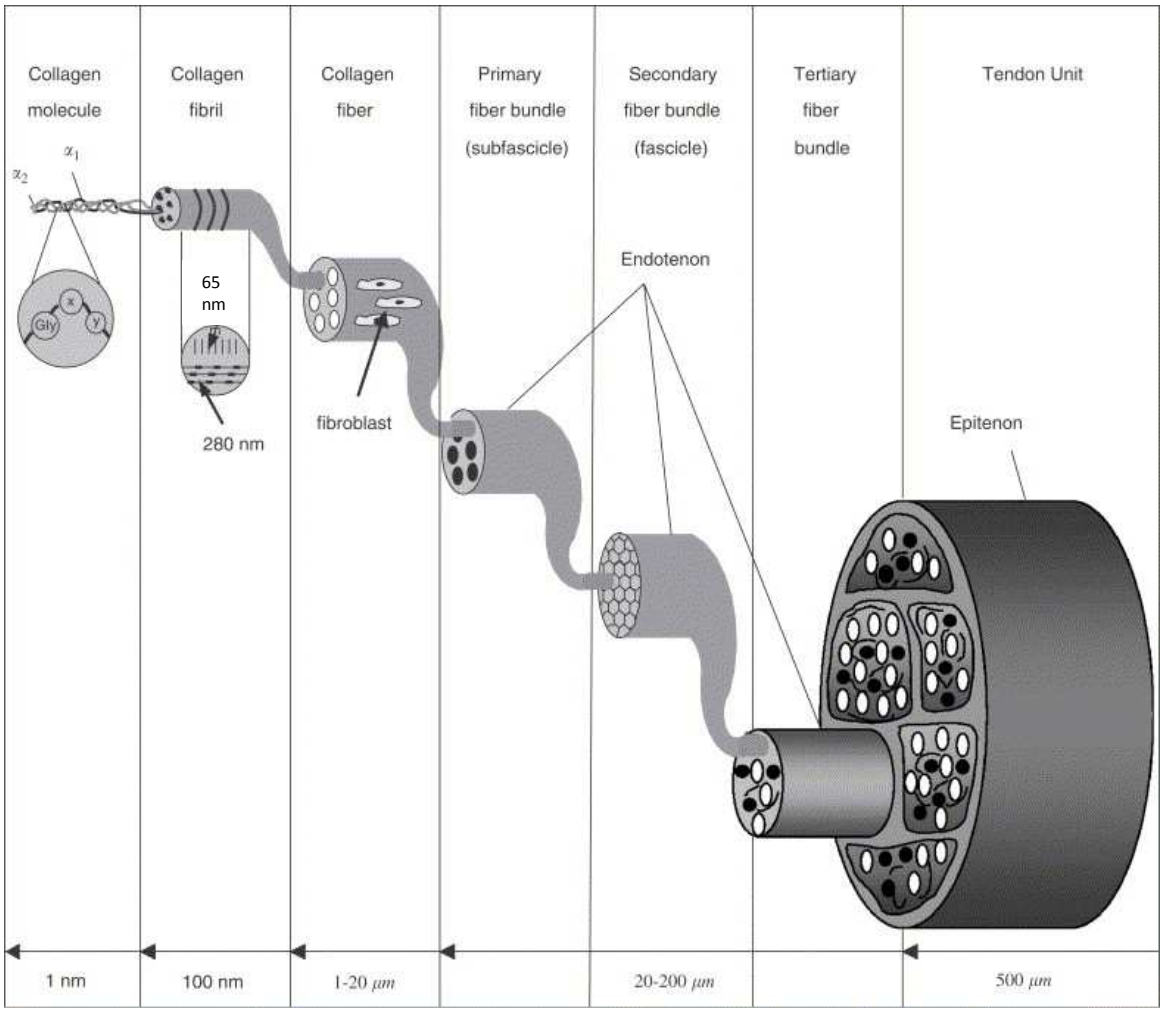

Figure 2.2*: The hierarchical structure of tendon. Collagen molecule arrangement in the fibril give a 65 nm gap in dry state and 67 nm gap in wet state [38].*

***Table 2.1**: Various collagen types as they correspond to the major collagen classes [20, 28-31].*

Class	Type	Molecular composition	Tissue distribution
Fibril-forming collagen	I	$\alpha1[I]_2\ \alpha2[I]$	Widespread: Dermis, bone ligament, tendon, cornea
	II	$\alpha1[II]_3$	Cartilage, vitreous body, nucleus pulposus
	III	$\alpha1[III]_3$	Skin, blood vessels, intestine, reticular fibres of most tissues
	V	$\alpha1[V]_3$ $\alpha1[V]_2\ \alpha2[V]$ $\alpha1[V]\ \alpha2[V]\ \alpha3[V]$	Widespread: Bone, dermis, cornea, placenta, lung
	XI	$\alpha1[XI]\ \alpha2[XI]\ \alpha3[XI]$	Cartilage, intervertebral disc, vitreous body
	XXIV	-	Bone, cornea
	XXVII	-	Cartilage
Network-forming collagen	IV	$\alpha1[IV]_2\ \alpha2[IV]$ $\alpha3[IV]\ \alpha4[IV]\ \alpha5[IV]$ $\alpha5[IV]_2\ \alpha6[IV]$	Basement membranes
	VI	$\alpha1[VI]\ \alpha2[VI]\ \alpha3[VI]$ $\alpha1[VI]\ \alpha2[VI]\ \alpha4[VI]$	Widespread: Bone, cartilage, cornea, dermis, placenta, lungs, intervertebral disc, vessel wall
	VIII	$\alpha1[VIII]_3$ $\alpha2[VIII]_3$ $\alpha1[VIII]_2\ \alpha2[VIII]$	Widespread: Dermis, brain, heart, kidney, endothelial cells
	X	$\alpha1[X]_3$	Cartilage
Anchoring fibrils	VII	$\alpha1[VII]_2\ \alpha2[VII]$	Dermis, bladder, oral muscosa, cervix
Fibril-associated collagen with interrupted triple helices (FACIT)	IX	$\alpha1[IX]\ \alpha2[IX]\ \alpha3[IX]$	Cartilage, cornea, vitreous
	XII	$\alpha1[XII]_3$	Dermis, tendon, ligament
	XIV	$\alpha1[XIV]_3$	Widespread: Bone, dermis, cartilage, tendon, placenta, vessel wall
	XVI	-	Dermis, kidney
	XIX	-	Basement membrane
	XX	-	Cornea l epithelium, tendon, embryonic skin
	XXI	-	Stomach, kidney, blood vessel wall
	XXII	-	Tissue junctions
	XXVI	-	Testis, ovary
Membrane-associated collagen with interrupted triple helices (MACIT)	XIII	-	Endothelial cells, dermis, eye, heart, intestine, lung, liver
	XVII	$\alpha1[XVII]_3$	Hemidesmosomes in epithelia
	XXIII	-	Heart, retina
	XXV	-	Brain, heart, testis
Multiple triple-helix domains and interruptions (MULTIPLEXIN)	XV	-	Capillaries, testis, kidney, heart, pancreas
	XVIII	-	Basement membrane, liver, lung

2.2 Proteoglycans

Proteoglycans are a large family of ECM molecules composed of long, unbranched GAG chains which are covalently attached to a protein core. GAG chains are linear polymers of repeated disaccharide units of hexosamine and hexuronic acid or hexose. In keratan sulphate, hexuronic acid is replaced by galactose. GAGs have a high negative charge due to the presence of carboxyl and/or ester groups on each repeat unit [50-53]. The five GAG types, as summarized in **Table 2.2**, are heparin sulphate/ heparin, keratan sulphate, chondroitin sulphate, dermatan sulphate and hyaluronic acid.

The main proteoglycans are syndecan, glypican, basement membrane PGs, hyalectans which include aggrecan, versican, brevican; and small leucine-rich repeat proteoglycans (SLRPs) including decorin, biglycan, fibromodulin, lumican, and keratocan [50]. The largest type of proteoglycan is aggrecan, which is present in cartilage and can represent up to 10% of its dry weight [51]. It forms multi-molecular aggregates in cartilage by noncovalently binding with glycoprotein (link protein) to a chain of high molecular weight hyaluronan. It has a core molecular weight of 225 – 250 kDa and is linked up to 100 glycosaminoglycan side chains [51, 54]. Chondroitin sulphate makes up about 95% of the side chains with the remaining 5% being keratan sulphate. Aggrecan plays a crucial role in tissue nutrition and biomechanics as it restricts the movement of water and solutes [51]. In tendon, aggrecan is important as is holds water within the fibrocartilage and resists compression [26, 38].

The three low molecular weight proteoglycans most commonly distributed in most connective tissues are decorin, biglycan and fibromodulin. Decorin is mainly expressed in skin, bone and tendon; biglycan in bone, skin, dentin and tendon; and fibromodulin in tendon and articular cartilage [50]. These proteoglycans have a core molecular weight of about 40 kDa [54]. The proteoglycans present in skin are versican, decorin, biglycan and hyaluronan (see **Table 2.3**). Versican is present in the basal layer of the epidermis, in association with fibres of the elastic

network in dermis [55] and in sweat glands as well as the sheaths of hair follicles[56]. Decorin, a small leucine-rich proteoglycan, facilitates in fibrillar slippage during mechanical deformation in tendon [26, 38]. In skin, it is largely observed in association with dermal fibres due to its ability to bind to collagen [56]. Both decorin and fibromodulin bind with collagens Type I and II in *in vitro* assays which cause delayed fibril formation and formation of thinner fibres. Conversely, biglycan does not bind to collagen but accumulates at the cell surface and in pericellular environments [54]. Biglycan in skin is localised to differentiating keratinocytes in the epidermis and also to vascular endothelium[56].

During the process of wound healing, GAGs are over expressed at the early stage and return to their normal level in the remodelling phase. During granulation tissue formation, the tissue concentrations of hyaluronic acid (a major member of GAG present in skin) increase as it provides a matrix which is readily penetrated by cells. During maturation of the wound, hyaluronic acid decreases as the chondroitin sulphate and dermatan sulphate concentrations increase. Decorin, the small dermatan sulphate PG, is involved in regulating collagen fibre formation while syndecan, a cell surface heparin sulphate PG is also involved in this phase of wound healing. Hyaluronan is eventually degraded by hyaluronidase and is replaced by PGs to provide the tissue with more resilience [57-58].

PGs cope with compressive stresses in connective tissue. The anionic glycosaminoglycan (AGAG) interfibrillar bridges in shape modules are part of a sliding filament process which converts local compression into delocalised tensile deformation. The interfibrillar bridge in shape modules (**Figure 2.3** (a)) are produced by antiparallel AGAG aggregates attached to collagen fibrils .As seen in **Figure 2.3** (b), when a compressive force is applied, tissue water is displaced in neighbouring spaces exerting pressure along the AGAG aggregates resulting in slippage between the aggregate participants. The removal of the compressive stress reverses the slippage to rest

state (on left of **Figure 2.3** (b)) depending upon the return to the original position of the tissue water [24].

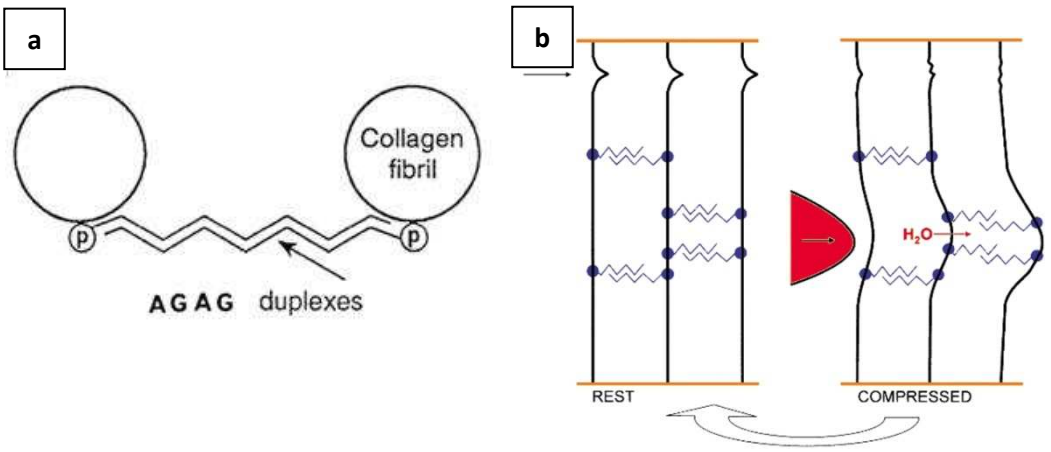

***Figure 2.3**: (a) Structure of a shape module where p is the proteoglycan protein, and (b) the reversible deformation of within shape module AGAG bridges. Collagen fibrils (black vertical lines) are bridged by shape modules (black zigzag lines) are covalently bonded to PG proteins (filled circles) which bind to fibrils at specific binding sites. Fibrils are anchored into ECM (orange horizontal lines) [24].*

***Table 2.3**: Proteoglycans in skin and its distribution [58].*

Skin layers	Types of Proteoglycans
Epidermis	Heparan sulphate, keratan sulphate, chondroitin sulphate, syndecan
Basement membrane	Heparan sulphate, chondroitin sulphate
Dermis	Heparan sulphate, chondroitin sulphate, dermatan sulphate, decorin, biglycan, fibroglycan, versican, glypican

***Table 2.2**: Disaccharide composition and structure of the different GAG chains. Adapted from [50, 52, 54, 59].*

GAG chains	Repeating dissacharide units [50, 52]	Dissacharide structure [50]	Designation [53, 59-60]
Heparin sulphate/ Heparin	D-glucuronic acid (GLcA) or L-iduronic acid (IdoA) + D-glucosamine (GlcNAc)	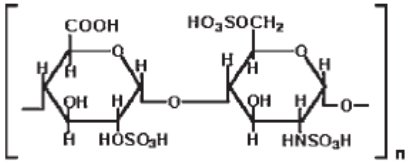	Mast cell, liver, lung, skin, intestinal mucosa, central nervous system, fibroblasts, mammary epithelial cells
Keratan sulphate	Galactose (Gal) + D-glucosamine (GlcNAc)	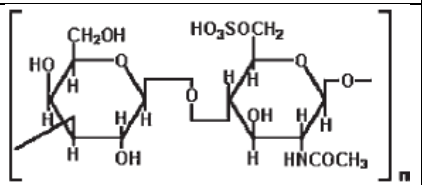	Cornea, cartilage, intervertebral disc, bone
Chondroitin sulphate	D-glucuronic acid (GLcA) + D-galactosamine (GalNAc)	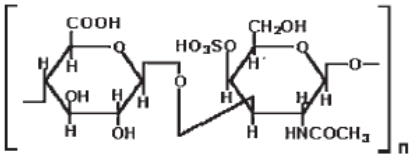	Large-aggregating: cartilage, aorta, tendon Large non-aggregating: skin, metaphysic, muscle Small non-aggregating: bone, cartilage
Dermatan sulphate	D-glucuronic acid (GLcA) or L-iduronic acid (IdoA) + D-galactosamine (GalNAc)	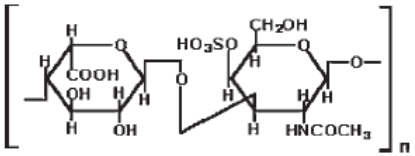	High iduronic acid content: skin, sclera, tendon, cartilage Low iduronic acid content: cornea, sclera, ovarian follicular fluid, fibroblast associated, cartilage (Type IX collagen)
Hyaluronic sulphate	D-glucuronic acid (GLcA) + D-glucosamine (GlcNAc)	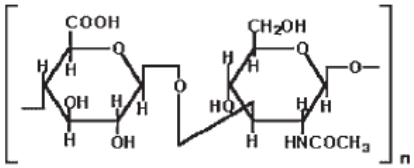	Hepatocyte plasma membrane, fibroblast plasma membrane, glomerular basement membrane, skin, synovial fluid, heart valve, cartilage

2.3 Elastin

Elastin is an insoluble, hydrophobic fibrillar material made up of tropoelastin molecules covalently bound to each other by cross-links. The key function of elastin is to provide elasticity to tissues and organs [61-65]. It is largely found in elastic ligaments (70% of the dry weight), large arteries (50%), lung (30%) and skin (2 – 4%) [64]. In tendon, elastin accounts for 2% of its dry weight and allows the collagen fibres to return to their prestretched lengths after physiological loading [26, 38].

The hydrophobicity of elastin is due to the fact that 80 – 90% [61] of elastin is made up of aliphatic, non-polar amino acids such as proline (Pro), alanine (Ala), valine (Val), leucine, isoleucine, lysine (Lys) and glycine (Gly). As is the case with collagen, nearly one third of the amino acid residues are glycine [63-64]. However, despite its highly hydrophobic nature, elastin is hydrated by solvent water that swells the protein *in vivo* and increases the entropy of the molecule [63]. Tropoelastin, the soluble precursor of elastic fibre is soluble in aqueous solutions at ambient temperature [64]. Elastin elongates and straightens under tension which exposes its hydrophobic surfaces to the aqueous environment. This results in a loss of entropy but it is the release of this energy that drives recoiling [24]. The molecular structure of the (Gly–Val–Gly–Val–Pro)$_n$ or poly(GVGVP) model of elastin is depicted in **Figure 2.4**.

In connective tissue, both collagen and elastin are present and work in tandem. While collagen provides rigidity for function, elastin allows connective tissue to stretch and return to its original state. In contrast to the right-handed triple-helical structure formed around a central axis in collagen, elastin forms a large shapeless central core from which other proteins extend. Like collagen, elastin is unusually rich in proline and glycine but, unlike collagen, is not glycosylated and contains some hydroxyproline but no hydroxylysine [66]. As strain increases within a collagen fibril framework, elastin is supplemented and superseded which determines the

maximum reversible deformation [24]. **Figure 2.5** shows the microscopical images of elastin and collagen in bovine aorta and ligament.

Elastic fibres are made up of two components: amorphous elastin and microfibrils. These elastic fibres, commonly rope-like structures, present as parallel-oriented structures in ligaments and are oriented into honeycomb structures in elastic cartilage. In heart valves, elastic fibres are sheet-like in the ventricularis, sponge-like in the spongiosa and tubular to circumferential in the fibrosa [64-65, 67].

Elastin is produced through a complex process known as elastogenesis. The tropoelastin molecule is synthesized in the rough endoplastic reticulum inside the cell. It promptly binds with a 67 kDa elastic-binding protein called galactolectin, which serves to prevent premature intracellular aggregation of tropoelastin. Once in the extracellular space, galactolectin binds with the galactosugars of the microfibrillar component, which leads to the release of the tropoelastin molecule locally. The 67kDa galactolectin then recycles back to the intracellular endosomal compartment and re-associates with the newly synthesized tropoelastin. This recycling of galactolectin is crucial for the effective extracellular deposition of insoluble elastin. [68]. The elastin molecule is deposited onto the microfibrillar component, acting as a scaffold, and is then modified by lysyl oxidase. The crosslinking process involves copper and vitamin B6-requiring lysyl oxidase, and results in a stable and mature elastin [63-64, 69]. Massively crosslinked arrays of tropoelastin in association with microfibrils contribute to tissue structural integrity and biomechanics through persistent flexibility, which allows for repeated stretch and relaxation cycles that critically depend on hydrated environments [70].

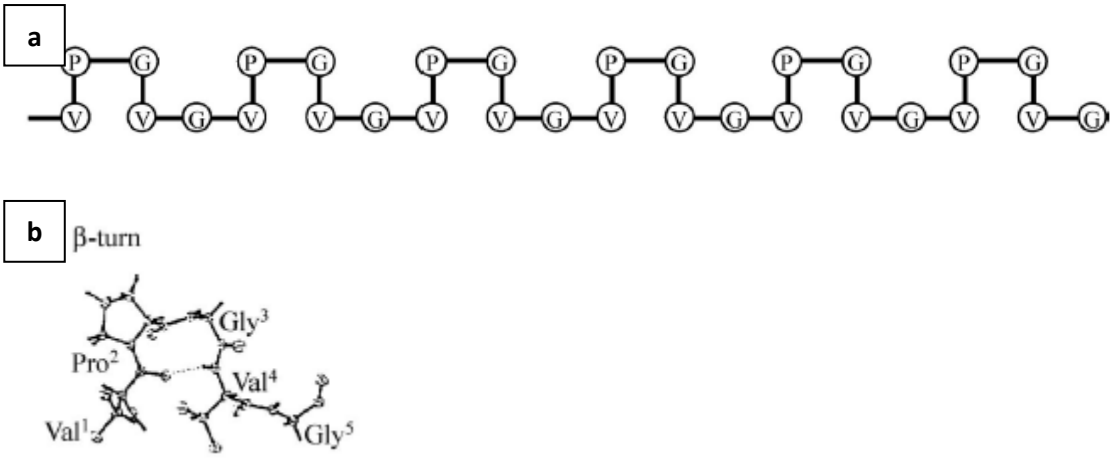

***Figure 2.4**: The molecular structure of the (Gly–Val–Gly–Val–Pro)$_n$, or poly(GVGVP) model of elastin: (a) Schematic representation of the repeating Pro-Gly-containing sequence inserting the β-turn structure, which is given in crystallographic detail in (b) [71].*

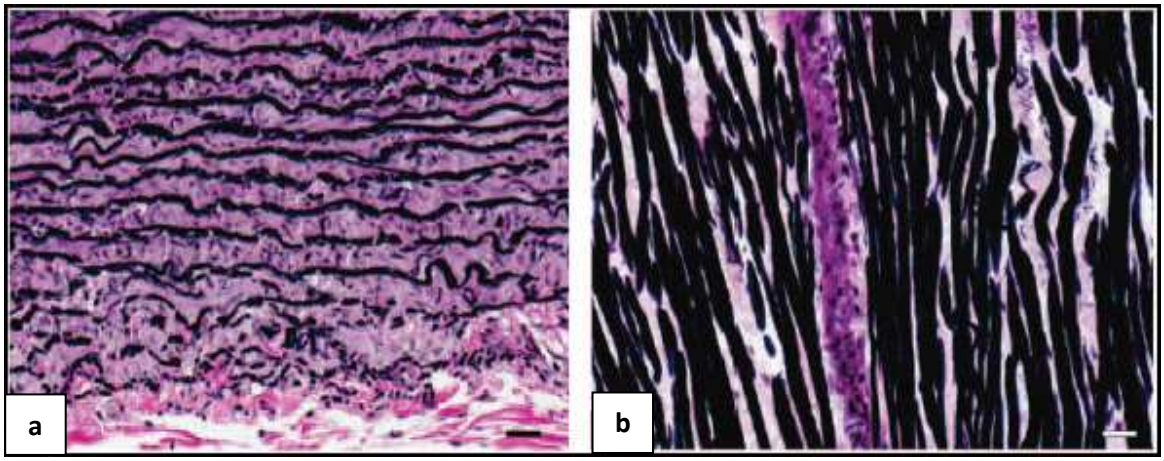

***Figure 2.5**: Light microscope images of (a) bovine aorta, and (b) ligament showing elastic fibres in black and collagen in pink (Verhoeff-Van Gieson staining; scale bar 10 µm) [64].*

3 Fibrosis

Fibrosis may be defined as “the overgrowth, hardening, and/or scarring of various tissues” [72], due to the excessive deposition of extracellular matrix components, primarily collagen. It is typically a product of chronic inflammatory reactions induced by various stimuli including but not limited to, biophysical factors like mechanical trauma and tissue injury [2], autoimmune reactions, allergic responses, and chemical and radiative stresses as well as infectious pathogens [72-73].

I will begin this chapter with an overview of normal cutaneous wound healing process as wounds heal the same way regardless of location of injury (**Section 3.1**). In the following sections, I will first describe fibrotic tissue formation as an effect of different disease conditions in specific organs (**Section 3.2**), followed by fibrotic tissue formation as a dysfunction of the wound healing process (**Section 3.3**). In all following chapters, the term fibrotic tissue will be used to denote scar tissue or any fibrous encapsulation generated in response to an injury. Scar tissue is weaker than normal tissue which is strong and highly organized. Collagen fibres in scar tissue are much smaller, have a random appearance and the tensile strength of a wound is approximately 80% of normal skin [74].

3.1 Normal Cutaneous Wound Healing

The wound healing response starts as soon as a tissue is injured and depends both on the degree of injury or defect created by the implantation procedure as well as the regenerative capacity of the tissue. Primary wound healing (also described as primary union or union by first intention) is the most common soft tissue wound encountered by surgeons. Healing of this type of wound generally occurs when the wound edges are brought together with sutures. Secondary wound healing (known also as secondary union or second intention) takes place when a large amount of cells and tissue are lost and the wound edges are widely separated. This type of wound heals by

the formation of granulation tissue which can lead to formation of a larger area of fibrotic tissue [75-77]. There are three sequential, yet overlapping stages in the regenerative phase of wound healing: inflammation, new tissue formation and remodelling (see **Figure 3.1**) [1, 18, 74-78].

3.1.1 Stage One – Inflammation

Inflammation is generally defined as the reaction of vascularised living tissue to local injury and serves to contain, neutralize, dilute or wall off the injurious agent or process [77]. Wound healing begins with a vascular response; with platelets coming into contact with collagen and extracellular matrix. These platelets adhere to collagen and start aggregating; releasing clotting factors, platelet-derived growth factor (PDGF) and transforming growth factor-beta (TGF-β) which are imperative for the wound repair process. The resulting fibrin clot becomes a scaffold for infiltrating cells. Hyaluronic acid in the blood clot helps with the physical stabilization of the matrix, stimulates cell infiltration and migration and controls degradation of fibrin [58]. PDGF is responsible for the chemotaxis (movement along chemical gradients) of neutrophils and macrophages in the wound repair process. Neutrophils are a type of white blood cell capable of ingesting and killing bacteria and provides an important defence against infection [79]. Neutrophils enter the wound site within 24 hours of injury and clean the wounded area of bacteria and foreign particles by the process of phagocytosis. Neutrophils continue to swell up with bacteria which result in what is called “laudable pus” in the wound [74]. TGF-β attract monocytes which are present in the wound after 2 to 3 days [1]. Monocytes are also a type of white blood cell which functions to ingest foreign particles such as bacteria and tissue debris [79]. These monocytes differentiate into macrophages (large scavenger cells present in connective tissue and major organs and remove bacteria as well as other foreign bodies from blood or tissue [79]) which continue the phagocytosis process. Macrophages also release more PDGF and TGF-β which are crucial for the next stage of wound healing [74, 78].

3.1.2 Stage Two – New Tissue Formation

New tissue formation occurs 2 to 10 days after injury. It is at this stage that cellular proliferation and migration of several cell types occur. The process begins with keratinocytes (a type of cell that makes up 95% of the cells of the epidermis [79]) migrating over the injured dermis, followed by angiogenesis where new blood vessels are formed. The migration and proliferation of keratinocytes is induced by the proteoglycan syndecan [58]. Angiogenesis is stimulated by vascular endothelial cell growth factor (VEGF) and basic fibroblast growth factor (bFGF; also known as FGF2) and occurs due to the high metabolic activity at the wound site. The fibrin matrix is then replaced with fibrous tissue by the capillaries associated with fibroblasts and macrophages. The proliferation and maturation of keratinocytes result in the restoration of the epithelium barrier function [1, 74]. Hyaluronic acid expands the extracellular space and creates an environment for cell movement in early granulation tissue formation. As wound healing progresses, the number of fibroblasts increases. Macrophages stimulate fibroblast proliferation. Fibroblasts migrate from the edge of the wound or from the bone marrow and some differentiate into myofibroblasts which eventually bring the edges of the wound together. Fibroblasts are vital in the production of new ECM [1, 74, 76].

3.1.3 Stage Three – Remodelling

The remodelling phase begins 2 to 3 weeks after injury and usually lasts longer than a year. It is characterized by the marked decrease in the processes activated post injury with fibroblasts, macrophages and myofibroblasts leaving the wound or undergoing apoptosis (programmed cell death). The wound becomes less vascular and have only a few cells containing mostly collagen and other extracellular matrix proteins. This phase is variable in different types of wounds and can take up to several weeks in cases where a large fibrous tissue is formed. The remodelling stage results in a dense avascular scar containing mainly Type III collagen, which over a period of 6 to 12 months is actively remodelled to predominantly Type I collagen. This process which is

carried out by matrix metalloproteinases secreted by fibroblasts, macrophages and endothelial cells, strengthens the tissue [1, 76]. PGs are also involved in this phase of wound healing whereby hyaluronic acid concentration decreases as chondroitin sulphate and dermatan sulphate concentrations increase. Decorin, the small dermatan sulphate PG, is involved in regulating collagen fibre formation while syndecan, a cell surface heparin sulphate PG is also involved in this phase of wound healing [57-58]. As seen in **Figure 3.1** (c), the healed region appears to be slightly higher than the surrounding surface and never assumes the normal appearance of uninjured skin with the absence of normal skin appendages [1, 76].

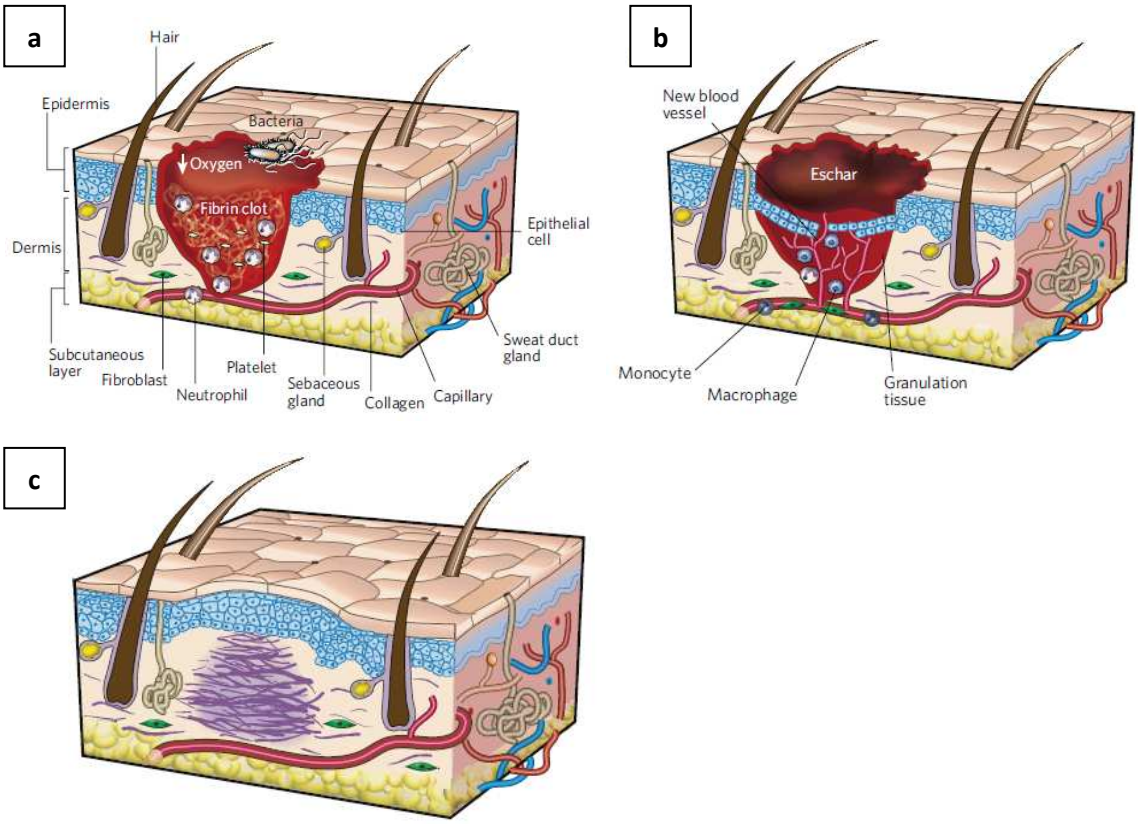

Figure 3.1*: The three essential stages of wound repair; (a) inflammation, (b) new tissue formation, and (c) remodelling. Stage one – inflammation is illustrated by a skin wound about 24 to 48 hours after injury. Stage two – new tissue formation is depicted by a skin wound about 5 to 10 days after injury. Stage three – remodelling is shown by a skin wound about 1 to 12 months after repair [1].*

3.2 Fibrosis: A Clinical Viewpoint

The major organs affected by fibrosis are the lung (interstitial lung disease), heart (hypertension or post-myocardial infarction), liver (alcoholism which leads to liver cirrhosis), scarring of the kidneys due to diabetes, skin hypertrophic scarring due to burn injuries and surgical procedures, and several others which are summarized in **Table 3.1**. Fibrosis in organs such as the lung, heart, kidney and liver occurs in the extracellular space and are referred to as primary interstitial disease [80]. Discussion in this section will be focused on the two major organs affected by fibrosis, namely the lung and the heart.

Table 3.1*: Tissues affected by fibrosis and possible causes [72].*

Tissues affected by fibrosis	Causes
Lung	Interstitial lung diseases caused by sarcoidosis, silicosis, drug reactions and infections, and collagen vascular diseases like rheumatoid arthritis and sclerodema
Heart	Hypertension, atherosclerosis, restenosis, scar tissue post-myocardial infarction
Liver	Viral hepatitis, schistosomiasis and alcoholism leading to cirrhosis
Kidney	Untreated hypertension, kidney scarring due to diabetes
Eye	Macular degeneration, retinal and vitreal retinopathy leading to blindness
Skin	Keloids, hypertrophic scars, systemic sclerosis and sclerodema, burns
Pancreas	Possibly autoimmune or hereditary
Intestine	Inflammatory bowel disease, pathogenic organisms
Brain	AIDS, Alzheimer's
Bone marrow	Cancer, ageing
Multi-organ fibrosis	Tissue scarring form surgical complications, chemotherapeutic drug-induced fibrosis, radiation-induced fibrosis from cancer therapy, mechanical injuries

Interstitial lung diseases are diagnostically classified as drug induced, pneumoconiosis, collagen vascular disease-associated lung disease, alveolar filling disorders, idiopathic pulmonary disorders, and primary lung diseases such as sarcoidosis and chronic hypersensitivity pneumonitis [81-82]. Idiopathic pulmonary fibrosis (IPF), the most common type of interstitial

lung disease (ILD) [16, 72] also occurs in idiopathic interstitial pneumonias, and as a response to lung injury including chemotherapeutic drugs and cancer therapy radiation [83].

IPF is a result of sequential acute injury to the lung which leads to critical damage of alveolar lining cells. Although the initiation events of the cycle are not fully understood, the subsequent inflammatory cell infiltration in the interstitium of the lung is followed by collagen proliferation and aberrant wound healing, characterized by excessive deposition of ECM leading to fibrosis which leads to thickening of the alveolar wall. The structural remodelling of the gas-exchange tissue along with the development of honeycomb change involves lung airspace fibrosis and alveolar collapse which eventually leads to airspace obliteration [17, 81, 84-86]. Active inflammation and end-stage fibrosis may appear in the same lung [81]. The histological variation between fibrosis, inflammation, honeycomb change and normal lung tissue seen in usual interstitial pneumonia, one of the four pathologic subcategories of IPF as defined by Katzenstein et al. [87] is depicted in **Figure 3.2**.

Myocardial fibrosis occurs in a range of conditions such as hypertension [88], chronic aortic regurgitation [89] and post-MI [11, 90-93]. Idiopathic interstitial myocardial fibrosis has also been found in highly trained athletes due to long repetitive arduous physical activity [94-95]. Myocardial infarction is the death of a segment of heart muscle that occurs when the artery carrying its blood supply is obstructed by a blood clot [79]. It is more commonly known as a heart attack. Taking the case of fibrosis formation post-MI as an example, the wound healing process begins with the death of cardiomyocytes (cells that comprise cardiac muscle) via necrosis (cell swelling) and apoptosis (cell shrinkage). This is followed by an inflammatory phase which occurs approximately 12 to 16 hours after infarction [91] leading to leukocyte infiltration into the infarct area. Leukocytes remove dead cells and attract other inflammatory cells like lymphocytes and macrophages into the area. Granulation tissue is then deposited, which matures into fibrotic tissue. In the early stages post-MI, the abnormal accumulation of collagen

provides the much needed mechanical support in preventing myocardial wall rupture. However, irreversible fibrosis also occurs in areas remote from the infarct site. Progressive fibrosis eventually stiffens the heart affecting both systolic and diastolic functions [96], and impairs mechano-electric coupling of cardiomyocytes resulting in the increased risk of arrhythmias [9-10]. Excessive fibrotic tissue accumulation also reduces capillary density and increases oxygen diffusion distance which affects cardiomyocyte metabolism and performance, leading to deterioration of heart function and eventually to congestive heart failure [97-98]. The increased level of fibrosis in mouse hearts post-MI can be seen in **Figure 3.3**. 3 days post-MI, early fibrotic tissue formation is visible. After 14 days, a thin stretched infarct (a small localized area of dead tissue produced as a result of inadequate blood supply [79]) which results in interstitial fibrosi can be seen in the borderzone of the infarcted region [92].

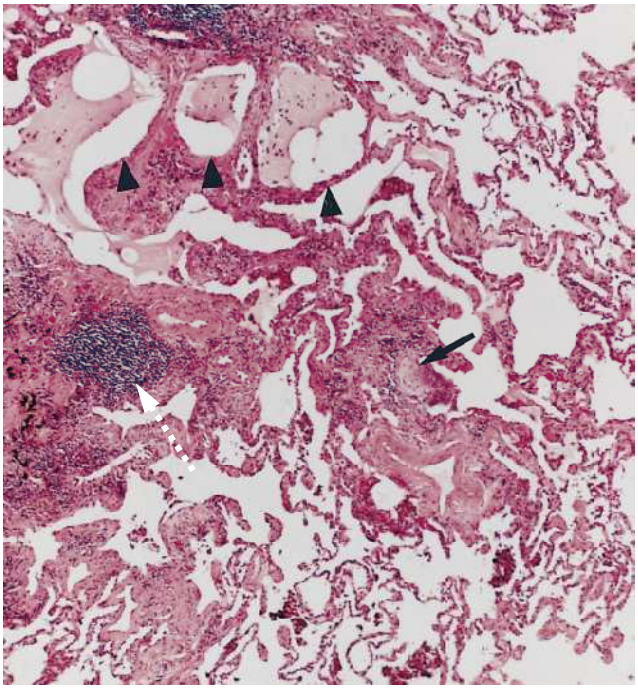

Figure 3.2*: Low magnification view of interstitial pneumonia in the lung. Fibrotic areas with dense collagen deposition (left of image indicated with white dotted arrow) alternate with areas of relatively unaffected lung tissue (right and bottom centre). Honeycomb change (black arrowheads), characterized by mucin-filled, enlarged air spaces separated by fibrosis are apparent. High fibroblast activity (black arrow) corresponding to inflammation is also evident. (Hematoxylin and eosin staining) [87].*

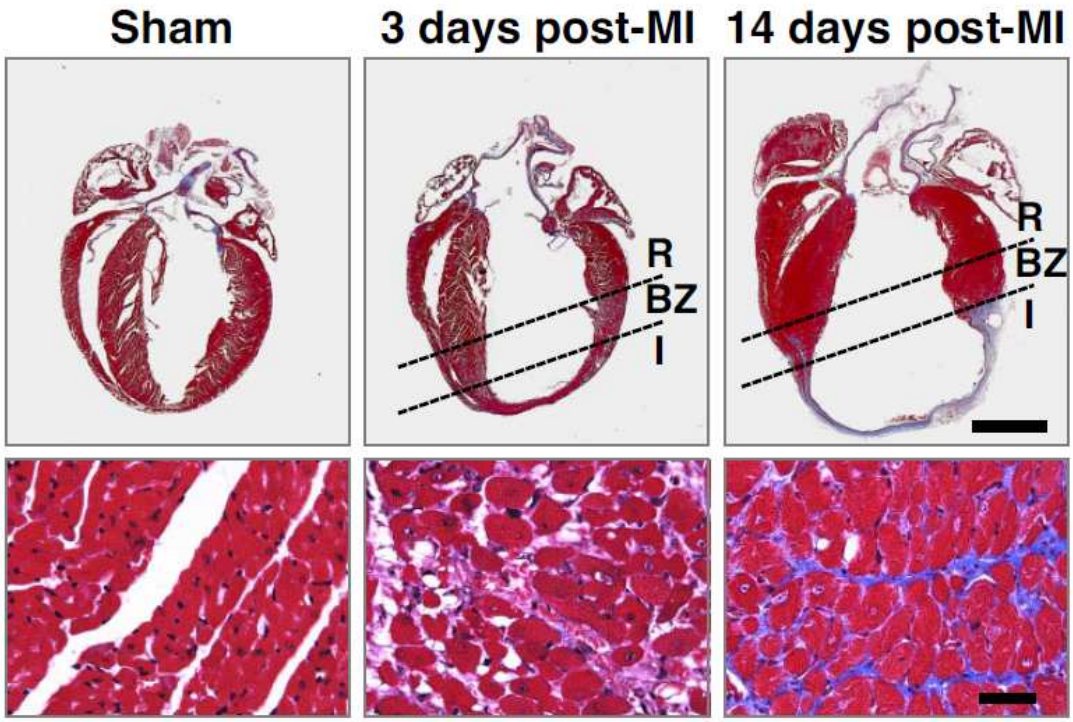

***Figure 3.3**: Post-MI fibrotic tissue formation on mouse heart sections after 3 and 14 days. Lower images are higher magnification images of the borderzone regions of the infarcted hearts compared to a sham operated heart. (I: infarct; BZ: borderzone; R: remote myocardium. Scale bars: upper 2 mm; lower 20 µm) [92].*

3.3 Implant-Induced Fibrosis

Biocompatibility may be defined as "*the ability of a material to perform with an appropriate response in a specific application*" [99]. The implantation of any kind of material into the human body results in a tissue response. Implantable materials can range from silicone breast implants, drug delivery devices, sensors, and prosthesis, to medical devices such as hip implants, pacemakers and stents.

A complex, multifaceted set of responses follow the implantation of a material (biomaterial) in living tissue, as illustrated in **Figure 3.4**, and are denoted by the generic term Foreign Body Response (FBR). FBR with the development of granulation tissue is the normal wound healing response to implanted biomaterials. Similarly to cutaneous wound healing (as described in **Section 3.1**), FBR begins with injury or implantation followed by infiltration of inflammatory cells such as monocytes and leukocytes. Acute inflammation lasts from minutes to days depending on the extent of injury, subsequently followed by chronic inflammation which appears histologically less uniform compared to acute inflammation. The histologic appearance of chronic inflammation is characterized by the presence of macrophages, monocytes and lymphocytes as well as the proliferation of blood vessels and connective tissue. Significant chronic inflammation may occur due to the chemical and physical properties of the biomaterial as well as micromotion at the implant site. These cascading events affect the degree of granulation tissue formation, foreign body reaction and ultimately fibrotic tissue formation [75, 77]. The end stage of tissue repair can occurs in two distinct ways: first, the regenerative phase where injured cells are replaced by cells of the same type; and second, fibrosis where normal parenchymal tissue (functional tissue of the organ) is replaced by connective tissue [75, 100]. The biocompatibility of an implant is typically determined by the extent of fibrotic tissue formation surrounding the implant as a function of time [75], with less fibrosis indicating better biocompatibility.

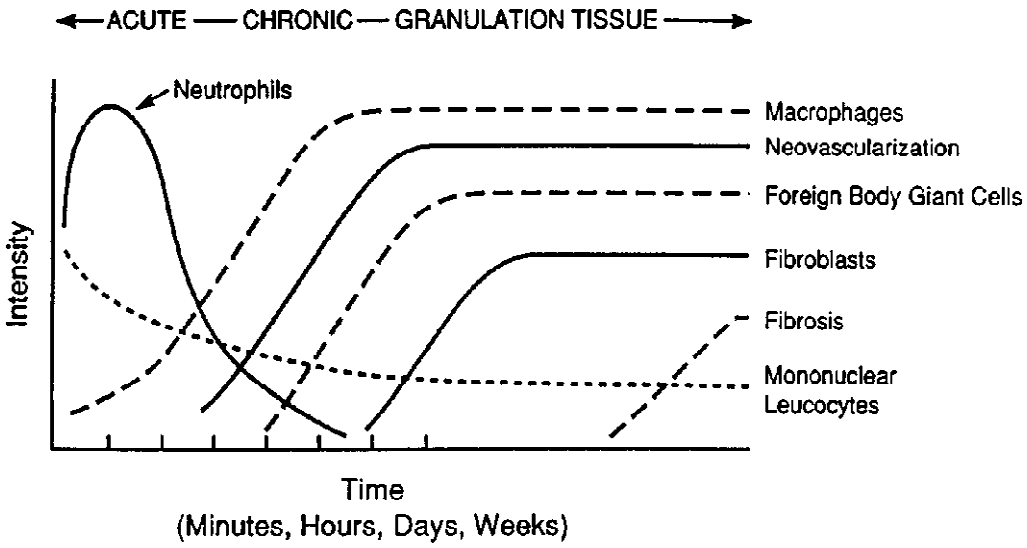

***Figure 3.4**: Temporal variation in tissue response to implanted biomaterials [75].*

There has been extensive research done in the area of fibrotic tissue response to implants, and the consequences for biocompatibility. A team of researchers at the University of Mississippi and Medical Center have studied the fibrotic tissue formation surrounding a variety of devices implanted at two surgical sites, subcutaneously (SC), which is beneath the skin and intraperitoneally (IP), in the abdominal cavity [101-104]. **Table 3.2** summarizes the effect of implantation site on five types of implants; aluminum calcium phosphate (ALCAP), hydroxyapatite (HA), tricalcium phosphate (TCP), poly-L-lycine (PLL) coated ultra high molecular weight polyethylene, and saline coated ultra high molecular weight polyethylene. A thin translucent layer of fibrotic tissue was visible surrounding all implants (see **Figure 3.5**). Fibrotic tissue thickness was measured 90 days post implantation using an ocular micrometer mounted in the objective of a light microscope. In all implant types except saline coated ultra high molecular weight polyethylene, fibrotic tissue thickness from implants in the intraperitoneal cavity was found to be larger than those retrieved from the subcutaneous implantation site. This finding is in agreement with earlier studies done by the same team using tricalcium phosphate-lycine (TCPL) delivery devices [105]. Thickness of the fibrotic tissue was also found to be positively correlated to the presence of macrophages, neutrophils, fibroblasts and capillaries in

the fibrotic tissue matrix. Butler et al. [103] did not however, provide an explanation as to why there was no significant difference in fibrotic tissue thickness between the two implantation sites for the saline coated ultra high molecular weight polyethylene implant. The extent of tissue damage caused by the surgical procedure itself is unknown but may contribute to the foreign body reaction [101-103]. These studies show that the implantation site (which affects the micromotion of the implant) and implant material (i.e. size, shape and topography) play a large role in the variation of fibrotic tissue thickness. Implant movement due to daily activity could result in a variable degree of mechanically induced tissue damage.

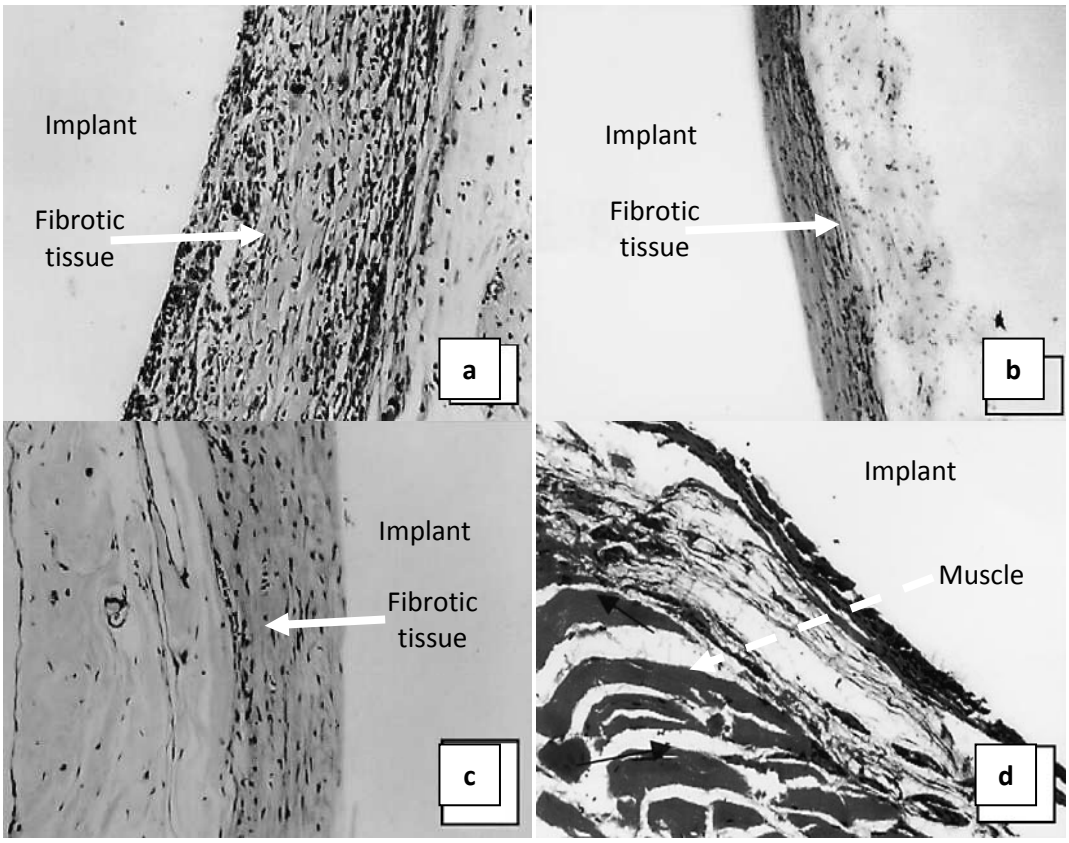

Figure 3.5*: Fibrotic tissue matrix surrounding implants 90 days post-implantation. ALCAP implants implanted (a) in the intraperitoneal cavity (10x), (b) subcutaneously (10x), and HA implants implanted (c) in the intraperitoneal cavity (4x), (d) subcutaneously (4x). In all images, on the immediate surface next to implant there is a cell layer of 1 to 3 cells thick followed by a dense layer of fibrotic tissue and finally a loose connective fibrous tissue. [101].*

***Table 3.2**: Fibrotic tissue thickness for different devices at two implantation sites 90 days post implantation.*

		Fibrotic tissue thickness 90 days post implantation (Mean ± SD microns)				
	Implant type	ALCAP [101-102, 104]	HA [101],[104]	TCP [102],[104]	PLL [103]	Saline [103]
Site	Subcutaneous	120.3 ± 7.1	162.0 ± 2.0	161.8 ± 1.7	132.8 ± 31.5	200.2 ± 6.2
	Intraperitoneal	456.9 ± 27.2	476.5 ± 14.2	720.4 ± 98.9	326.2 ± 7.3	200.4 ± 7.2

Legend: ALCAP = aluminum calcium phosphate; HA = hydroxyapatite; TCP = tricalcium phosphate; PLL = poly-L-lycine coated ultra high molecular weight polyethylene; Saline = saline coated ultra high molecular weight polyethylene.

Benghuzzi et al. [105] also studied the effect of time on TCPL delivery devices at two implantation sites, subcutaneous and intraperitoneal. Regardless of the implantation site, fibrotic tissue formation occurred and the fibrotic tissue thickness increased with time. Fibrotic tissue thickness in the subcutaneous and intraperitoneal sites increased from 2200 µm ± 230 µm and 3000 µm ± 170 µm, respectively after 1 week to 4500 µm ± 250 µm and 7200 µm ± 540 µm, respectively after 5 weeks. Fibrotic tissue formation was also found to be higher in the intraperitoneal surgical site as compared to the subcutaneous site.

Implant surface chemistry and topography are important factors in the formation of fibrotic tissue. The type of coating material used on implant surfaces is critical in ensuring the biocompatibility of both long-term and short-term implantable devices. Suska et al. [106] coated 1 mm thick polydimethylsiloxane (PDMS) or more commonly known as silicone disks with noble metals silver (Ag), gold (Au) and palladium (Pd) and implanted them subcutaneously on the back of Sprague-Dawley rats. Fibrotic tissue thickness was measured 21 days post implantation. Fibrotic tissue thickness was found to be higher on coated implants (> 100 µm) as compared to the control PDMS implant (86.5 µm). The thickest fibrotic tissue formation with a mean thickness of 159 µm was seen in PDMS disks coated with layers of Ag, high Pd concentration and

low Au concentration; as illustrated in **Figure 3.6** (b). It was also established that PDMS disks coated with silver only or with silver combined with low concentrations of palladium and gold induced the thinnest fibrotic tissue formation compared to other metal coatings (see **Figure 3.7**) [106]. Tissue reaction to noble metals is similar to that of wound healing; i.e. only a thin fibrotic capsule is formed. This is due to the fact that noble metals are chemically inert in which diffusion of metal ions and oxygen which cause oxidation or corrosion do not occur. Pure metals (except noble metals) tend to evoke severe tissue reaction in which healing is slow and a thick fibrotic capsule is formed [107].

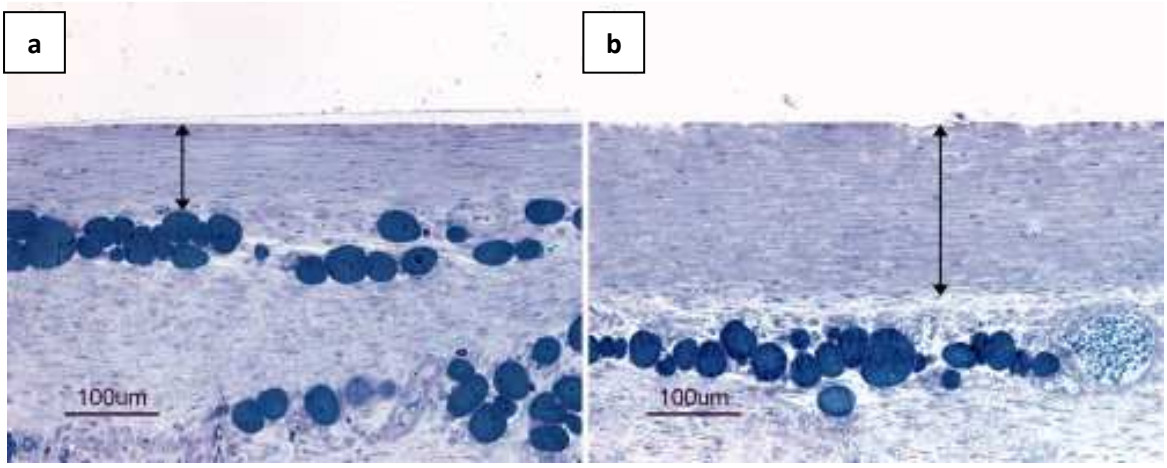

***Figure 3.6**: Fibrotic tissue thickness (shown with arrows) in (a) uncoated PDMS disk, and (b) a PDMS disk coated with layers of Ag, high Pd concentration and low Au concentration. Fat storing cells are stained dark blue. (Staining by Richardson solution) [106].*

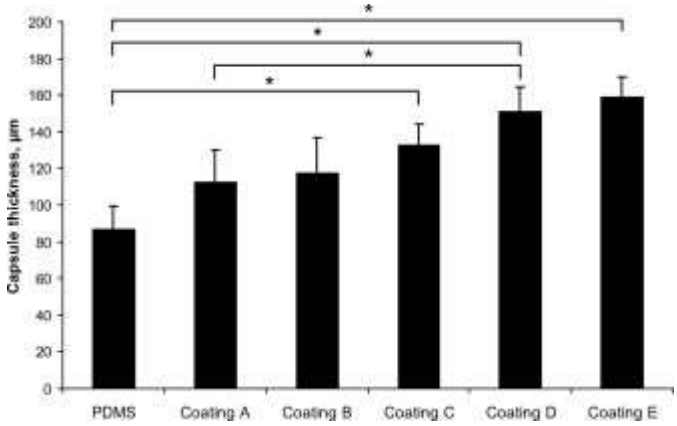

***Figure 3.7**: Fibrotic tissue thickness measured 21 days post implantation. PDMS = control; Coating A = Pure Ag; Coating B = Ag, low Pd, low Au; Coating C = Ag, low Pd, medium Au; Coating D = Ag, medium Pd, medium Au; Coating B = Ag, high Pd, low Au [106].*

The effect of coating material on fibrotic tissue thickness was also studied by Zeplin et al. [108] Textured monosilicone implants and surface-modified phosphorylcholine (PC)-coated silicone implants were implanted submuscularly into Sprague-Dawley rats and fibrotic tissue thickness was measured at its thinnest area 3 months after implantation. The PC-coated silicone implants generated a fibrotic tissue thickness of 143.34 µm ± 13.98 µm (median ± standard deviation) giving a statistically lower ($p \leq 0.05$) thickness as compared to 175.55 µm ± 29.59 µm thickness seen in the control textured monosilicone implants. Hydrophopic surfaces enable interaction of the implant with surrounding tissue resulting in unspecific adsorption of proteins, cells and bacteria. Activated monocytes which produce growth factors and fibrocyte stimulating cytokines tend to adhere more to hydrophobic polymer surfaces. The introduction of PC coating on the silicone implants increased the hydrophilicity of the breast implants leading to a reduction in foreign body reaction and ultimately to a lower fibrotic tissue thickness.

The temporal development of fibrotic tissue formation after 3 and 6 months around breast implants filled with various substances implanted subcutaneously in the lower back of Sprague-Dawley rats showed that fibrotic tissue thickness increased significantly with time in implants filled with cohesive silicone ($p = 0.034$) and hydrogel ($p = 0.05$). The increase in fibrotic tissue thickness correlated with an increase in inflammation and the presence of macrophages. The increase in foreign body reaction in hydrogels may be due to diffusion of hydrogel through the thin surface of the implant. Implants filled with saline and silicone however, did not show a difference in fibrotic tissue thickness between 3 and 6 months. This study also found a significant correlation between fibrotic tissue formation and chronic inflammation [109]. The findings of this study underline the importance of the implant material in the formation of fibrotic tissue.

Implants with larger surface roughness illicit a reduced inflammatory response and thinner fibrotic tissue regardless of implant location in rats. Pillar surface textured implants placed in fatty tissue result in a thinner fibrotic tissue formation due to the reduction in interfacial shear

forces between the implant and surrounding tissue. Shear forces occur due to the micromotion of implants due to muscle activity, body acceleration and external forces. The interaction between fat cells which absorb the applied stress, and pillar surface texturing result in shear stresses being distributed over a larger surface area [110].

The effect of implant thickness and porosity of different polymers on the thickness of fibrotic tissue 7 weeks post implantation were studied by Ward et al. [111]. Fibrotic tissue thickness of the different polymers is summarized in **Table 3.3**. Thinner solid amphiphilic polycarbonate-based polyurethane with silicone and polyethylene oxide (PU-S-PEO) implants of 300 µm thickness resulted in a thinner fibrotic tissue as compared to 2000 µm implants. In implants of 2000 µm thickness, fibrotic tissue formation was lower in PU-S-PEO implants than in pure polyurethane (PU) implants. This could be due to the hydrophilicity of polyethylene oxide (PEO) and the presence of silicone, a biomaterial widely used. Fibrotic tissue thickness in polyvinyl alcohol (PVA) sponge with 60 µm channel size and 500 µm thickness, and expanded polytetrafluoroethylene (ePTFE) with specified pore size of 1 µm and sheet thickness of 145 µm, were similar to those seen in 2000 µm PU-S-PEO implants. The fibrotic tissue density was however much lower in the porous materials in which the loose collagen network allows for use in biosensors.

Table 3.3*: Fibrotic tissue thickness generated by different polymers 7 weeks post implantation.*

Implant type	Solid PU-S-PEO 300 µm	Solid PU-S-PEO 2000 µm	Solid PU 2000 µm	Porous PVA 500 µm	Porous ePTFE 145 µm
Fibrotic tissue thickness (Mean ± SD microns)	84.3 ± 2.9	104.9 ± 9.7	193.2 ± 12.6	109.6 ± 12.9	122.0 ± 12.1

Another study on the temporal development of fibrotic tissue was carried out using titanium implants. Four types of machined titanium implants were implanted in the subcutaneous layer of Sprague-Dawley rats and fibrotic tissue formation was measured 7 and 28 days post

implantation. In all four implants, titanium (Ti), porous titanium (PTi), blood plasma clot film-coated titanium (plasmaTi) and blood plasma clot film coated-porous titanium (plasmaPTi), an increase in fibrotic tissue thickness was observed. After 7 days, all implants had about 80 µm fibrotic tissue thickness. This increased to 200 µm after 28 days [112]. Surface modification of the implant materials used in this study showed no significant differences in fibrotic tissue thickness. This is in contradiction to the fundamental understanding that surface roughness and porosity reduce fibrotic tissue thickness as shown in a previous study by Picha et al. [110]. Increasing the surface roughness of silicone breast implants at the sub-micron scale has been shown to decrease fibroblast proliferation which could lead to a reduction in fibrotic tissue thickness [113]. Larger sized grooves (500 nm – 2 µm) in the topography of polymers limit macrophage activation which can affect the formation of fibrotic tissue [114].

The development of fibrotic tissue is largely induced by biophysical or mechanical forces. The natural movements of the tissue result in shear stress and strain at the tissue biomaterial interface. When an implant with higher Young's modulus than the surrounding tissue is introduced, stresses will concentrate at the implant-tissue interface as the tissue moves naturally which ultimately leads to the formation of fibrotic tissue [115].

Hypertrophic scarring can occur as a result of tensile stresses during wound healing, hence utmost care must be taken in managing the wound [116]. Aarabi et al. [117] demonstrated that applying tensile forces during the proliferative phase of wound healing (day 3 to day 6) in mice resulted in hypertrophic scarring. The thickness and cross sectional area of the scar (see **Figure 3.8**) increased after 2 weeks of loading and no further increase was seen in week 4 till week 24. This study clearly indicated the negative effect of mechanical forces on hypertrophic scar formation. The treatment of hypertrophic scars formed post-second and third degree burns with pressure showed a reorganization of collagen fibres from a disorganized form into a parallel arrangement. Pressure therapy also resulted in the rearrangement of fibrillin and elastin

allowing them to function as in normal dermis. Pressure treatment leads to ECM reorganization and the decrease in cellularity seen in the final stages of wound healing [118]. In such cases applying mechanical pressure results in the resolution of hypertrophic scarring.

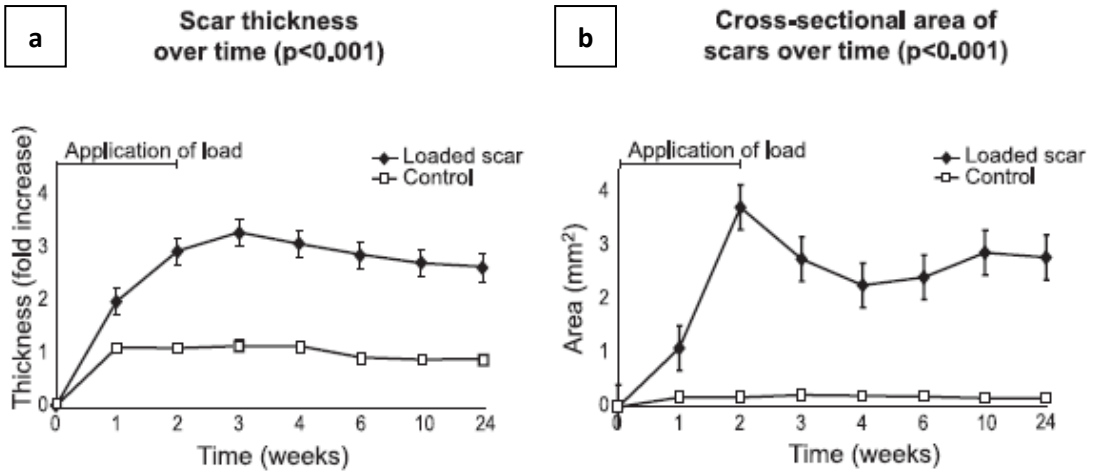

***Figure 3.8**: Scar (a) thickness and (b) cross-sectional area changes post tensile loading in adult mice [117].*

Great care should be taken in applying murine model studies in understanding the effect of mechanical forces on the formation of fibrotic tissue in skin as studies have shown that adult human wounds demonstrate excessive dermal scarring as compared to murine wounds [119-120]. Fetal skin wounds that occur during the first one-third to one-half of gestation regenerate without scarring [8]. Low resting tension found in murine skin suggests that the intrinsic forces may not be sufficient to activate the processes that lead to human hypertrophic scarring [117].

These studies indicate that fibrotic tissue formation is a natural tissue response to the implantation of any foreign object in the body. The extent of fibrotic tissue formation is however, dependent on a number of factors, namely the biological environment of the implantation site as well as the implant material size, shape, topography and physicochemical surface properties. Implant micromotion could also result in a variable degree of mechanically induced tissue damage.

3.4 Scattering and Diffraction Analysis of Fibrotic Tissue

Quantitative analysis of the developing collagen architecture is an essential, but so far almost completely neglected, aspect of wound healing research. While techniques such as confocal microscopy and transmission electron microscopy can discriminate between fibrotic tissue and unwounded tissue collagen morphology [121], these methods do not offer nanostructural information. X-ray scattering and diffraction analysis of fibrotic tissue offer an advantage over biochemical analysis and electron microscopy techniques as it is capable of providing information on both the molecular and fibril parameters of collagenous tissue. X-ray diffraction also allows for the tissue to be kept hydrated during testing thus reducing processing artefacts. SAXS and WAXD results represent averages throughout the entire tissue length as compared to the highly selective nature of electron microscopy.

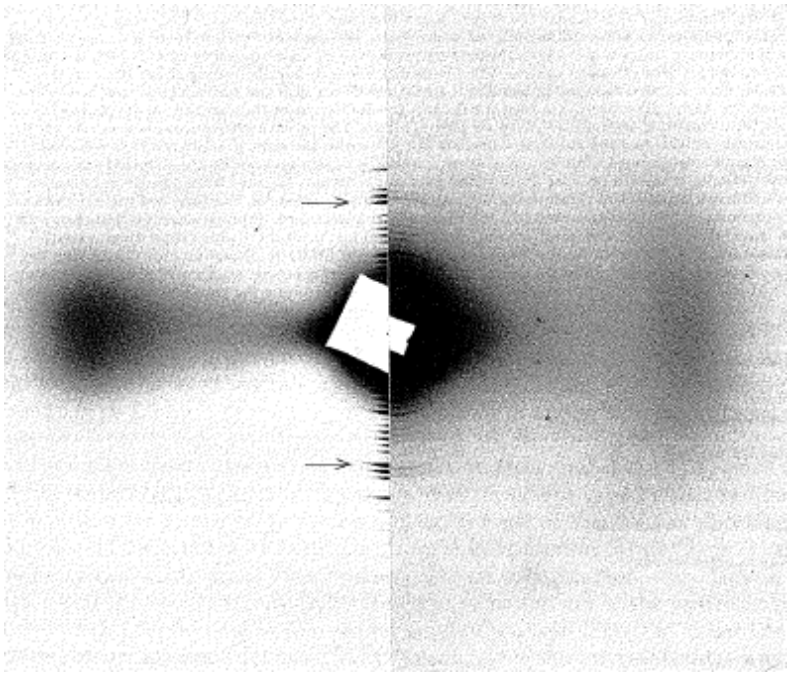

Figure 3.9*: X-ray diffraction patterns of wet lamb leg tendon (left) and wet lamb leg skin (right). Arrows indicate 12th order [43].*

Brodsky and co workers pioneered the application of SAXD to study the differing meridional SAXD patterns from skin [43] in the early 1980s. In this study it was observed that wet lamb leg

skin and wet rat tail skin had a shorter axial periodicity (D-spacing) of 65.2 nm as compared to 67 nm seen in native tissues such as lamb leg tendon, rat tail tendon, rat Achilles tendon and calf Achilles tendon. The X-ray diffraction pattern is shown in **Figure 3.9**. This was attributed to the presence of Type III collagen in skin which although homologous to Type I present in tendon, has a different amino acid residue in one third of its sequence. It was hypothesized that the interaction of the positively charged amino acid residues with negatively charged proteoglycans in skin possibly reduce charge repulsion and allow collagen in skin to adopt a less extended form.

A recent SAXS study carried out by Cócera et al. [122] on healthy skin showed a characteristic collagen pattern with a D-spacing of 63.4 nm in both whole skin and the dermis layer. In the complete skin sample in long configuration up to the 10th order reflection is visible, whereas in the short configuration the diffraction pattern for complete skin goes from 3rd order till the 24th order (see **Figure 3.10**). The scattering feature due to the cylindrical shape of the fibrils can be seen between the 1st and 3rd peak in **Figure 3.10** (a). The study did not however, indicate if the skin specimens were tested in wet or dry state.

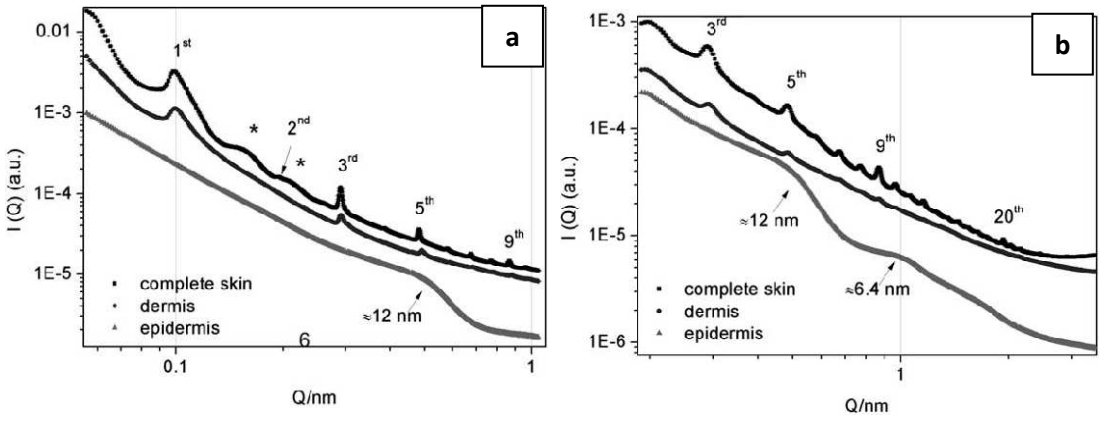

***Figure 3.10**: Radial averages of SAXS patterns of skin, dermis and epidermis measured at two sample-to-detector distances (a) 5 meters (long configuration) and (b) 1.4 meters (short configuration) [122].*

In contrast to the (admittedly limited) examples of skin SAXD described previously, the application of X-ray diffraction (either SAXS or WAXD) to fibrotic tissue however has not been

studied extensively due to the poor degree of fibrillar orientation of the tissue. Brodsky [123] used X-ray diffraction technique to study collagen organization in an oriented fibrous capsule. Fibrous capsule had formed around a silicon tube covered with polyester mesh which had been implanted below the cutaneous trunci muscle of a sheep. Polyester-collagen composite samples were explanted after 13 weeks and tested while immersed in PBS. An axial periodicity of 65.5 nm was detected from the 7^{th} up to the 25^{th} order reflection (**Figure 3.11**). A single broad equatorial maximum which relates to the average lateral intermolecular spacing or the packing density in collagen fibrils was detected near 1.57 nm, similar to that in skin but larger than that reported for tendons [124]. It was suggested that the decreased D-spacing in the fibrotic tissue (65.5 nm compared to 67 nm in tendon) could be due to the presence of Type III collagen as well as the tilting of collagen molecules with respect to the fibril axis. A poor diffraction pattern with little order was seen on granuloma tissue prepared without polyester mesh. It is unclear how the growth of granuloma tissue was induced.

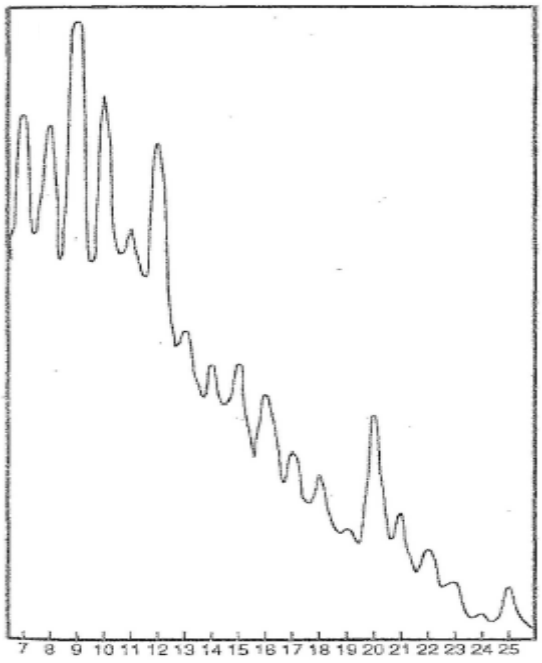

***Figure 3.11**: X-ray pattern along the meridional axis showing the 7^{th} to 25^{th} orders of the 65.5 nm period [123].*

***Table 3.4**: Average interfibrillar spacing, fibril diameter and intermolecular spacing of corneal fibrotic tissue measured in hydrated state [125].*

Time points	SAXS		WAXD
	Interfibrillar spacing (Mean ± SD nm)	**Fibril diameter (Mean ± SD nm)**	**Intermolecular spacing (Mean ± SD nm)**
3 weeks	63.0 ± 5	-	1.67 ± 0.06
6 weeks	66.1 ± 5	> 39.2	1.62 ± 0.06
7 months	71.8 ± 0.6	43.5 ± 0.9	1.72 ± 0.06
14 months	71.8 ± 2.8	42.9 ± 1.0	1.75 ± 0.04
21 months	72.8 ± 2.5	43.4 ± 0.7	1.75 ± 0.06
Control	66.3 ± 3.5	41.7 ± 0.4	1.78 ± 0.06

SAXS and WAXD have also been used to understand the changes in collagen molecular and fibrillar spacing and fibril diameters as a function of age in corneal fibrotic tissue and its effect on tissue opacity [125]. Corneal tissue is far more regularly ordered than other collageneous tissues (due to the physiological requirements of transparency), and hence may be more likely to show SAXD/WAXD spectra even in a fibrotic state. An axial periodicity of 65 nm was found in fibrotic tissue at all time points (3 weeks, 6 weeks, 7 months, 14 months and 21 months). The average spacing between collagen fibrils calculated from the first-order equatorial reflections in SAXS showed a gradual increase from 3 weeks to 21 months which suggests a reduction in packing density compared to normal corneal tissue (**Table 3.4**). Average fibril diameter in fibrotic tissue was generally slightly higher than that of normal corneal tissue. However, the range of fibril diameters, obtained by calculating the ratio of peak height to peak width at half height of the first subsidiary equatorial reflection, showed an increase in the early stage but returned to normal after 14 months. Analysis of the WAXD data provided intermolecular spacing information, which indicated a lower intermolecular spacing in fibrotic tissue as compared to healthy tissue although not significantly different after 7 months. Corneal fibrotic tissue increased in transparency as fibrotic tissue age increased, but was still more opaque than that of

normal corneal tissue. The results of this study suggest that collagen interfibril order changes with time consistent with the decrease in tissue opacity and neither fibril diameter nor intermolecular spacing have any impact on corneal tissue opacity during healing.

Brodsky and Eikenberry [124] have provided an extensive review on the application of X-ray diffraction on various native tissues. Skin samples from lambs, rats, humans, dogs and calves were found to have a lower D period in the range of 65.2 – 65.8 nm as compared to 67 nm seen in rat tail tendon, while an increase in equatorial spread is observed. This is consistent with the tilting of collagen molecules by about 12° with respect to the fibril axis. The intermolecular spacing varies between the different tissues with the smallest seen in noncalcifying tendons (1.44 – 1.49 nm), followed by skin, bone and calcifying tendons (about 1.53 nm) and cartilage with the largest spacing of 1.6 nm. Some tissues such as rat tail tendon exhibit the presence of sharp reflections indicating the existence of ordered lateral packing of collagen molecules in some fibrils. Other tissues for example calf Achilles tendon, skin and cartilage only exhibit a diffuse equatorial maximum with no discrete diffraction patterns.

4 Materials and Methods

4.1 Sample Preparation

All tissue/implant sections described here and in the following chapters were provided through a collaboration with Dr Krishna Burugapalli from the Brunel Institute of Bioengineering, Brunel University. A subcutaneous implantation series, involving a range of implant chemistry and nanoscale porosities, was carried out on adult Sprague–Dawley rats (175 – 200 grams body weight). These rats were randomly divided into two groups (n = 3/group) in order to study fibrotic tissue formation at two different time points.

Implantation Methodology

In each animal, six types of implants with different morphologies, porosities and chemical structures were implanted. The full description of the implant types is given in **Table 4.1**, and a range of types was chosen to stimulate different degrees and types of host inflammatory response, which will affect the formation of the fibrous capsule as described in **Section 3.3**. As reported in **Table 4.1** the sheet implants had dimensions of 10 mm (width) $\times$ 10-15 mm (length) $\times$ variable 30-300 μm (thickness) and were implanted on the back of each rat. The position of the implants was randomized, with each rat receiving one of each implant type (refer to **Table 4.2**). 3 implants were implanted on each side of the dorsal midline, about 2 cm away from the midline, with each implant separated from the other by a minimum of 3 cm (**Figure 4.1**). Rats in both groups were euthanized at 4 weeks and 9 weeks, respectively, and implant sites including implants and surrounding tissue were explanted. The explanted tissue were fixed with RCL2® a formalin-free tissue fixative which does not crosslink the tissue [126] and were processed for histopathology, X-ray scattering and micro-mechanical analysis.

Preservation of cells and tissues as they naturally occur is a crucial part of all histological techniques. Fixatives prevent autolysis by inactivating lysosomal enzymes and stabilize fine structures inside and between cells by making macromolecules resistant to dissolution by water and other liquids. The growth of bacteria and molds that lead to putrefactive changes is inhibited by fixatives [127]. RCL2® was used as a fixative in all implant-induced fibrosis samples based on a preliminary test using mouse skin. Mouse skin samples with intact epidermis, dermis, muscle and subcutaneous layers were fixed in Neutral Buffered Formalin (NBF) solution, RCL2® solution and snap frozen to determine the best method to use for all samples. NBF solution is a 4% aqueous solution of formaldehyde and fixes by adding to the side-chains of basic amino acids and to the amide nitrogen atoms of peptide linkages. When two formaldehyde binding sites are close together, cross-linking methylene bridges are formed [127]. RCL2® on the other hand, is a formalin-free tissue fixative which does not crosslink the tissue [126].

Mouse skin samples fixed in NBF and RCL2® solutions were washed in phosphate buffered saline (PBS) solution over a period of two days to ensure all traces of fixative were removed. The dermis was then separated from the muscle and subcutaneous layers using forceps. Samples stored in NBF solution were found to be more difficult to handle and became very mucus like. Samples fixed in RCL2® solution on the other hand, remained intact. Snap frozen samples were eventually dropped from the evaluation as it was not feasible to transport them between facilities for testing and evaluation. Samples intended for snap freezing should be transported on top of wet ice, on saline-dampened gauze and rapidly frozen within two hours. Samples should not be allowed to freeze slowly or to soak up excess saline, as these will cause artifacts that are visible microscopically and will interfere with any interpretation [127]. Based on these observations, RCL2® was chosen as the fixative for use in all implant-induced fibrosis samples.

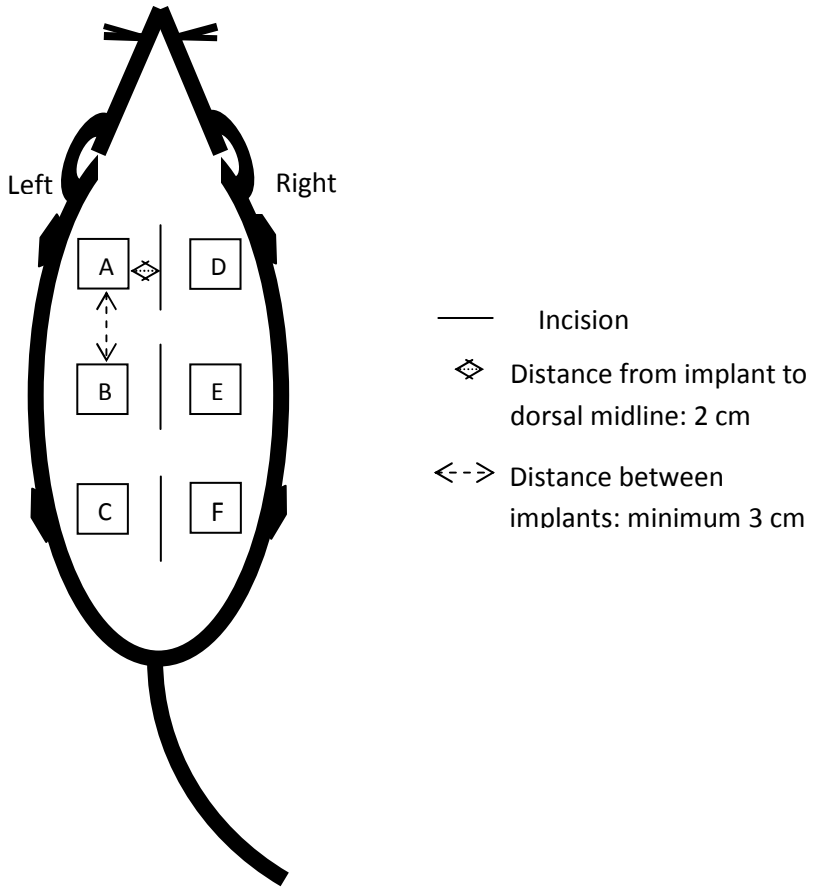

***Figure 4.1**: Implant positions in Rat 1.*

Preparation of sections

Once tissue has been fixed, it must be processed into a form which allows the samples to be sliced into thin sections. This is typically done using paraffin wax. The process of embedding fixed tissue in paraffin is called tissue processing. The main steps in this process are dehydration and clearing which are essential as wet samples cannot be directly infiltrated with paraffin. Tissue processing using paraffin wax is advantageous as the blocks are durable, cutting qualities are good and most importantly, tissues can be stored long term without any deterioration [128].

Tissue sections were placed in embedding cassettes and embedded in paraffin wax using the protocol outlined in **Table 4.3**. Ethanol was used to gradually dehydrate the tissue sections before Xylene (a clearing agent) was introduced. The dehydration process is critical to ensure all traces of water are removed as water and paraffin are not miscible [127]. The clearing process

involves the removal of the dehydrant (ethanol) with xylene, a substance that is miscible with the embedding medium (paraffin). Tissue sections were subsequently placed in molten paraffin wax, heated to 60°C, for 12 hours. Once processed, the tissue was oriented into a paraffin block and subsequently sectioned (see **Figure 4.2**). One key consideration is that tissue hardens upon fixation and remains in the shape it was fixed in. This is critical in cases where final orientation of the section is important. Sectioning was performed using a Leica RM 2145 semi-motorized rotary microtome (Meyer Instruments, Houston, TX, USA). 3 to 5 sections were sliced at 300 µm thickness.

The sliced sections were then dewaxed for synchrotron testing using the protocol described in **Table 4.4**. Briefly, the samples were immersed in xylene which is an excellent solvent for removing paraffin followed by dehydration in ethanol. They were then stored in a physiological PBS solution at 4°C. The dewaxing protocol is crucial to ensure wax is completely removed from the tissue section as residual paraffin wax can give a strong signal in synchrotron X-ray scattering measurements. The time taken in each process step was determined by using Raman spectroscopy (see **Figure 4.3**). A 300 µm wax embedded tissue section was dewaxed using the protocol described in **Table 4.4**. Raman spectra were collected using Nicolet Almega XR dispersive Raman spectrometer (Thermo Fisher Scientific Inc, WI USA). The integrated Olympus BX-51 microscope is equipped with three objectives (100x, 50x and 10x). The 10x objective was used for data collection. Samples were placed on a motor-controlled stage, and manually focussed. A 785 nm laser wavelength was used as the excitation source. The laser power was set at 100%, while the exposure time and number of exposures were set at 1 second and 128, respectively. Background spectra was collected and automatically subtracted from the sample spectra. OMNIC software (v.7.2a Thermo Electron Corporation) was used to collect spectra and configure Raman settings. Raman spectra were collected pre- and post-dewaxing and compared to Raman spectrum of paraffin wax. As illustrated in **Figure 4.3**, the spectrum of paraffin wax clearly shows distinctive Raman contributions at the 1063 cm^{-1}, 1133 cm^{-1}, 1296 cm^{-1} and 1441

cm^{-1}. These peaks are not visible in the spectrum collected on the 300 µm tissue section post-dewaxing indicating that the dewaxing protocol successfully removed all traces of wax.

Prior to synchrotron testing, these samples were mounted onto 30 mm x 30 mm sample holders, as illustrated in **Figure 4.4**. Samples were mounted between two X-ray transparent thin polymer window films (Ultralene®, Spex SamplePrep Metuchen, NJ, USA), filled with PBS and then gripped in place using two plastic plates, with an O-ring and 4 screws situated symmetrically on all four sides. These samples were used in the synchrotron scanning X-ray scattering and diffraction investigations, to be discussed in **Section 4.2**.

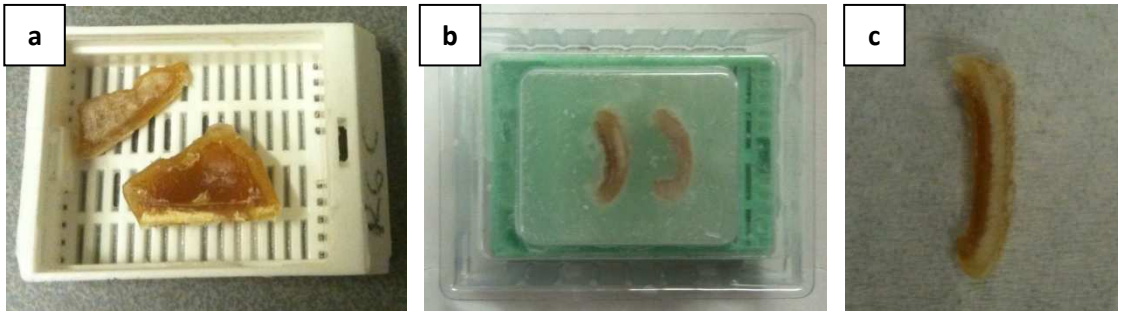

***Figure 4.2**: Sample preparation: (a) Sample R6c post processing, (b) tissue oriented into a paraffin block, and (c) tissue post microtome sectioning.*

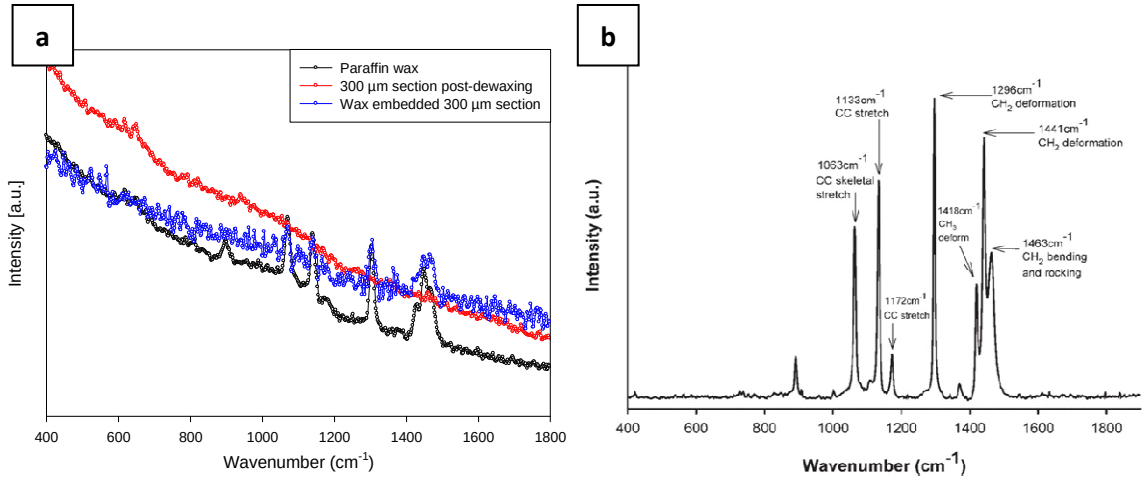

***Figure 4.3**: (a) Dewaxing protocol efficacy test and (b) reference Raman spectrum of paraffin wax [128].*

***Table 4.1**: Implant material and thickness.*

Implant	Implant material	Thickness
A	Electrospun polyurethane mesh, 8%, fibre diameter ≈ 300 nm	30 µm
B	Polyurethane film, nonporous/ nanoporous < 10 nm pore size	100 µm
C	Coaxial fibre mesh with polyurethane core and a shell of gelatine crosslinked with glutaraldehyde, 6%, fibre diameter ≈ 1100 nm	50 µm
D	Electrospun polyurethane mesh, 12%, fibre diameter ≈ 1200 nm	80 µm
E	Semi- interpenetrating network (IPN), HEMA-DHPMA-NPV-EGDMA crosslinked gel interpenetrating with non-crosslinked gelatine	200-300 µm
F	Full IPN, HEMA-DHPMA-NPV-EGDMA crosslinked gel with gelatine crosslinked with glutaraldehyde	200-300 µm

***Table 4.3**: Tissue processing and paraffin-wax embedding procedure.*

Process	Solution	Time
Dehydrate	70% Ethanol	2 hours
Dehydrate	90% Ethanol	2 hours
Dehydrate	100% Ethanol	2 hours
Clearing agent	100% Xylene	2 hours
Clearing agent	100% Xylene	2 hours
Infiltrate	Paraffin (at 60°C)	12 hours

***Table 4.4**: Tissue section dewaxing procedure.*

Process	Solution	Time
Solvent	100% Xylene	1.5 hours
Solvent	100% Xylene	1.5 hours
Solvent	100% Xylene	1.5 hours
Solvent	100% Xylene	1.5 hours
Dehydrate	100% Ethanol	1 hour
Dehydrate	100% Ethanol	1 hour
Dehydrate	95% Ethanol	1 hour
Dehydrate	70% Ethanol	1 hour
Dehydrate	50% Ethanol	1 hour
Rehydrate	Distilled water	1 hour
Rehydrate	Distilled water	1 hour

***Table 4.2**: Implant location in all six rats.*

Time points	Rat #		Implant	Implant thickness	Location on rat
4 weeks	R1	R1a	A	30 µm	Left Neck Right R1a R1d R1b R1e R1c R1f
		R1b	B	100 µm	
		R1c	C	50 µm	
		R1d	D	80 µm	
		R1e	E	200-300 µm	
		R1f	F	200-300 µm	
	R2	R2a	F	200-300 µm	R2a R2d R2b R2e R2c R2f
		R2b	D	80 µm	
		R2c	E	200-300 µm	
		R2d	C	50 µm	
		R2e	A	30 µm	
		R2f	B	100 µm	
	R3	R3a	E	200-300 µm	R3a R3d R3b R3e R3c R3f
		R3b	C	50 µm	
		R3c	A	30 µm	
		R3d	B	100 µm	
		R3e	F	200-300 µm	
		R3f	D	80 µm	
9 weeks	R4	R4a	D	80 µm	R4a R4d R4b R4e R4c R4f
		R4b	E	200-300 µm	
		R4c	F	200-300 µm	
		R4d	A	30 µm	
		R4e	B	100 µm	
		R4f	C	50 µm	
	R5	R5a	C	50 µm	R5a R5d R5b R5e R5c R5f
		R5b	A	30 µm	
		R5c	B	100 µm	
		R5d	F	200-300 µm	
		R5e	D	80 µm	
		R5f	E	200-300 µm	
	R6	R6a	B	100 µm	R6a R6d R6b R6e R6c R6f
		R6b	F	200-300 µm	
		R6c	D	80 µm	
		R6d	E	200-300 µm	
		R6e	C	50 µm	
		R6f	A	30 µm	

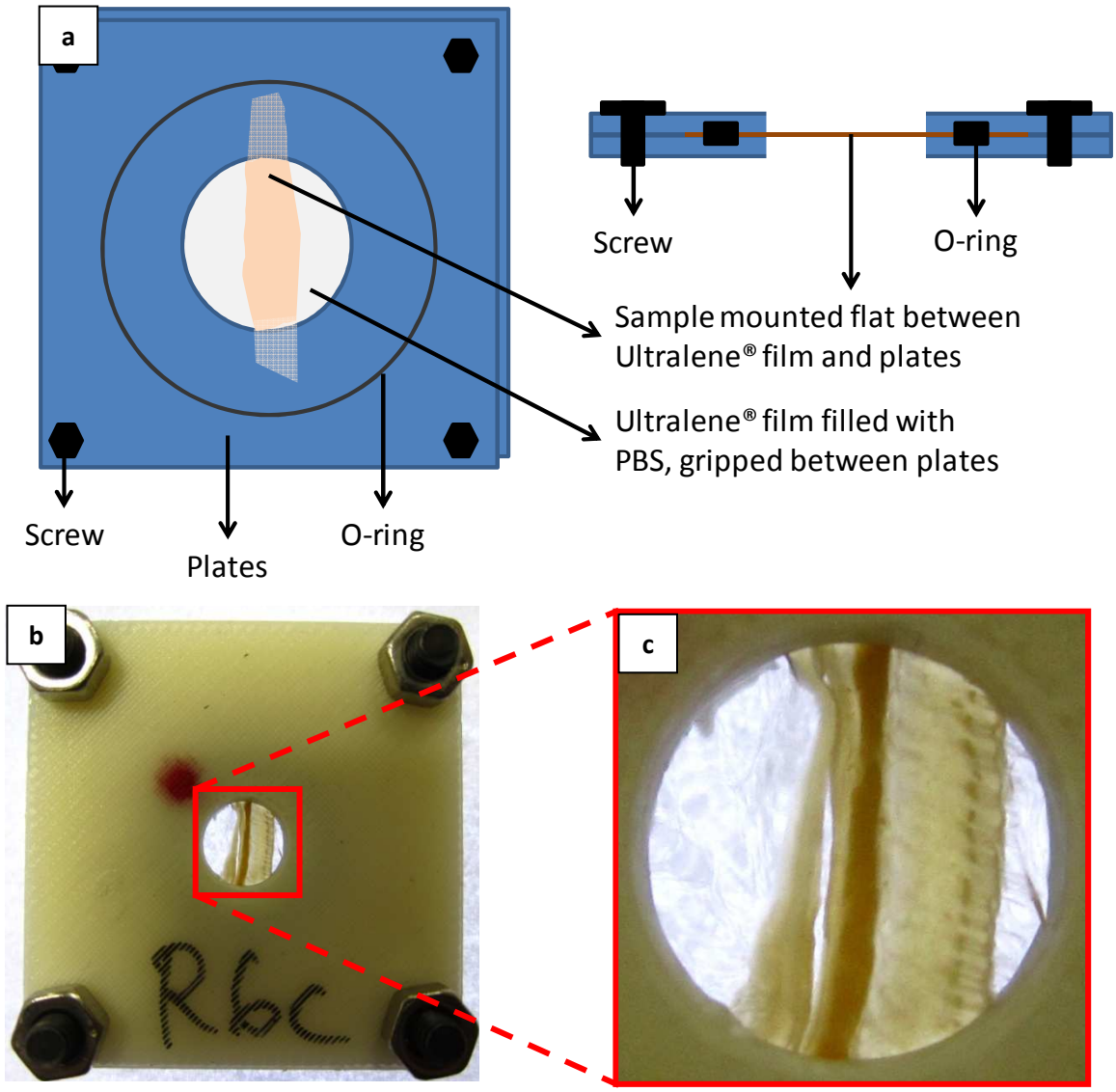

***Figure 4.4**: (a) Front view and cross-sectional view of sample holders used for scanning X-ray scattering and diffraction studies, (b) sample R6c mounted in sample holders, and (c) enlarged image of sample R6c. The O-ring ensures that the PBS does not leak out during the experiment as the sample holder is in an upright position during testing.*

4.2 X-Ray Scattering and Diffraction

In 1895, Wilhelm Conrad Röntgen, a German physicist, discovered X-rays; so named due to their unknown nature. Röntgen was later awarded the Nobel Prize in Physics 1901 *"in recognition of the extraordinary services he has rendered by the discovery of the remarkable rays subsequently named after him"* [129]. X-rays are electromagnetic radiation with a wavelength much smaller than that of visible light. The phenomenon of X-ray diffraction by crystals was however, only discovered in 1912 by Max von Laue, a German physicist who received the Nobel Prize in Physics 1914 for his discovery [130]. Van Laue showed that regular arrangement of atoms in crystals could produce diffraction spots with X-rays. X-rays used in X-ray crystallography have wavelengths approximately in the range 0.5 to 2.5 Å [131-132]. It is also important to mention the subsequent application of X-ray diffraction by two English physicists, Sir William Henry Bragg and William Lawrence Bragg to the study of crystal structure [133].

Scattering and diffraction techniques are better suited for quantification of nanostructures as real-space imaging using X-rays (such as microradiography) is not capable to resolve structures at the nanometre scale. X-ray scattering and diffraction techniques allow non-destructive quantitative analysis of biological systems and are frequently used to investigate these structures at the nanometre level. When exposed to x-rays in transmission mode, hierarchically structured materials give scattering and diffraction patterns in both SAXS [134-135] and WAXD regimes [136-139]. In combination, these techniques allow the construction of quantitative images of nanostructural parameters with micrometre scanning resolution.

4.2.1 Principles

Scattering and Diffraction

The interaction between X-rays and the charge distributions in atomic matter leads to the absorption and scattering of the X-rays. The terms scattering and diffraction both refer to an interaction between waves or photons and the atoms of an object. Scattering occurs when the object is made up of unordered atoms whereas diffraction occurs when waves or photons interact with ordered atoms [140-141]. Scattering can be distinguished by the arrangement of atoms. Diffuse scattering occurs by weak scattering of randomly arranged atoms in space in all directions. In the case of scattering by atoms arranged periodically in space, i.e. in a perfect crystal, scattering can occur in two different modes. The first is known as diffraction where strong scattering takes place in very few directions, satisfying Bragg's law. In the second mode, scattering occurs in most directions and does not satisfy Bragg's law; hence no scattering occurs as the scattered rays cancel one another. Diffraction may be defined as "a beam composed of a large number of scattered rays mutually reinforcing each other" [131]. As such, diffraction is essentially a scattering phenomenon.

In elastic scattering (see **Figure 4.5**), the relationship between the scattering vector $\vec{q}$ and the scattering angle 2θ is given by:

$$\vec{q} = \frac{4\pi}{\lambda} \cdot \sin\frac{2\theta}{2} \quad (when\ \vec{k} = \vec{k}')$$

where λ is the wavelength, $\vec{k}$ is the incident beam, $\vec{k}'$ is the scattered beam and 2θ is known as the Bragg scattering angle.

The measured scattering intensity $I(\vec{q})$ is related to the square of the Fourier transform of the electron density distribution $\rho(\vec{r})$ by the following equation:

$$I(\vec{q}) = K\frac{d\Sigma}{d\Omega}(\vec{q}) = \frac{K}{V}\left|\int_V \rho(\vec{r})\exp(i\vec{q}\vec{r})d^3r\right|^2$$

where $\vec{q}$ is the scattering vector as depicted in **Figure 4.5**, *V* is the total irradiated sample volume, *K* is a constant and $\frac{d\Sigma}{d\Omega}(\vec{q})$ corresponds to the macroscopic differential scattering cross section of the sample.

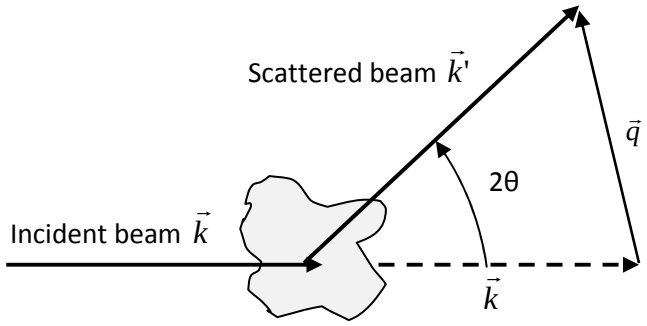

Figure 4.5*: Elastic scattering of X-rays, showing incident ($\vec{k}$) and scattered ($\vec{k}'$) beams. The scattering wave vector q is also shown.*

Bragg's Law

Bragg's law states the essential condition which must be met if diffraction is to occur. Bragg's law refers to the following equation:

$$m\lambda = 2 \cdot d_{hkl} \cdot \sin\theta$$

where *m* is an integer, *(hkl)* are the Miller indices of the crystallographic plane and d_{hkl} is the interplanar spacing between planes.

Since sin θ cannot exceed 1, the above equation can be written as:

$$\frac{m\lambda}{2d_{hkl}} = \sin\theta < 1$$

Therefore, $m\lambda$ must be less than $2d_{hkl}$. The smallest value of m is 1 in the case of diffraction (m = 0 cannot be observed as this corresponds to the beam being diffracted in the same direction as the incident beam). Thus, λ must be less than $2d_{hkl}$ at any observable angle 2θ.

Bragg's law can be written as follows:

$$\lambda = 2 \cdot \frac{d_{hkl}}{m} \cdot \sin\theta$$

Sharp Bragg peaks are observed if atoms are perfectly ordered in a crystalline structure. If atoms are randomly oriented, these peaks have a lower intensity and a larger width.

In the one dimensional case, the coordinate of the reciprocal space $\vec{q}$ is inversely related to the coordinate in real space by the following equation:

$$\vec{q} = m\frac{2\pi}{d}\vec{n}$$

where $\vec{n}$ is a unit vector.

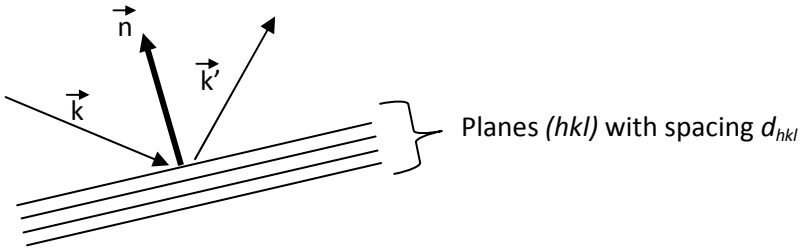

***Figure 4.6**: Bragg's law depicting the incident and diffracted beams. In a mirror condition, $\vec{n} // \vec{q}$*

4.2.2 Small Angle X-Ray Scattering and Wide Angle X-ray Diffraction

Small angle X-ray scattering research began in the late 1920s and early 1930s with natural fibres, in particular cellulose, as well as colloidal coal. It was in 1938 that Andre Guinier, a solid-state physicist and crystallographer, proposed his concept of particulate scattering or X-ray small

angle scattering of an isolated particle. The theoretical framework was provided by Günther Porod [141].

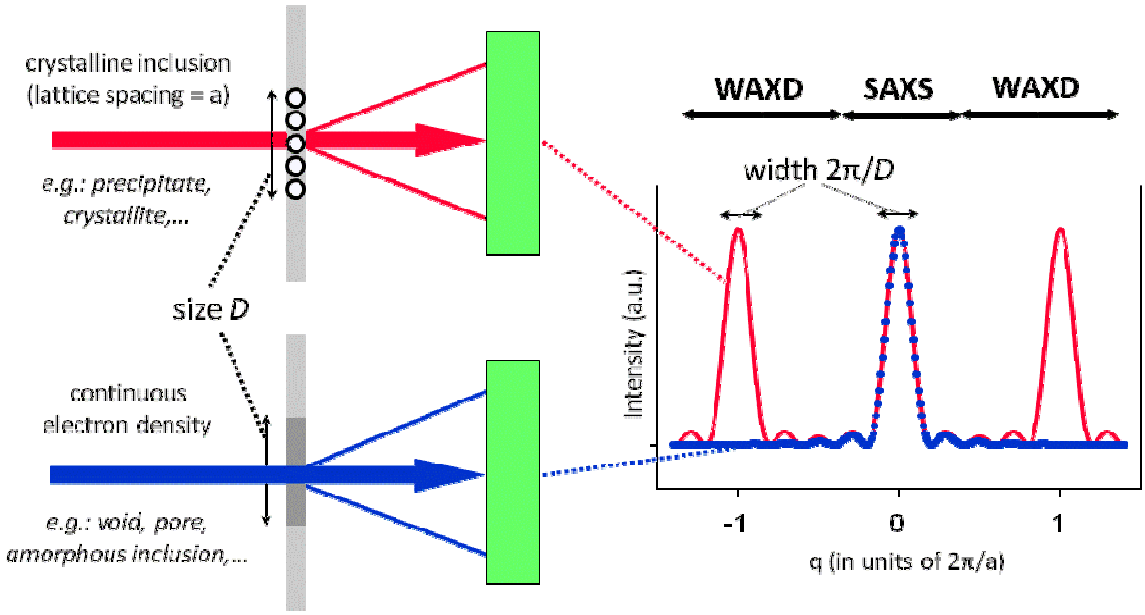

***Figure 4.7**: Small angle X-ray scattering and wide angle X-ray diffraction. D denotes the size of the lattice.*

The differentiation between small and wide angles in SAXS and WAXD is made on the basis of a critical angle. SAXS is diffuse scattering at angles smaller than 5° around the primary beam for incident X-rays generated by a Cu-Kα source (λ = 1.54 Å). It is sensitive to structures in the range of 1 – 50 nm. This enables characterization of randomly oriented systems and statistically distributed structures of colloidal (nanometre) dimensions including polymers, fibres, metals, alloys, glasses, ceramics, colloids, liquid crystals and biological materials [134, 137, 140]. The difference between SAXS and WAXD is illustrated in **Figure 4.7**. In the small angle regime, both scattering and diffraction are present, whereas in the wide angle regime only diffraction from crystallographic lattices arises. Small angle X-ray diffraction (SAXD) is a special case of SAXS, and typically appears in long period structures such as tropocollagen molecules, where the axial stacking generates a periodicity in electron density at the scale of tens of nanometres. WAXD patterns recorded at large Bragg angles reflect the crystal structure and crystallinity of materials providing information at the atomic level, while SAXS which is diffuse scattering at small angles is

sensitive to non-perfectly arranged structures at 1 – 100 nm length scales for nanostructure analysis [137].

Regardless of the crystallinity of a material, information on the size of small particles or their surface area per unit volume can be attained by the amount and angular distribution of the scattered intensity in SAXS. In SAXS, the two-dimensional scattering pattern obtained using an area detector, as shown in **Figure 4.8**, results in a two-dimensional section of $I(\vec{q})$ perpendicular to the incident beam. The shape of the SAXS signal (typically elliptical or the special elliptical case of circular symmetry) arises based on the shape and ordering of the particles embedded in the scattering object. A broadening in scattering signal in reciprocal space is inversely proportional to the dimensions of the scattering object in real space, as follows:

$$q_y \propto \frac{2\pi}{H}, \qquad q_x \propto \frac{2\pi}{W}$$

where H is the height and W is the width of the scattering object. This is depicted in a three-dimensional case in **Figure 4.8** where small dimensions in real space appear large in reciprocal space and vice versa.

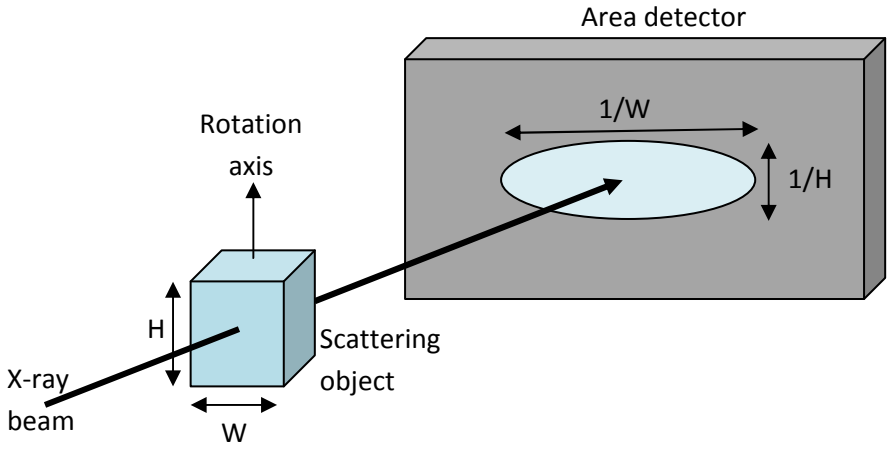

***Figure 4.8**: SAXS: correlation between real and reciprocal space in a three-dimensional case, where small dimensions in real space appear large in reciprocal space and vice versa.*

In WAXD, the diffracted X-rays from a polycrystalline material are on a cone for each lattice plane. The intersection of this cone with the detector plane gives rise to a ring of strong diffracted intensity on the detector plane, and the collection of these rings for all lattice planes are known as the Debye-Scherrer rings. These rings form at an angular distance of 2θ (where 2θ is the Bragg angle defined previously) with the direction of the primary beam (see **Figure 4.9**). Information on the orientation of lattice planes can be obtained from the intensity variation along the diffraction rings [142].

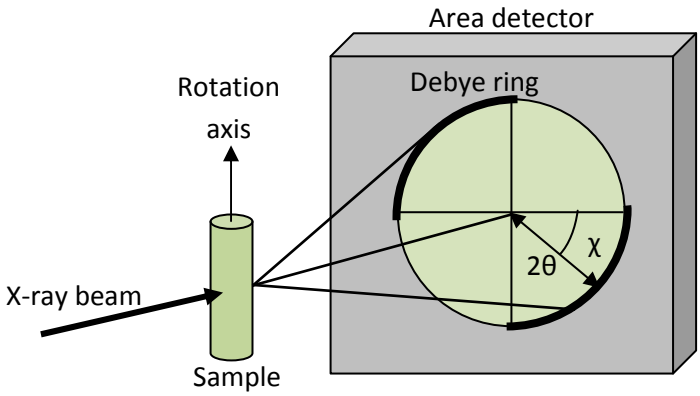

Figure 4.9*: WAXD: Debye-Scherrer rings form when the X-ray beam illuminates the sample, diffracting the X-ray on a cone and intersecting the detector plane. Adapted from [142].*

SAXS/SAXD and WAXD patterns from molecular and supramolecular packing of collagen

Due to the triple helical structure of the tropocollagen molecules [143-144] and the regular spacing of amino acids along a single amino acid chain, the WAXD spectrum from collagen tissue shows a distinct peak corresponding to a lattice spacing of 0.29 nm [145], which is the average spacing of amino acids along the chain (**Figure 4.10** (b) and (d)). Changes in the intensity of this peak may correspond to changes in either the volume-fraction of tropocollagen molecules in the scattering volume or possibly in the degree of maturity of the tissue, with less mature tissue leading to lower WAXD intensities.

Concurrently, the axial arrangement of these tropocollagen molecules into the collagen fibril (diameter 50-200 nm) is also highly regular. Due to the necessity of minimizing hydrophobic interactions between adjacent chains, the molecules do not line up in parallel but in a staggered arrangement as shown schematically in **Figure 4.10** (b). When combined with a gap between sequential tropocollagen molecules, the overall arrangement of molecules in the fibril results in the "gap-overlap" arrangement [20, 23] depicted in **Figure 4.10** (b) where regions of high molecular packing (and concomitant high electron density) alternate with regions of lower molecular packing (and lower electron density). Such an axial periodicity in electron density, denoted *D*, is equivalent to a one-dimensional lattice of the type mentioned previously. It consequently gives rise to a series of Bragg reflections in reciprocal space along the fibril axis *(meridional)* direction (see **Figure 4.10** (a)), which can be picked up in the low angle regime of an X-ray detector due to the magnitude of $D \sim 65 - 67$ nm (depending on tissue type and degree of hydration) corresponding to a wave vector of $q_D = 2\pi/D$ of about 0.094 – 0.097 nm^{-1}. These are shown schematically in **Figure 4.10** (c).

Finally, the lateral spacing of the tropocollagen molecules in the fibril gives rise to diffraction peaks as well. The lateral spacing of the tropocollagen molecules ranges from 1.1 nm (in dry or fully calcified tissue) to 1.4-1.5 nm (in wet and/or uncalcified tissue). As a result, perpendicular to the meridional reflections arising from the D-periodicity, a diffraction peak denoted as the equatorial peak arises in the low-angle WAXD / intermediate SAXS range. As the lateral disorder in collagen packing is large (explanations have included the liquid-like ordering proposed by Woodhead-Galloway [146]), only the first order peak is usually observed, and is shown in **Figure 4.10** (a).

All the reflections described above are sensitive to external stimuli, which can range from physicochemical to mechanical. Specifically, as the D-period provides an internal length scale to the collagen fibrils, changes in the D periodicity can provide a direct measure of fibril strain along

the axial direction, when it is detectable. At a smaller length scale, shifts in the 0.29 nm tropocollagen WAXD reflection under mechanical loading provide a measure of mechanical strain at the molecular level. Lastly, fibrillar contraction can be assessed from shifts of the equatorial Bragg peak to larger *q*-values.

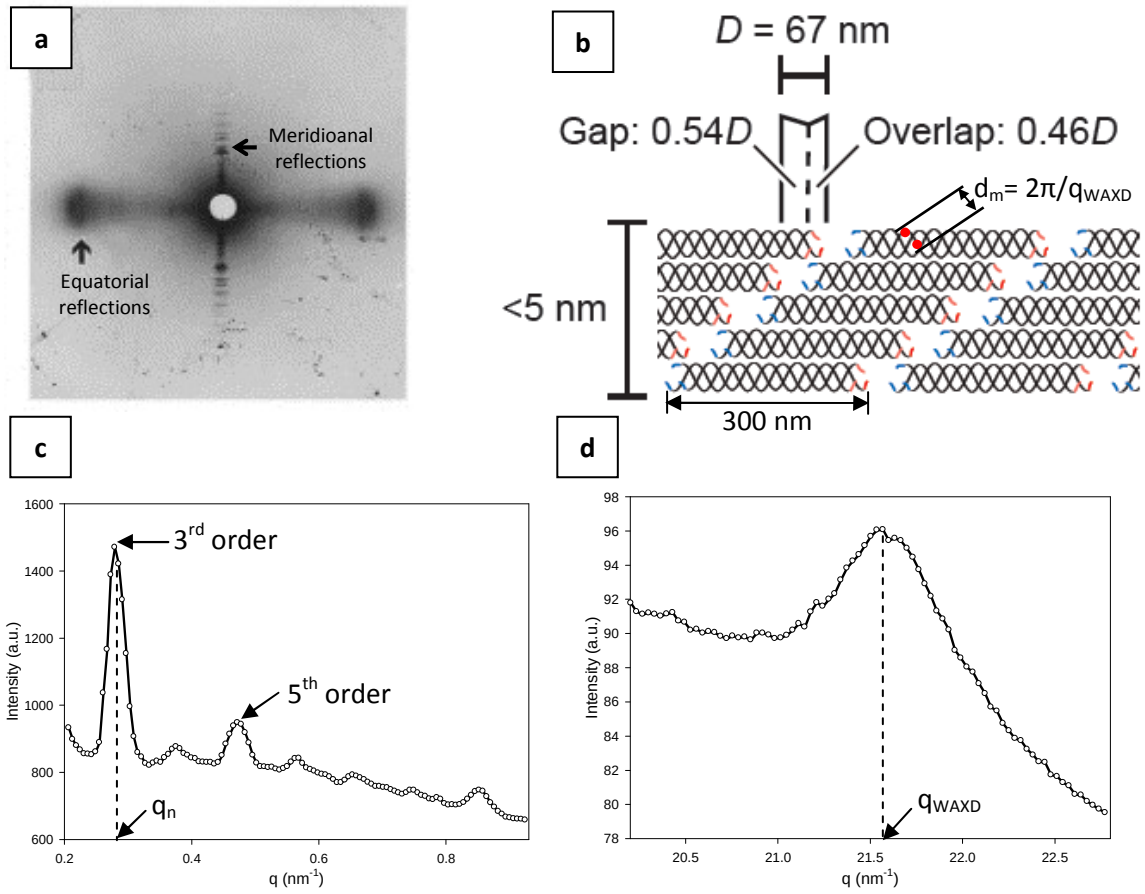

***Figure 4.10**: (a) Medium angle X-ray diffraction pattern of mouse tail tendon [147], (b) staggered arrangement of collagen molecule in a collagen microfibril giving rise to the axial spacing seen in (c) (where $q_n=2\pi n/D$ and n is the reflection order) and intramolecular spacing shown in (d).*

Scanning SAXS and WAXD

The combination of scanning along a sample with X-ray scattering techniques is an ideal method for detecting local micro- and nanoscale heterogeneities seen in hierarchical structures. The combination of SAXS and WAXD with focused X-ray beams for scanning with true micrometre resolution requires high photon fluxes which can only be provided by synchrotron radiation sources and highly efficient and fast detection systems. This technique is perfect for analysing anisotropic and inhomogeneous human tissue in which direct spatial resolution is desired. Scanning SAXS and WAXD provide information on the orientation of nanometre sized organic and inorganic components within the X-ray beam focused to diameters in the micrometre range.

Scanning SAXS and WAXD can be achieved using computer controlled stages allowing movement of the sample in the plane perpendicular to the beam, and a narrow X-ray beam which allows for position resolved analysis of biological tissue by scanning the sample across the x-ray beam. This method was developed for the investigation of hierarchically structured materials such as wood and bone [134-135, 137-138]. The total time for data acquisition for scanning SAXS and WAXD measurements depends on the number of spots in the raster scan and the exposure time used.

The position resolved small angle X-ray scattering analysis done by Fratzl et al. [134] was based on a conventional X-ray pinhole camera equipped with a two-dimensional position sensitive detector and a rotating-anode X-ray generator. The sample was moved in two directions, *x* and *y*, by computer controlled motorized stages. This allowed SAXS patterns to be collected at various positions of the sample at a spatial resolution of 200 µm. This technique was used to map the SAXS spectra of mineral particles in bone as well as the orientation and diameter of the cellulose fibrils in wood cell wall. Paris et al. [137] applied this method by combining SAXS and WAXD to study the thickness and orientation of mineral particles in human cancellous bone and at the bone-cartilage interface. Scanning SAXS and WAXD studies were also performed on wood to understand the orientation of cellulose fibrils in wood cell wall. Müller and co-workers [148]

recently used scanning SAXS to visualize and quantify the nanostructure of the bony tissue of human femoral head, the hard tissue of human tooth, thalamus as part of human brain and the urethra. Scanning SAXS spectra provided information on the collagen fibre orientation in bone as well as the difference in chemical composition and structure between dentin and enamel in human tooth.

Figure 4.11 illustrates the principle of the scanning technique used. The sample was moved in both *x* and *y* directions perpendicular to the X-ray beam. The beam stop is necessary as the intensity of the incoming beam is much higher than the scattered portion of the X-rays. For scanning SAXS, the detector is placed at a further distance from the sample and for scanning WAXD, the detector is moved closer to the sample. By changing the sample-to-detector distance, successive SAXS and WAXD measurements can be performed on the same location on the sample. SAXS is ideal for the detection of nanometre sized features between 1 nm and 1 µm, while WAXD covers the scales below until the atomic distances are reached [137, 148].

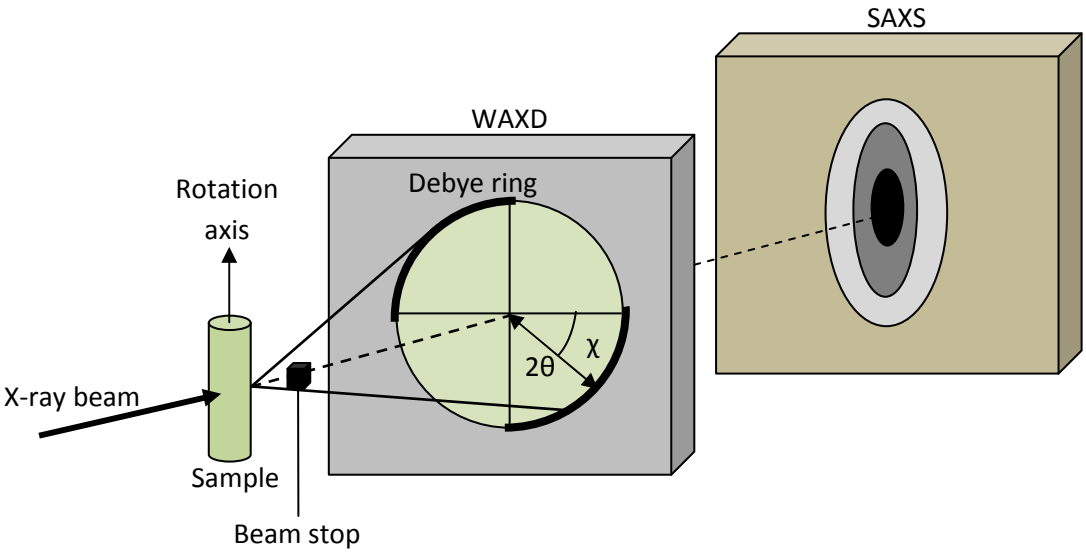

***Figure 4.11**: Scanning SAXS and WAXD setup. In SAXS configuration, detector is placed further from sample, whereas in WAXD the detector is moved closer to sample. Adapted from [137, 148].*

4.3 Synchrotron

All SAXS and WAXD measurements on fibrotic tissue presented in this thesis were performed using a synchrotron source. High intensity synchrotron x-ray sources have far evolved from the traditional source of incident radiation for x-ray diffraction using an evacuated tube containing a cathode and anode subjected to a high electrical potential. The very intense synchrotron light, predominantly in the X-ray region, is millions of times brighter than light produced from conventional sources. Synchrotron sources permit diffraction experiments to be carried out on very small crystals or on large biological molecules and allow weak magnetic scattering to be detected [149]. Synchrotrons were originally developed to study the basic constituents of matter. First generation synchrotrons were built for high-energy particle physics. Second generation synchrotron were dedicated to the production of synchrotron light. The third generation synchrotron widely available now (with about 40 large facilities around the world) produce even more intense and tuneable beams of synchrotron light [150].

Synchrotron radiation occurs when high energy electrons produced by an electric gun are accelerated at a speed close to that of light through a series of three particle accelerators, namely the linear accelerator, the booster synchrotron and the storage ring (see **Figure 4.12**). The linear accelerator, the first of the three particle accelerators, is used to accelerate the electrons to an extreme relativistic energy of a hundred million electron volts using radio frequency cavities. These electrons with an energy of 0.1 GeV then enter the booster where they follow a trajectory shaped like an "athletics track" with two straight sections joined together with semicircular curves. Dipole bending magnets are used to curve the electrons around the bends, and a radio-frequency voltage source is used to accelerate the electrons in the straight sections. Once the electrons reach an energy of 3 GeV, they are transferred into the storage ring. The storage ring is a polygon made of straight sections angled together with bending magnets or dipole magnets which are once again used to curve electron beams between adjacent straight

sections. The storage ring is maintained in high vacuum condition to minimize electrons scattering off air molecules. Synchrotron light is generated as the electrons travel at a speed close to that of light and are bent by a powerful magnetic field keeping them in the curved path of the storage ring. This light is then channelled out of the storage ring wall and into experimental stations called beamlines [149-150].

Each beamline is made up of four main sections, the front end, the optics hutch, an experimental hutch and a control cabin. The front end connects to the storage ring at a tangent and passes through the shield wall into the optics hutch. The five main functions of the front end are to allow light extracted from the storage ring to pass through to the beamline, monitor the position of the light, protect the storage ring in case of a leak in the beamline, remove as much heat as possible from the synchrotron light and allow safe access into the optics hutch as required. In the optics hutch, the incoming synchrotron light is filtered and focussed by optical devices like mirrors and diffraction gratings, into the experimental hutch where the light interacts with the sample being studied. The final hutch which is the control cabin is where scientists control the experiments and collect and analyse data obtained by the detectors [150].

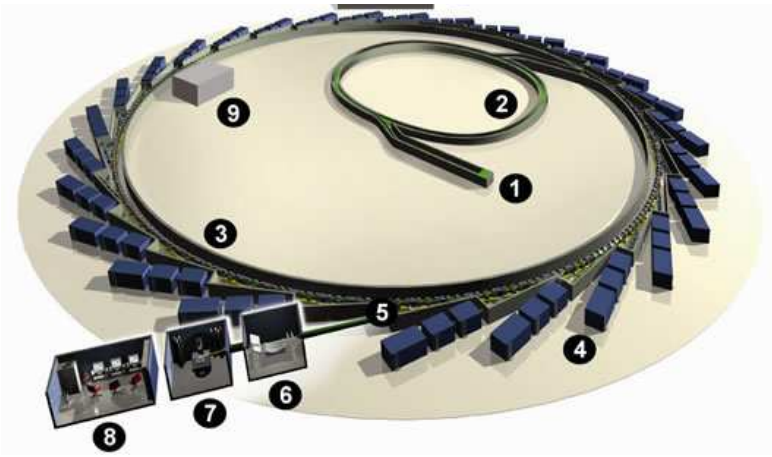

Figure 4.12*: The synchrotron machine. (1) Injection gun consisting of the electron gun and linear accelerator, (2) booster synchrotron, (3) storage ring, (4) beamlines, (5) front ends, (6) optics hutch, (7) experimental hutch, (8) control cabin, and (9) radiofrequency cavity [150].*

The rapid increase in beam brilliance at third generation synchrotron radiation sources have led to the development of microfocus beamlines (ID13 at the European Synchrotron Radiation Facility (ESRF, France) and I22 at Diamond Light Source (DLS, United Kingdom)). The principle scanning microfocus experimental setup at I22 beamline at Diamond Light Source is shown in **Figure 4.13**. Microfocus beamlines are crucial in imaging biomaterials as they allow utilization of smaller beam spot sizes of between 5 and 30 µm. By combining detectors of large active area and small pixel sizes with high photon flux and small beam divergence, the detector can be placed very close to the sample allowing optimization of the experimental setup for a small beam [139]. Microfocus synchrotron radiation has been widely used in studying bone structure and micromechanics [136, 151-153] as well as soft tissue and cornea [154-156].

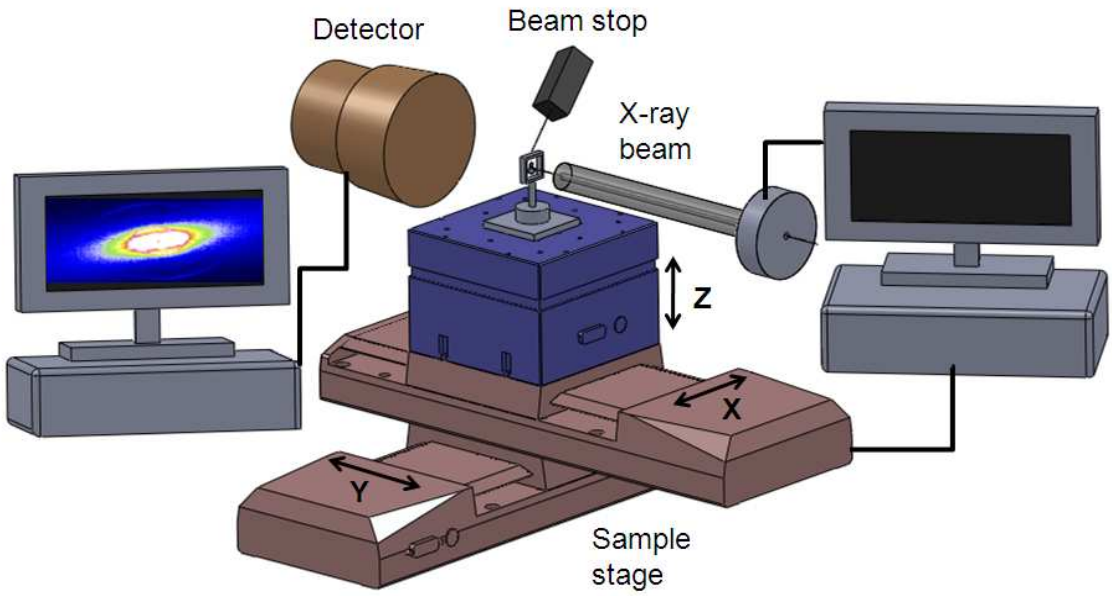

***Figure 4.13**: Scanning microfocus experimental setup at I22 beamline at Diamond Light Source, United Kingdom.*

4.4 Development of Micro-mechanical Tester

While it is not the focus of this thesis to understand the mechanisms controlling the normal or abnormal development at the fibrillar level in the fibrotic layer, a significant contribution towards this understanding has been completed. A micro-mechanical tester was designed and manufactured over a period of several months for future use in *in-situ* mechanical testing combined with synchrotron X-ray scattering and diffraction as well as Raman spectroscopy, which will link nano- and microscale fibrotic structure to mechanics at the fibrillar level in the fibrotic layer. The micro-mechanical tester allows for use in several different interchangeable configurations for use in both Raman spectroscopy and high brilliance synchrotron x-ray scattering and diffraction. The design and development processes are discussed in the following sections.

4.4.1 Design Process

The design process of the micro-mechanical tester was done according to an adaptation of the Pahl and Beitz systematic approach to engineering design. The process steps used are outlined in **Figure 4.14**. The Pahl and Beitz method was developed in the 1970s by two German professors and is based on a long tradition of German research. The fundamental idea behind this method is that design-based problem solving is a variant of general problem solving [157].

Phase 1 began with defining the product and design specifications. Information on the micro-mechanical tester requirements as well as the constraints was collected and is listed as follows:

- Samples must be immersed in PBS solution during testing in order to mimic the body's physiological condition.
- Micro-mechanical tester must allow for conversion between tensile testing and shear testing.

- Tester must allow for use in both the horizontal (see **Figures 4.17** (a) and (b)) and vertical (see **Figures 4.17** (c) and (d)) testing configurations. The micro-mechanical tester will be placed on a flat horizontal surface for tensile and shear testing of tissue samples. For *in-situ* synchrotron X-ray diffraction studies, the micro-mechanical tester will be placed in a vertical configuration to allow X-ray beam through the sample.
- Sample holders must be able to grip sample without causing slippage during testing and yet avoid placing any additional forces on the tissue sample.
- For *in situ* synchrotron X-ray diffraction studies, the fluid chamber depth must be optimum to minimize X-ray beam intensity absorption while at the same time minimize radiation damage caused by the X-ray beam. This last factor also depends on exposure time for each sample, which can vary between materials of different scattering power.

  Tester form factor must accommodate for potential use in combination with Raman spectroscopy to understand changes in molecular structure.

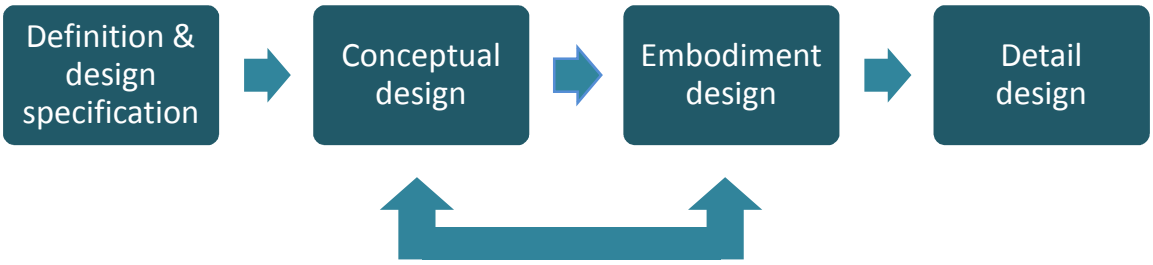

***Figure 4.14**: Micro-mechanical tester design process using Pahl and Beitz design methodology.*

In the conceptual phase, the specifications outlined in phase 1 were analyzed and potential problems were identified. The problems were then decomposed into sub-problems and solutions to these sub-problems were sought via brainstorming, patent searches and design catalogues. As per the Pahl and Beitz design methodology, emphasis was placed on this phase as fundamental failures in the concept are difficult to correct in later phases of design. A pencil

sketch of the initial design was made and discussed with peers. As this tester was designed with the potential usage in combination with Raman spectroscopy in mind, space restrictions had to be taken into account. Tester parts that had to be manufactured and parts that had to be purchased were identified.

Phase 3, the embodiment design phase, involved the development of preliminary layouts. Pencil sketches in phase 2 were transformed into three-dimensional drawings using the 3D design CAD software SolidWorks (2008, SP0.0, Dassault Systèmes, France). Several design alternatives were considered and the best preliminary layout was selected. This design was then refined and optimized based on function, manufacturability, assembly and cost effectiveness. For example, the material downselected for the fluid chamber had to be re-evaluated due to cost and manufacturing time concerns. The assembly view in SolidWorks allowed the detection of any possible dimensional mistakes and ensured that all the parts fit together. This phase concluded with the preparation of preliminary parts lists and drawings.

All detail drawings and parts lists were completed in phase 4, the detail design phase. Orders for parts to be purchased were made and manufacturing of parts was initiated.

4.4.2 Micro-mechanical Tester Parts and Assembly

The micro-mechanical tester was fitted with two digital linear actuators (RS Components, United Kingdom) which had a maximum force of 28.1N, nominal voltage of 12Vdc, maximum travel of 48 mm and an incremental motion of 0.0254 mm per step. Load was sensed using a 2kg load cell (ALD Mini-UTC, A.L. Design Inc., Buffalo, NY, USA). Two precision linear slide units (IKO Nippon Thomson, United Kingdom) were used to support the movement of the linear actuator leadscrew.

Two main parts were designed and manufactured; the sample holders as well as the fluid chambers. These are discussed in the following sections. Along with the sample holders and fluid

chambers, several small parts were also designed and manufactured in house; namely the base plate and stepper motor holders.

Sample holders

Two types of sample holders were designed; one for tensile testing (**Figure 4.15** (a)) and the other for shear testing (**Figure 4.15** (b)). Samples can be gripped between the bottom and top covers by placing sand paper in between to hold soft tissue.

Fluid chambers

Fluid chambers were included in the design in order to ensure samples were fully immersed in PBS solution during testing in order to mimic the body's physiological condition. These chambers were made out of clear plexiglass. For horizontal tensile and shear testing, a basic fluid chamber was manufactured (see **Figure 4.16** (a)). In the vertical configuration, designed for *in-situ* synchrotron X-ray diffraction studies, a new fluid chamber was required (**Figure 4.16** (b)). As X-rays are strongly absorbed in saline, the distance between the X-ray inlet and outlet had to be optimized. The optimization of the X-ray profile depth is key as radiation damage to the tissue sample is increased by a narrow profile depth. Two additional tubes were incorporated into the fluid chamber to shorten the X-ray path. The ends of the inlet and outlet tubes were covered with Ultralene® thin window film which is transparent to X-ray.

Micro-mechanical tester assembly

The parts which were designed and manufactured in house as well as the purchased parts can be assembled in four interchangeable configurations, as illustrated in **Figure 4.17**. Tensile and shear testing on fibrotic tissue can be done using the horizontal configurations (**Figures 4.17** (a) and (b), respectively). For *in situ* synchrotron X-ray diffraction studies, the vertical configurations depicted in **Figures 4.17** (c) and (d) can be used.

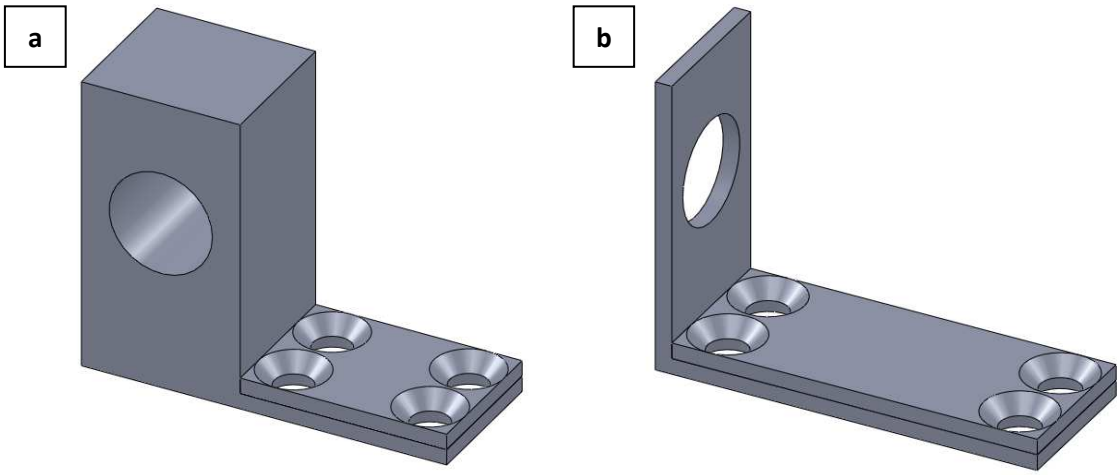

Figure 4.15*: Sample holders for (a) tensile, and (b) shear testing.*

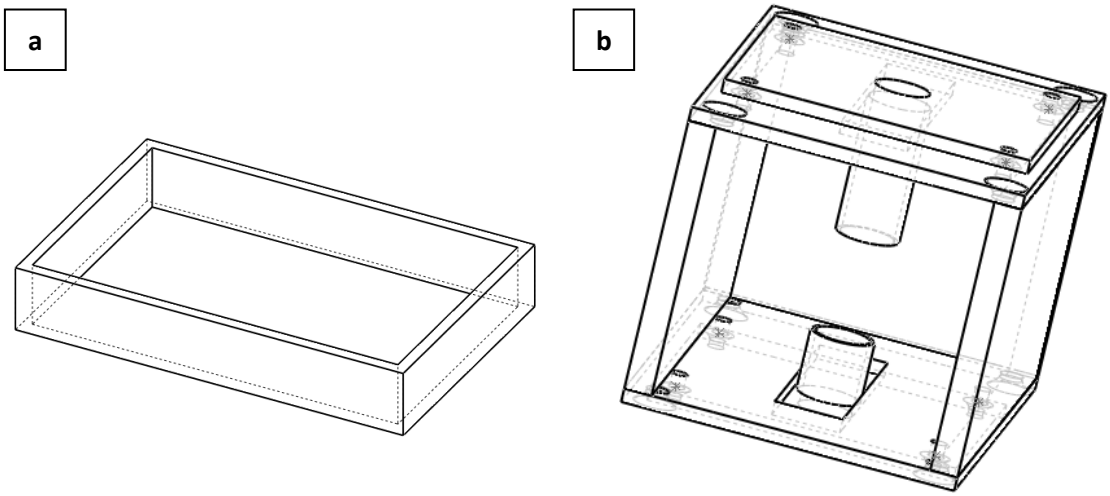

Figure 4.16: *Fluid chambers for (a) horizontal, and (b) vertical tester configurations.*

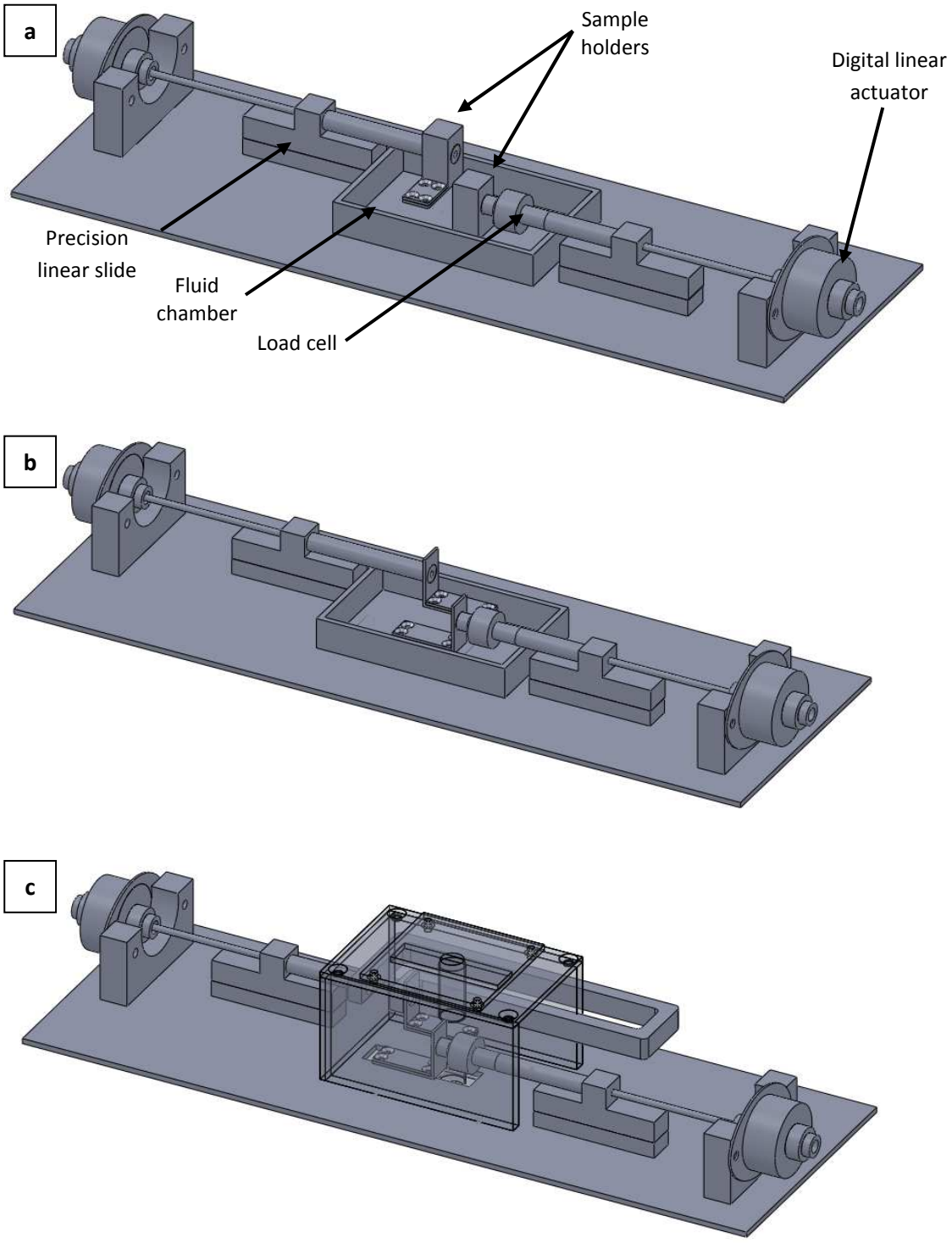
a
Sample holders
Digital linear actuator
Precision linear slide
Fluid chamber
Load cell
b
c

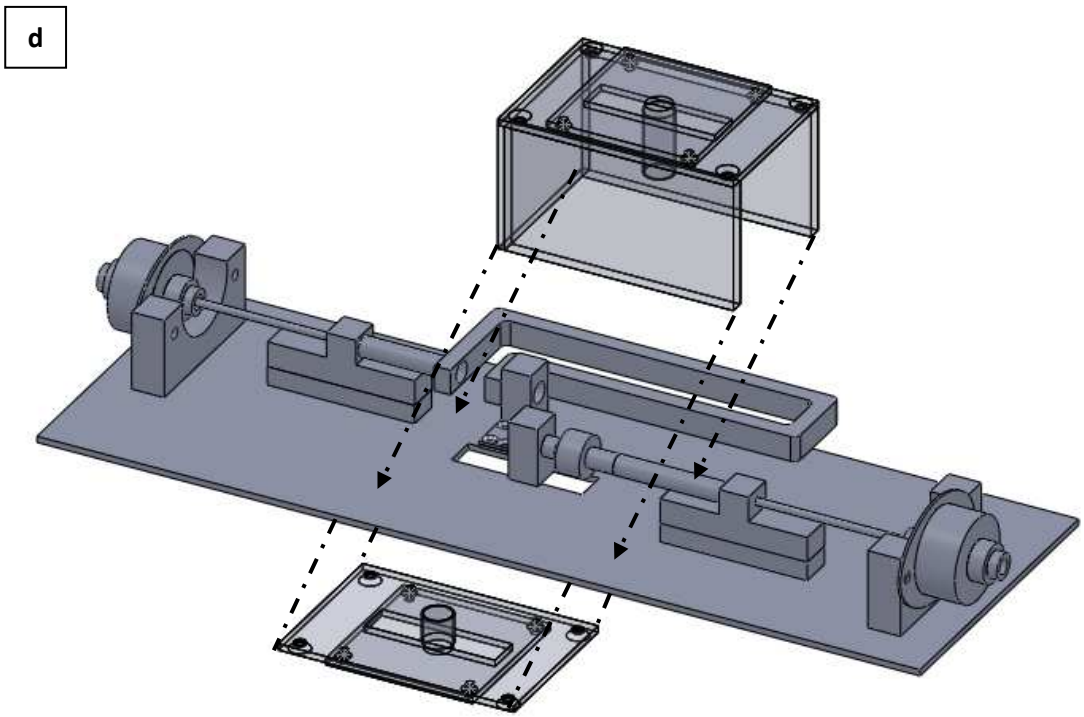

***Figure 4.17**: Micro-mechanical tester configurations: (a) horizontal tensile tester, (b) horizontal shear tester, (c) vertical shear tester, and (d) vertical tensile tester.*

5 Results and Discussion

Fibrotic tissue that forms around implants is primarily made up of Type III and Type I collagen, as is seen in the remodelling phase of wound healing [1]. The majority of research on axial fibril structure and lateral packing of collagen molecules within a fibril have been focused on bone and tendon, which is composed almost exclusively of Type I collagen and in which Type III collagen is absent. This is attributed to the fact that a high degree of crystallinity is present in homotypic collagen fibrils and the relative simplicity of modelling a system which contains only one collagen type [37]. A large number of fibrillar structures in tissues such as skin, aorta, colonic submucosa and cornea are, on the other hand, made up of heterotypic collagen fibrils, i.e. a combination of a number of different collagen types. These fibrils tend to exhibit a long periodic helical ultrastructure when studied using X-ray diffraction techniques [37]. The molecular organization within heterotypic fibrils is less well understood compared to homotypic collagen fibrils. There have been a small number of studies carried out to understand collagen architecture in skin [43, 122] and human breast tissue [158-161] which are composed of Type III and Type I collagen, as well as corneal fibrotic tissue which is composed of Type I and Type V collagen [125, 162-163]; but research into these areas is still very limited. Abnormalities of collagen molecular structure may affect collagen molecular packing in fibrillar forming connective tissues.

With the above in mind, the research in this thesis is focused on the nanostructural imaging of fibrotic tissue in subcutaneous implants using (static) scanning SAXS and WAXD using a microfocus (15 μm) synchrotron X-ray beam, to obtain a quantitative model of the fibrotic tissue in a static (undeformed) condition. In this chapter, I will present and discuss the results of a single (representative) implant type and time to demonstrate proof-of-principle of the novel microfocus synchrotron scanning SAXS and WAXD technique. Intramolecular amino-acid spacing, axial collagen periodicity, and degree of fibrillar orientation will be studied in fibrotic tissue

around the subcutaneous implant to demonstrate the promising application of this novel technique. These results will be the first SAXS-model for fibrotic tissue nanostructure and will be the foundation on which subsequent work can be based. It would be pertinent to highlight that to date, there has been very little research done in applying X-ray diffraction and scattering to the nanostructure of implant-induced fibrosis. The work presented here is, to the best of my knowledge, the first to combine microfocus spatial resolution and the quantitative potential of X-ray scattering and diffraction to characterize the fibrotic tissue nanostructure.

Sample preparation for the tissue specimens used in scanning SAXS and WAXD experiments have been discussed in **Section 4.1**. Sample holders (shown previously in **Figure 4.4**) were mounted on a 3-axis motorized linear high-precision elevation stage on a microfocus end station at beamline I22 at Diamond Light Source in Didcot, Oxfordshire, United Kingdom. In both SAXS and WAXD configurations, a synchrotron X-ray beam with a spot size of 13 µm by 15 µm and a wavelength, λ of 0.8857 Å with a 14 keV energy level were used. X-ray scattering was detected by a Pilatus 2M detector which has a pixel size of 172 µm by 172 µm and a total active area of 254 mm by 289 mm. A small tungsten wire beamstop was placed behind the sample to stop the primary beam from hitting the detector.

The detector position was changed to vary the sample to detector lengths required for both SAXS and WAXD measurements. The distance between the sample and detector in SAXS and WAXD configurations was 1007.8 mm (corresponding to a wave vector range of 0.18 to 1.21 nm^{-1}) and 489.3 mm (corresponding to a wave vector range of 20.2 to 22.8 nm^{-1}), respectively. The SAXS-configuration distance was determined using wet rat tail tendon, which has a known D-period of 67 nm as a calibration. Rat tail tendon was mounted and tested in the same manner as the fibrotic tissue specimens. The beam centre coordinate was calibrated using silver behenate in SAXS configuration and a silicon-standard in WAXD configuration. The silicon-standard was used to calibrate the WAXD-configuration distance as well. SAXS and WAXD line scans were

taken at locations on each sample predetermined by light microscopy imaging before the experiment. The line scan locations were mainly across the tissue/implant interface, which was horizontal (X-direction) in the sample holder. Line scans were done by moving the X stage horizontally using a step size of 15 µm (corresponding to the microfocus beam diameter). The exposure time for fibrotic tissue specimens as well as calibration specimens was 10 seconds. Data evaluation was done using the software package *FIT2D* [164] and all measured data was corrected for background as will be described in this section.

Line scans in both SAXS and WAXD configurations were done on a total of 17 samples over a range of implant types at both time points. Because each tissue/implant interface had a distinct geometry and shape, the SAXS and WAXD line scan locations varied slightly between samples in order for consistency and comparability. The line-scan locations for all 17 samples measured in this beamtime as well as the optical microscope images of stained tissue sections and camera images of actual samples mounted for SAXS and WAXD testing are shown in **Figure 5.**2. Several samples were mounted on the motorized holder to measure the samples one-by-one in an automated manner.

The results and discussion presented in this thesis will be focused on 1 sample (Sample R6c) with implant type-D (electrospun polyurethane (12%) mesh with a fibre diameter of about 1200 nm) at 9 weeks (see **Table 4.1** in **Section 4.1**). The methods used on Sample R6c will be applied to 3 other samples of implant type-D; 1 at 9 weeks (Sample R5e) and 2 samples at 4 week (Sample R1d and Sample R2d). Preliminary D-period calculations will be done using 1 sample (Sample R1b) from 4 weeks of implant type-B (nonporous/ nanoporous <10 nm pore size polyurethane film). As illustrated in **Figure 5.2**, it is difficult to determine the precise location of the fibrotic tissue in the optical microscope image of the actual tissue being tested. In addition to their utility in modelling the nanostructure, SAXS and WAXD data will help in determining the fibrotic tissue location in all samples.

5.1 Histology

As illustrated in **Figure 5.1**, generally three to four distinct layers can be distinguished from the implant surface upwards. On the immediate surface of the implant, a cell layer of 1 to 3 cells thick is present. This is followed by dense fibrotic tissue generated by the implant, which is of interest in this thesis. Adipose tissue is typically present in older rats. The next layer is loose connective tissue which can be distinguished into two layers based on the degree of vascularity. Blood vessels are present in the loose connective tissue layer adjacent to the dense fibrotic tissue. Subcutaneous smooth muscle is mainly composed of muscle cells held together by thin collagenous fibrous tissue.

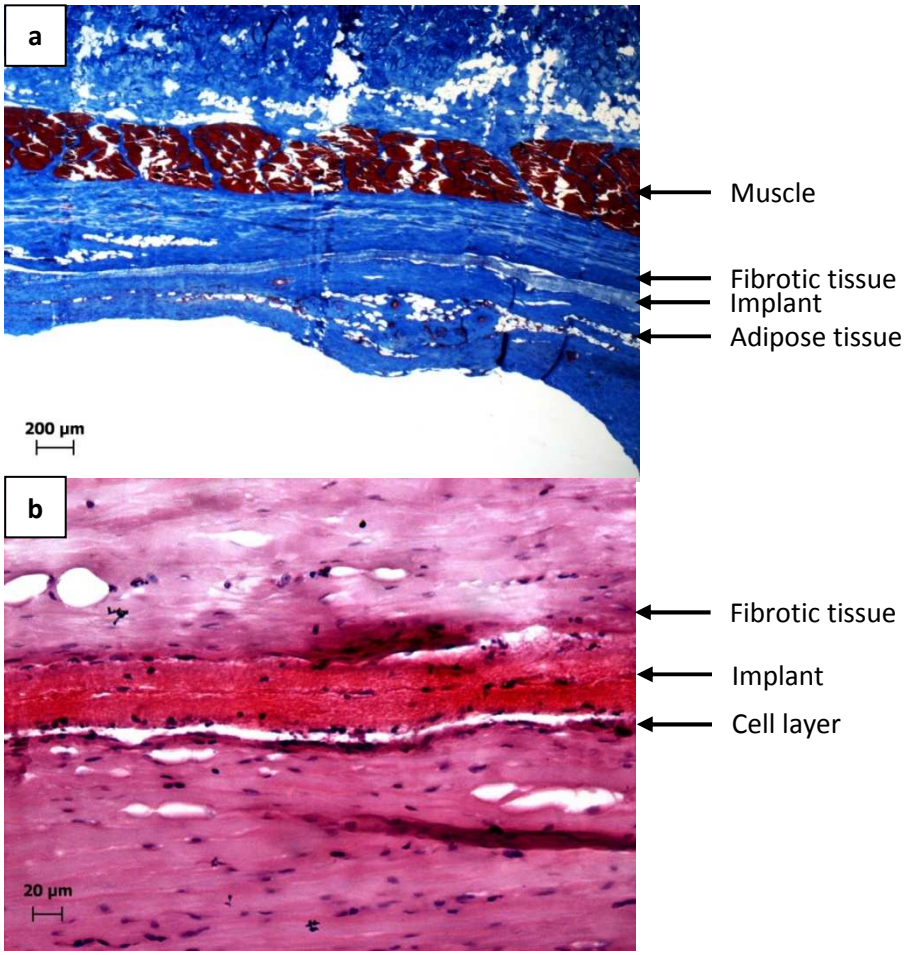

***Figure 5.1**: Optical microscope images of Sample R6c (a) Masson's trichrome staining and (b) enlarged image showing implant/ tissue interface Hematoxylin and eosin staining (images provided by Dr Krishna Burugapalli). Implant, fibrotic tissue and adipose tissue are indicated.*

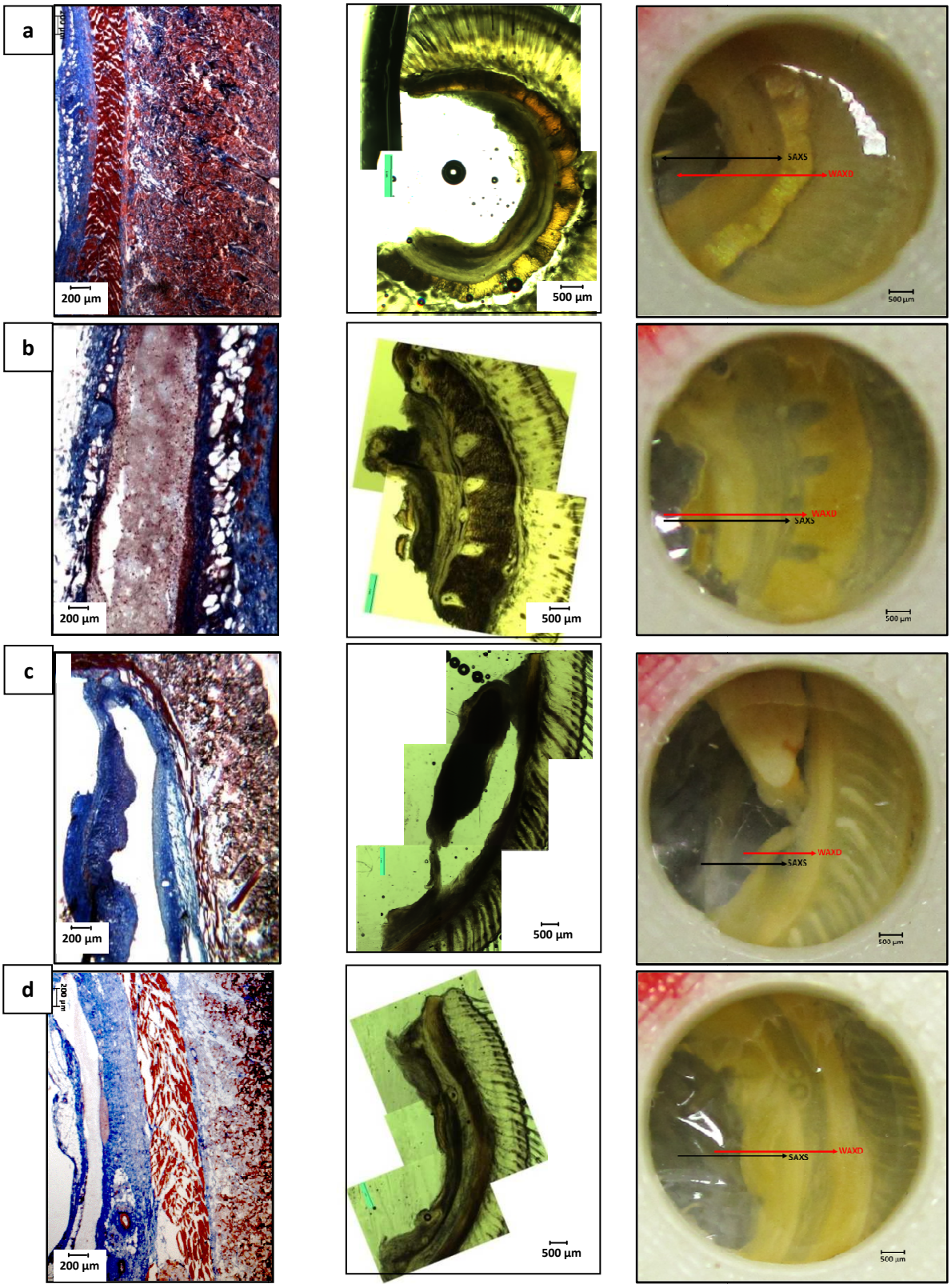
a
200 µm
500 µm
SAXS
WAXD
500 µm
b
200 µm
500 µm
WAXD
SAXS
500 µm
c
200 µm
500 µm
WAXD
SAXS
500 µm
d
200 µm
500 µm
SAXS
WAXD
500 µm

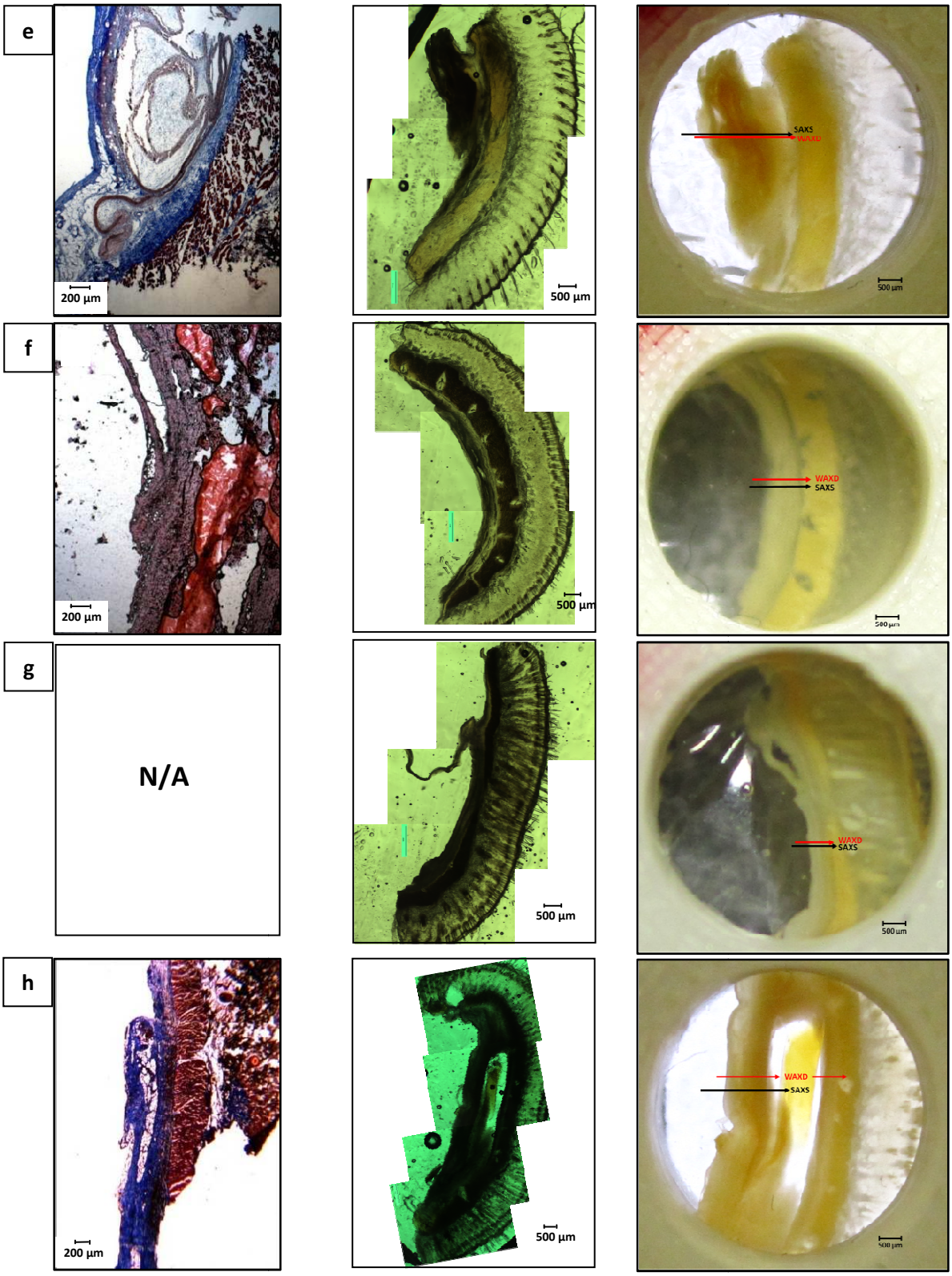
e
200 µm
500 µm
SAXS
WAXD
500 µm
f
200 µm
500 µm
WAXD
SAXS
g
N/A
500 µm
WAXD
SAXS
500 µm
h
200 µm
500 µm
WAXD
SAXS
500 µm

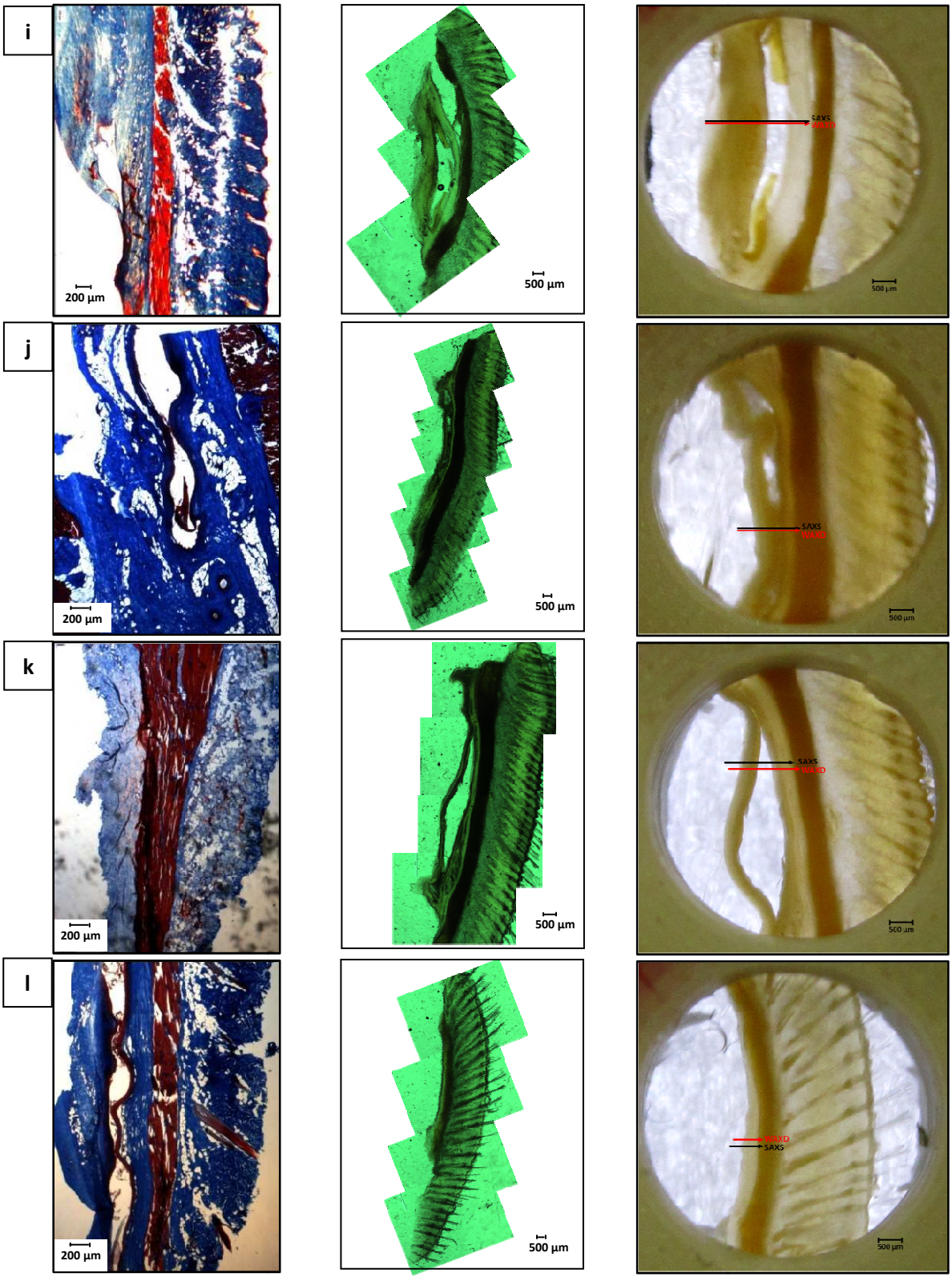
i
200 µm
500 µm
SAXS
WAXD
500 µm
j
200 µm
500 µm
SAXS
WAXD
500 µm
k
200 µm
500 µm
SAXS
WAXD
500 µm
l
200 µm
500 µm
WAXD
SAXS
500 µm

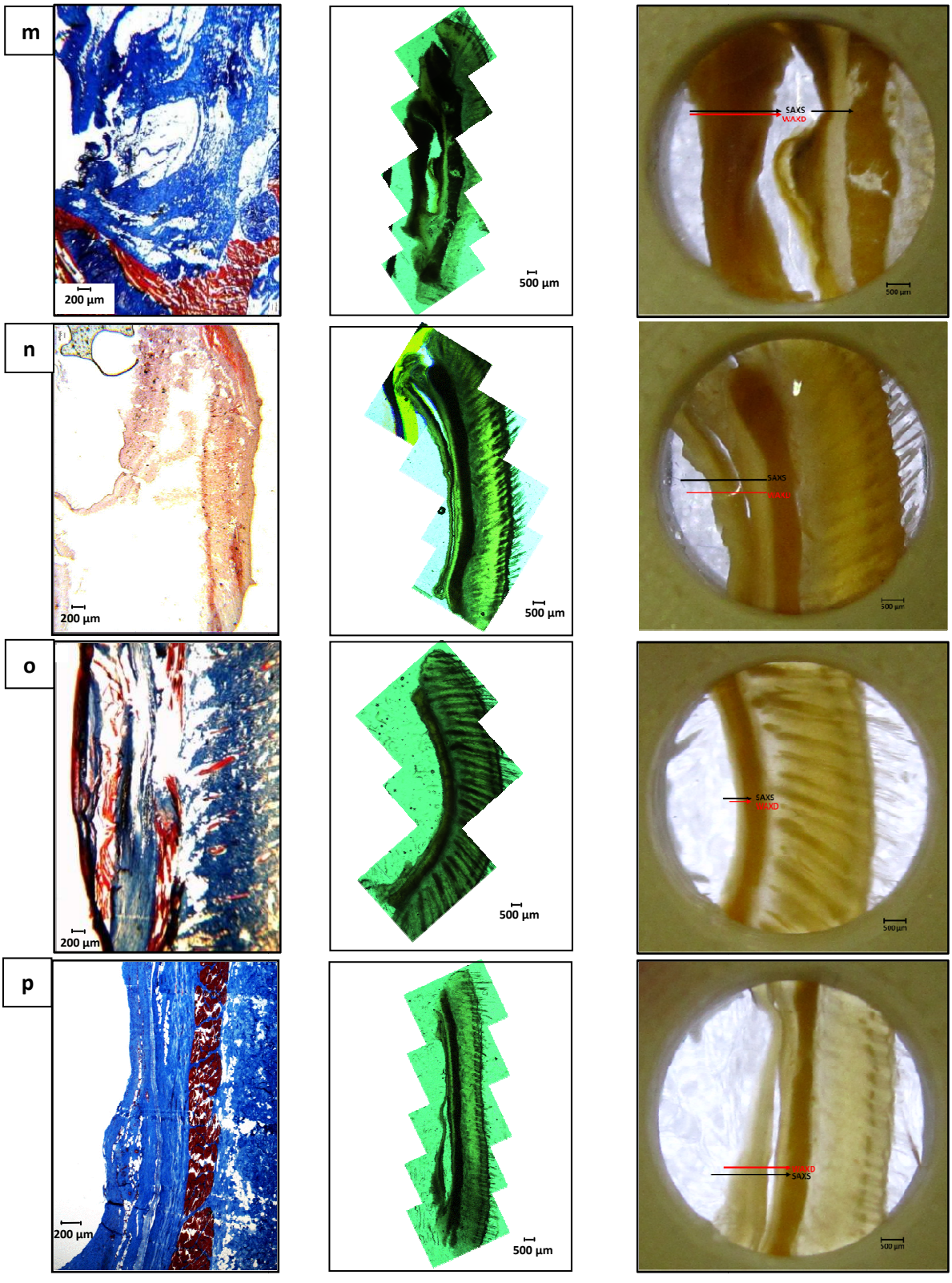
m
200 µm
500 µm
SAXS
WAXD
n
200 µm
500 µm
SAXS
WAXD
o
200 µm
500 µm
SAXS
WAXD
p
200 µm
500 µm
WAXD
SAXS

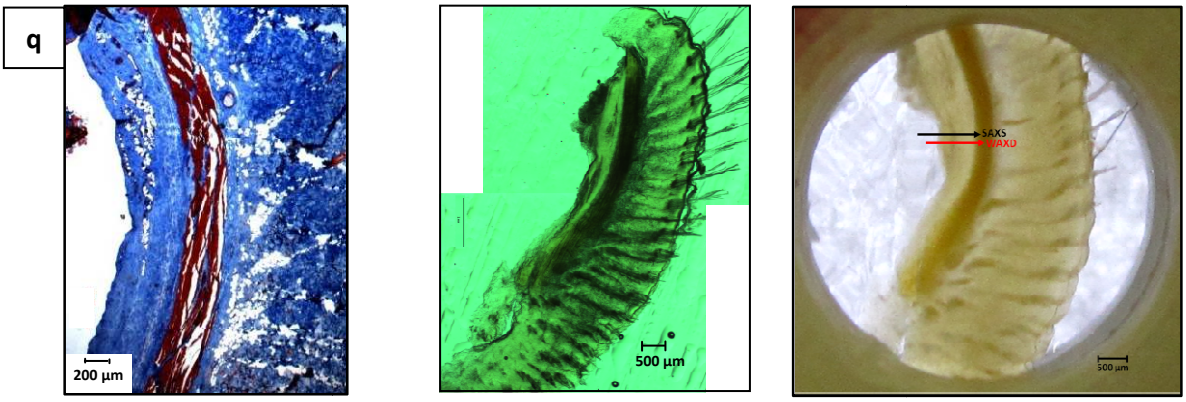

***Figure 5.2**: Images of (a) Sample R1b, (b) Sample R1d, (c) Sample R1f, (d) Sample 2b, (e) Sample 2d, (f) Sample 2e, (g) Sample 2f, (h) Sample 3e, (i) Sample 4c, (j) Sample 4e, (k) Sample 5b, (l) Sample 5c, (m) Sample 5d, (n) Sample 5e, (o) Sample 6b, (p) Sample 6c and (q) Sample R6f using (from left- right) optical microscopy post Masson's trichrome and Hematoxylin and eosin staining (images provided by Dr Krishna Burugapalli), optical microscope images of samples prior to mounting and camera images of samples mounted in sample holders with SAXS and WAXD locations indicated.*

5.2 SAXS Line Scan

Intensity maxima due to scattering of well ordered systems are observed as 'rings' about the centre of the image. Radially averaging the 2-dimensional SAXS patterns results in a 1-dimensional intensity profile over the entire image. Radial averaging is done by first defining a circular region of interest centred on the diffraction image and then applying this to the 2D images. The intensities are averaged as a function of *q,* the distance from the diffraction centre, starting from the pre-defined inner radius outward to the outer radius.

2-dimensional SAXS patterns gained from Sample R6c were analyzed using the *FIT2D* program. A total of 120 frames were collected in the line scan which spanned across water, fibrotic tissue and natural loose connective tissue (see **Figure 5.5** (d)). The 2D SAXS pattern of fibrotic tissue is shown in **Figure 5.3** (a) and (b). By radially averaging the 2D SAXS patterns using the inner and outer radius indicated in yellow in **Figure 5.3** (b), a 1D SAXS profile was generated. The resulting

1D data was exported to a standard plotting package (SigmaPlot, Version 10.0, Systat Software Inc., Germany) where the data was plotted as *Intensity* versus *q* (see **Figure 5.3** (c)).

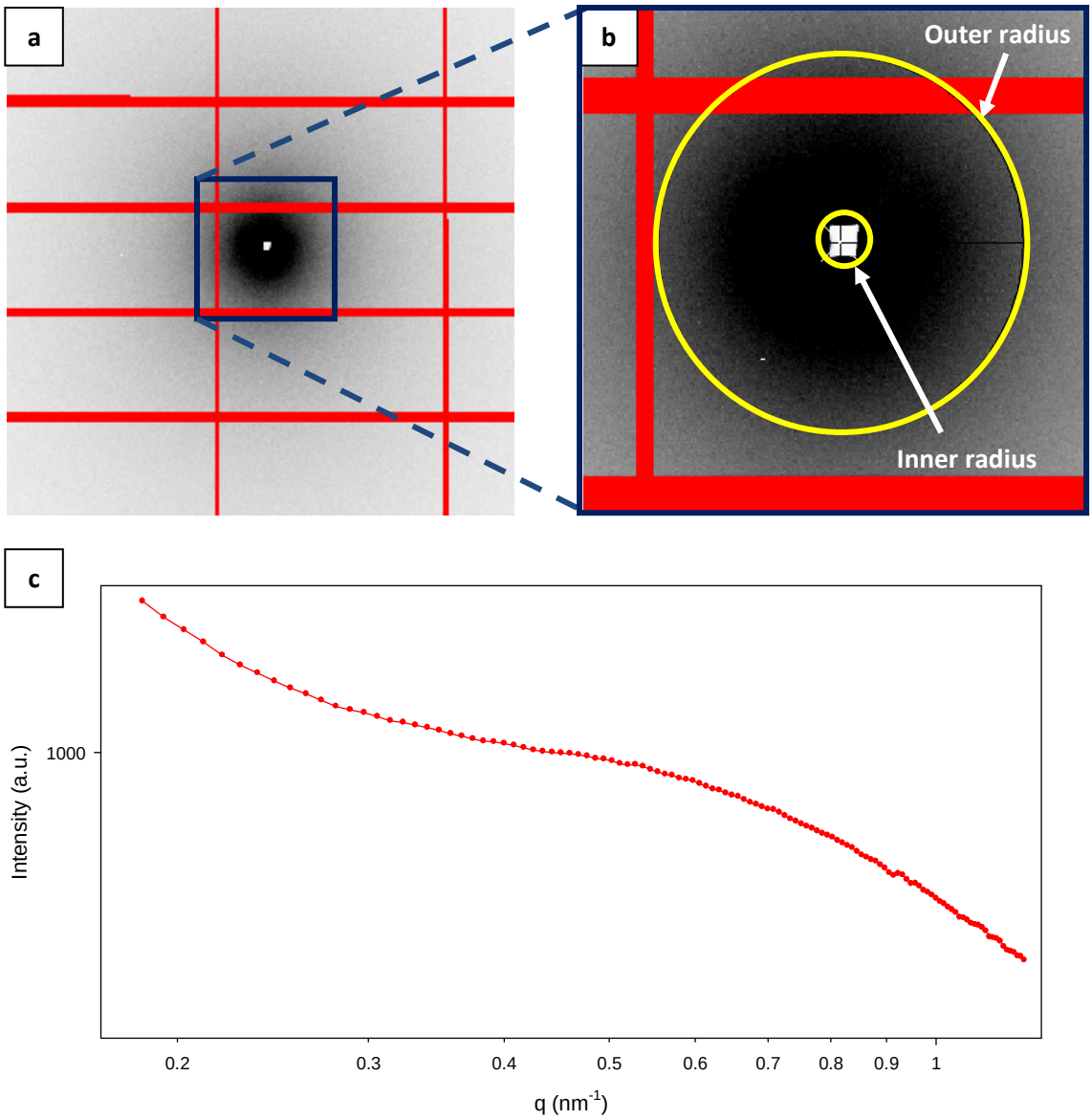

Figure 5.3: *SAXS results of Sample R6c showing (a) 2D SAXS pattern of fibrotic tissue region, (b) region of interest with inner and outer radius indicated, and (c) 1D SAXS profile of fibrotic tissue raw data with radial integration which provides total scattering intensity.*

In comparison to more conventional and strongly scattering samples (with higher electron density) like bone or cellulose, SAXS intensity from the porous and thin fibrotic tissue is relatively weak. Therefore, it is critical to carefully correct the measured SAXS signal to remove any extraneous signal (which can come from upstream beamline optics, air-scattering or other contributions) which will otherwise overwhelm the signal of interest from the tissue itself. In

order to correct for the scattering from air, water and other non-sample contributions to the X-ray signal, the raw SAXS data was background corrected. The background correction was carried out by measuring the raw SAXS data for a location in the sample without tissue (sometimes referred to as the "empty beam" position), and subtracting it from the raw SAXS data at the tissue-location for each frame using the following equation:

$$I_s^{bgr\ corr}(q) = I_s^{raw}(q) - \left[\frac{d_s}{d_w}\right] \cdot I_w^{raw}(q)$$

where $I_s^{bgr\,corr}(q)$ is the sample intensity after background correction, $I_s^{raw}(q)$ is the sample raw data intensity, d_s is the sample diode value, d_w is the empty-beam diode value and $I_w^{raw}(q)$ is the empty-beam background intensity averaged over 10 frames. Diode intensities were measured using a photon sensitive diode placed between the sample and detector. d_s/d_w correspond to transmission τ.

2D SAXS patterns of fibrotic tissue and empty-beam background are shown in **Figure 5.4** (a) and (b), respectively. The significant effect of background correction on the fibrotic tissue spectra is illustrated in **Figure 5.4** (c), where it is clear that (i) the corrected SAXS intensity is 2-3 orders of magnitude lower than the raw data and (ii) that after background correction the corrected SAXS intensity follows a power law behaviour $q^{-\alpha}$. In **Figure 5.5** (a), the 1D raw-SAXS intensity plots of water background, fibrotic tissue and transition tissue between implant and fibrotic tissue are shown. The equivalent background corrected plots are shown in **Figure 5.5** (b). It is apparent that fibrotic tissue and transition tissue have significantly different 1D SAXS profiles and a clear transition can be seen from water to transition subcutaneous tissue and to fibrotic tissue.

The area under the SAXS curve, A_{SAXS} (**Figure 5.5** (c)) for all 120 background corrected frames in the SAXS line scan (**Figure 5.5** (d)) was calculated. The area under the curve for the regions with no tissue (water region) was approximately zero and a larger area under the curve was seen

where fibrotic tissue is present. In this sample, the implant was no longer in place leaving an air-gap at the implant location. The dip in A_{SAXS} at positions between 1.48 mm and 1.6 mm on this sample corresponds precisely to the location where the implant used to be and is now a gap filled with the surrounding PBS solution. The removal of the implant can be attributed to two possible reasons. The first is the implant being removed during processing and sample preparation, and the second being the possible loosening of the implant at 9 weeks from surrounding tissue due to loss of adhesion. Most significantly, the high value of A_{SAXS} at both sides of the dip is noted, which is identified with the presence of a relatively-dense fibrotic tissue layer. Since fibrotic tissue is generated surrounding an implant, the peak in A_{SAXS} seen on both sides of the dip corresponds to implant location. The area under the curve is similar at both left and right fibrotic tissue locations, indicating a similar growth process on the peri-dermal and endodermal sides.

The scattering volume of the sample can be interpreted by comparing the area under SAXS curve with the diode intensity at each point along the line scan (see **Figure 5.6**). The diode intensity was measured by using a photon sensitive diode placed between the sample and detector. The measurement line scan was done 15 µm above the SAXS line scan to avoid measuring on an area subjected to radiation damage by the SAXS line scan. The data shows that there is higher x-ray absorbance by the sample as compared to water. It is not understood why the diode intensity did not rise at the location where the implant used to be and is now a gap filled with the surrounding PBS solution.

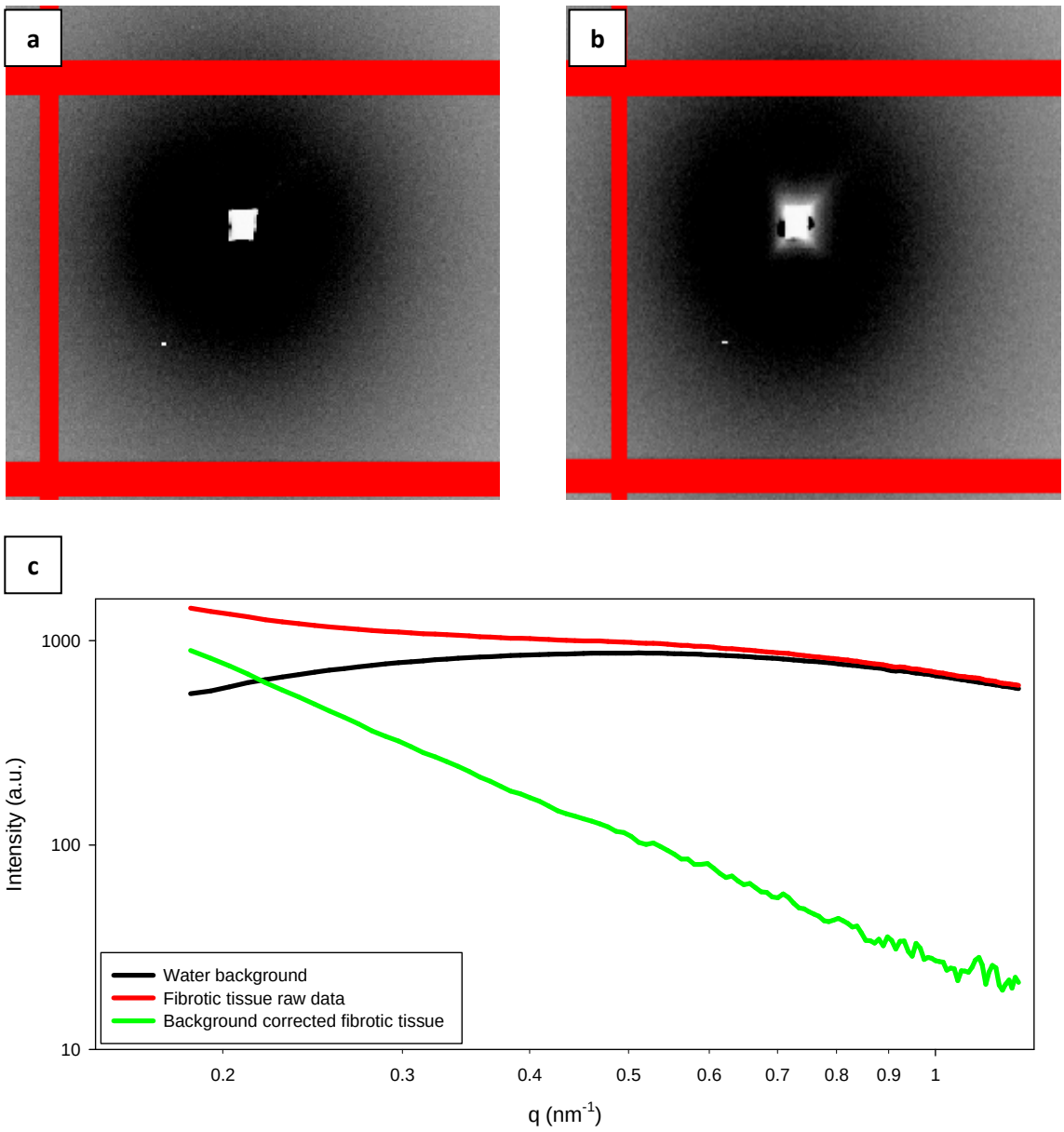

Figure 5.4: *Effect of background correction of SAXS results in Sample R6c showing (a) 2D SAXS pattern of fibrotic tissue region, (b) 2D SAXS pattern of water background, and (c) 1D SAXS profile with radial integration of water background, fibrotic tissue raw data and background corrected fibrotic tissue.*

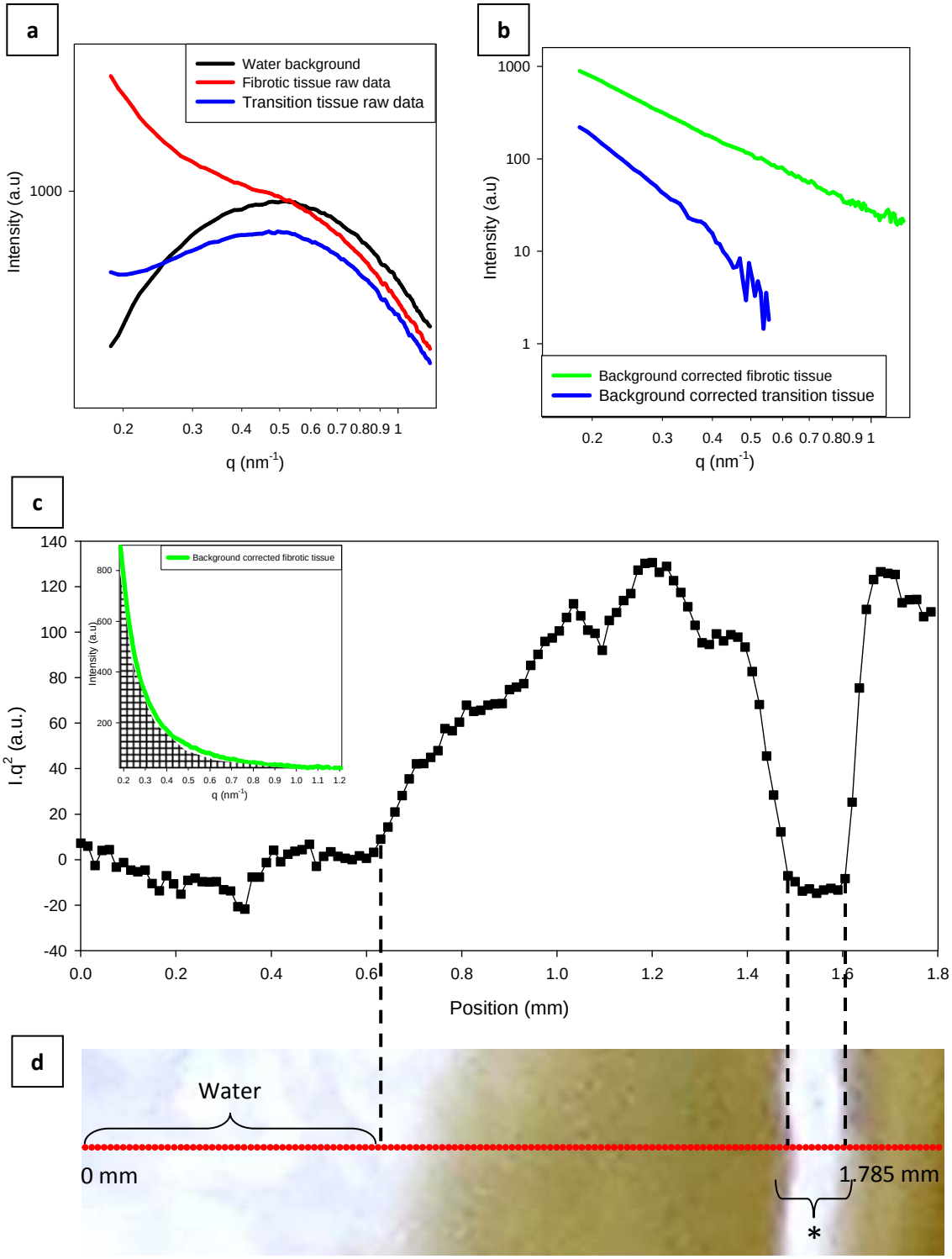

Figure 5.5: *Sample R6c (a) 1D SAXS intensity plots of water background, fibrotic tissue and transition tissue between implant and fibrotic tissue raw data, (b) 1D SAXS intensity plot of background corrected fibrotic tissue and transition tissue data, (c) area under the curve for SAXS line scan across water and fibrotic tissue region (area under the curve for fibrotic tissue shown inset as an example), and (d) SAXS line scan location with a beamsize of 15 µm (* denotes original implant location).*

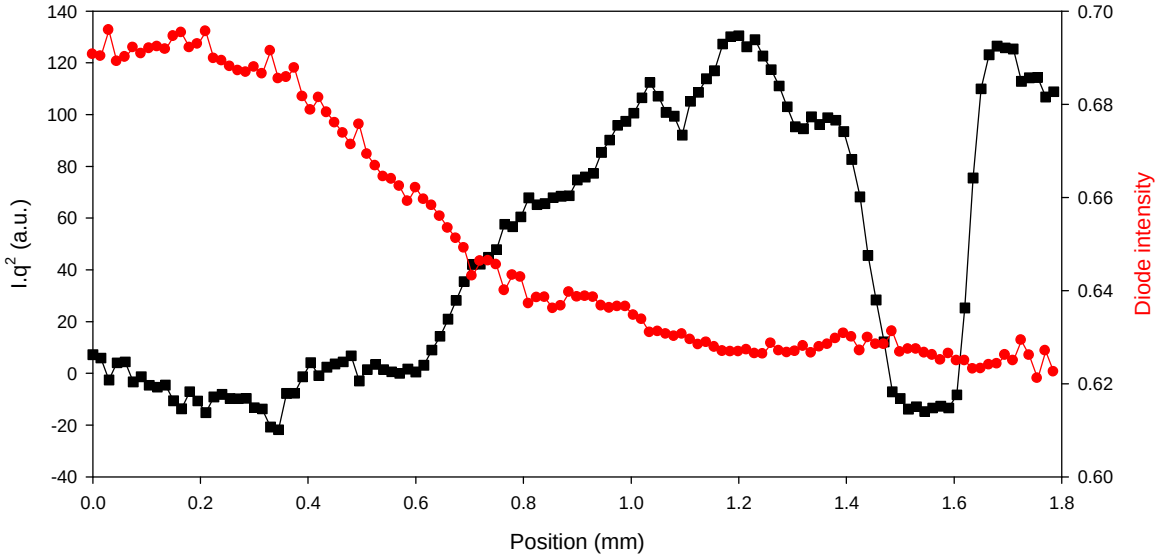

Figure 5.6: *Sample R6c area under SAXS curve and the diode intensities at each point along the line scan.*

The orientation of collagen fibrils can be estimated by azimuthally integrating the 2D SAXS spectra. The 2D SAXS patterns of rat tail tendon and Sample R6c fibrotic tissue region are shown in **Figure 5.7** (a) and (b), respectively. The 1D SAXS profiles of azimuthally integrated rat tail tendon and fibrotic tissue raw data and background corrected data are show in **Figure 5.7** (c) and (d), respectively. The primary orientation of collagen can be derived from the anisotropical SAXS pattern. If a large number of fibrils are randomly oriented, then this anisotropy vanishes and the 2D SAXS pattern becomes isotropic. To calculate the degree of alignment, the parameter ρ is introduced and is defined as follows:

$$\rho = \frac{A_1}{A_0 + A_1}$$

where A_0 is the constant background and A_1 is the total area under the curve minus the constant background (shown in **Figure 5.8** (a)). The parameter ρ gives the amount of oriented collagen fibrils, wherein a value of $\rho = 0$ indicates that there is no predominant orientation and $\rho = 1$ point towards perfectly oriented fibrils. Calculating ρ for both rat tail tendon and fibrotic tissue return the values of 1 and 0.239, respectively, indicating that collagen fibrils in rat tail tendon are

perfectly oriented while collagen fibrils in fibrotic tissue are somewhat anisotropic. This finding is somewhat unexpected, given the optical appearance of isotropy in the raw SAXS data in **Figure 5.4**. It highlights the necessity for careful background subtraction and analysis to accurately determine the nanostructural orientation of the fibrotic tissue.

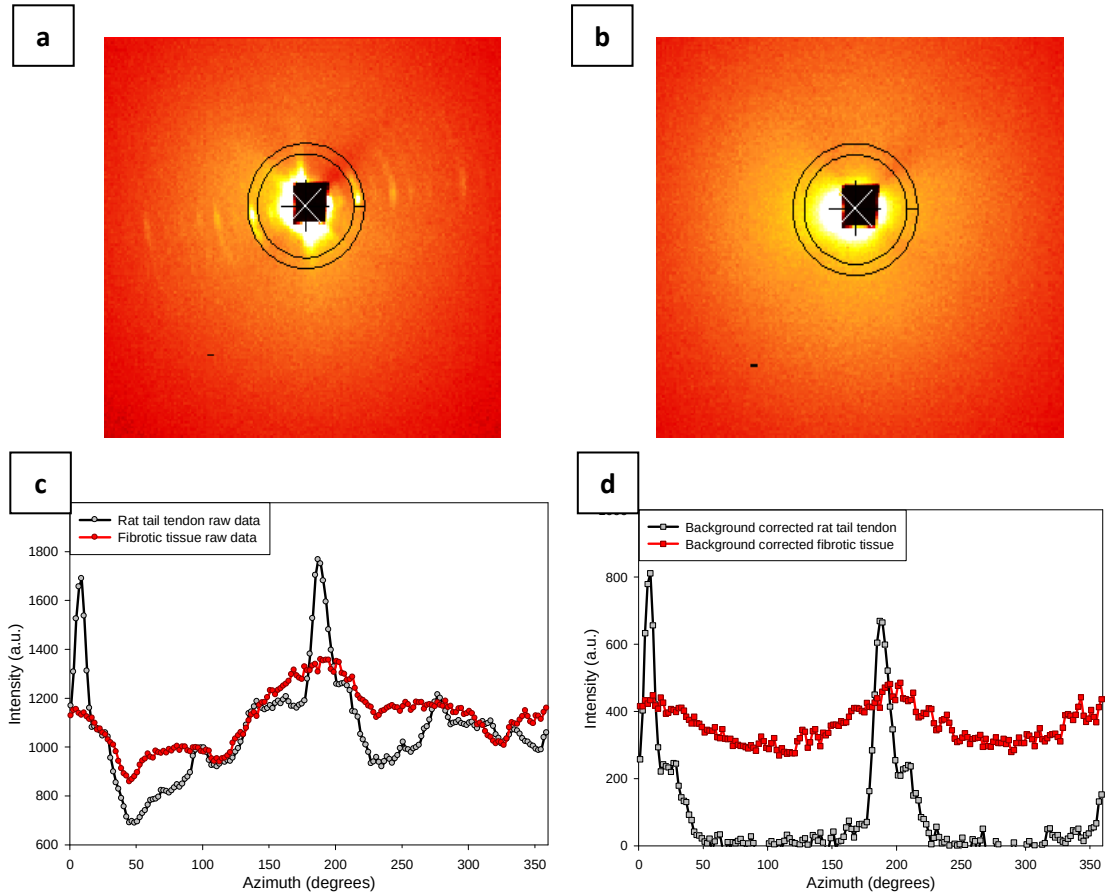

Figure 5.7: *2D SAXS patterns showing inner and outer radius locations of (a) rat tail tendon and (b) fibrotic tissue in Sample R6c, (c) 1D SAXS profiles showing azimuthally averaged scattering intensity of raw data and (d) 1D SAXS profile post background subtraction of rat tail tendon and fibrotic tissue.*

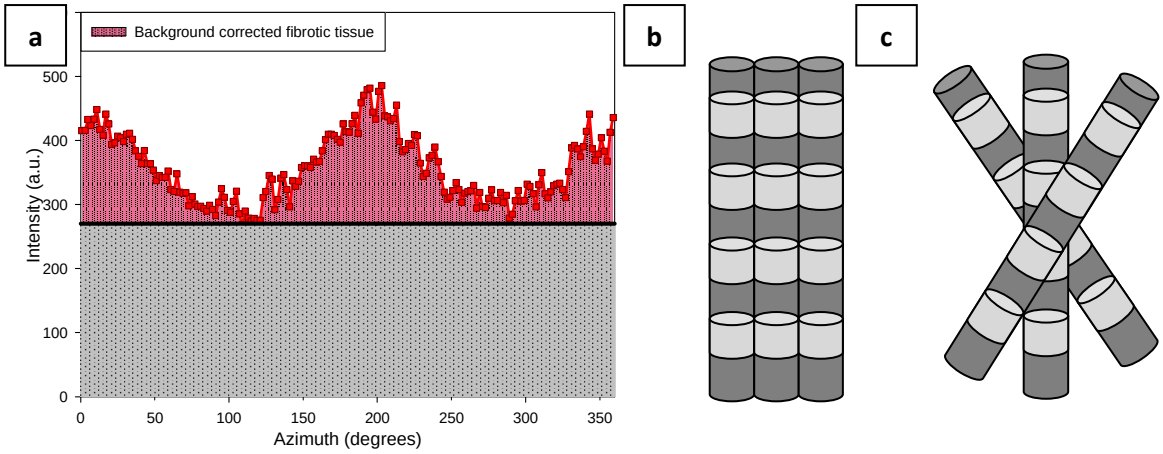

Figure 5.8: *(a) Sample R6c fibrotic tissue post background correction plot. The calculation of ρ requires A_1 and A_0 which are colour coded in the plot: A_1 in pink and the constant background A_0 in gray. Possible collagen fibril alignment in rat tail tendon and fibrotic tissue are shown in (b) and (c), respectively.*

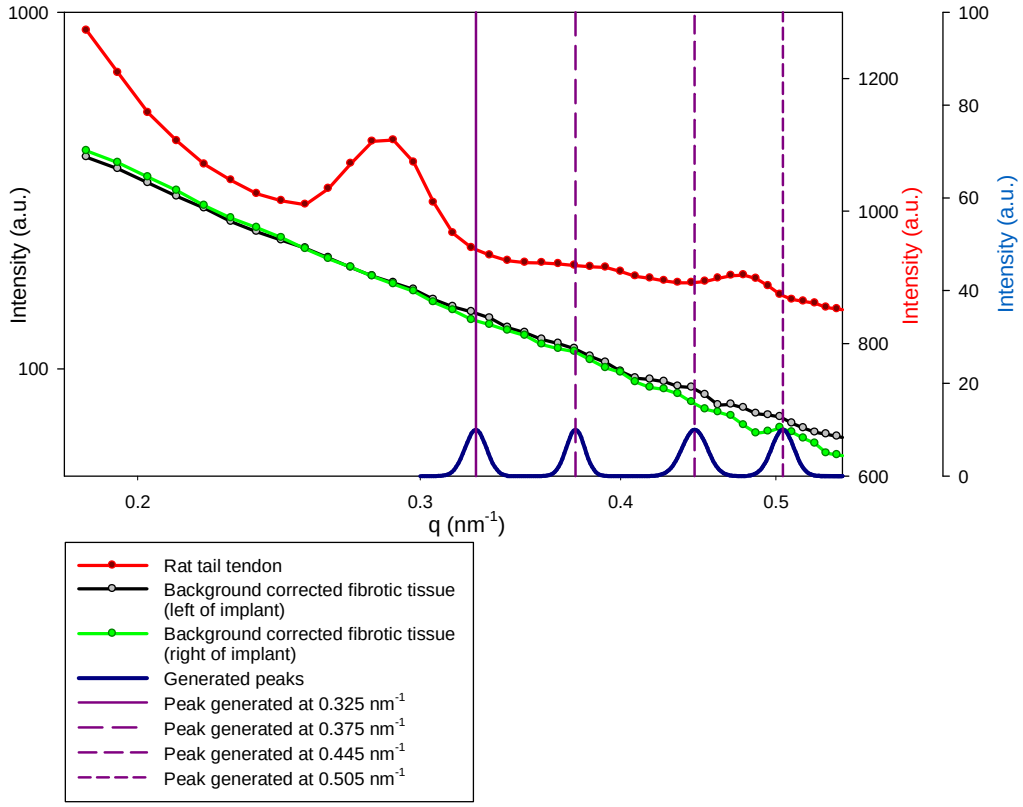

Figure 5.9: *1D SAXS profiles of rat tail tendon and fibrotic tissue from both the left and right sides of the implant in Sample R1b. Fibrotic tissue plots were corrected for water background. Gaussian peaks were generated at locations where q peaks are visible in fibrotic tissue.*

The axial periodicity of collagen fibrils, also known as D-spacing which arise from a series of meriodional reflections is calculated from 2D SAXS patterns using the following equation:

$$D = \frac{2\pi}{q_{SAXS}}$$

where q_{SAXS} is the peak position of a 1D WAXD profile. As can be seen in **Figure 5.7** (a) and (b), the meridional reflection patterns of rat tail tendon are highly observable whereas the Bragg peaks of fibrotic tissue are very weak. The first order meridional pattern is not seen as it is covered by the beam-stop. In highly ordered systems like rat tail tendon, relatively sharp diffraction spots are seen. In tissues where an angular dispersion of a population of collagen fibres occurs, angular spreading in the meridional reflection arc is seen. In systems where the fibrils are completely randomly oriented, a uniform circle of isotropic diffracted intensity is observed [165]. In developing chick corneas, meridional reflections only appear at day 12 of development and continue to increase steadily in intensity up to day 19. The D-period decreases from day 12 to day 19. Since the meridional reflections arise as a result of the axial electron density of fibrillar collagen and do not depend upon its lateral arrangement, collagen deposition is only detected at day 12, possibly due to the amount of new collagen deposition in the secondary chick stroma reaching a threshold [163]. At present, it is unclear if a similar condition applies to the development of fibrotic tissue.

From the q_{SAXS} peaks in **Figure 5.9**, the D-periodicity of rat tail tendon was found to be 67 nm which is consistent with values found in literature [20-21, 38, 43, 124]. However, q_{SAXS} peaks in 4 week old fibrotic tissue 1D SAXS profiles on both the left and right sides of the implant in Sample R1b appear to be very faint. The loss of observed intensity in the fibrotic tissue meridional series could be due to the random axial displacements arising from Type I and Type III collagen interactions. Model building and X-ray fibre diagram simulation studies done by Cameron et al. [37] show that nonspecific or random interactions of Type I and Type III collagen in axial

displacements of about 6 nm within a fibril D-period could decrease the diffraction intensity. The localisation of Type I and Type III collagen molecules within the fibril is unclear and could contribute to the results obtained in this study.

Gaussian peaks were generated at points where q_{SAXS} peaks were observed in fibrotic tissue profiles in order to calculate the D-periodicity of fibrotic tissue. Unlike the 65.5 nm axial periodicity found in fibrotic tissue in the collagen-polyester composite implanted in sheep by Brodsky et al. [123], D-periodicity in Sample R1b could not be determined as of yet. It is of interest to speculate on the origins of the different collagen D-periodicity seen in fibrotic tissue in this study. Two key differences observed are the implant porosity and the maturity of the fibrotic tissue. Fibrotic tissue in this study was explanted after only 4 weeks whereas the collagen-polyester samples use by Brodsky et al. were explanted after 13 weeks. As highlighted by Brodsky et al. [123], fibrotic tissue that forms surrounding a biomaterial implant is normally disordered. The altered D-periodicity seen in this study could also be due to the presence of a significant amount of Type III collagen (owing to the short implantation time) which, although homologous to Type I, has different amino acid residues in about one-third of its sequence [43]. A shortened D-period in heterotypic collagen fibres may indicate a molecular tilt of 15° to the fibre axis [37]. Nevertheless, results of this SAXS analysis support the somewhat anisotropic collagen fibril orientation seen in **Figure 5.8** demonstrating that the collagen fibrils in fibrotic tissue are not well oriented.

5.3 WAXD Line Scan

A total of 101 frames were collected during WAXD line scan in Sample R6c which similar to SAXS line scan also spanned across water, fibrotic tissue and natural loose connective tissue (fibrous tissue). To ensure that the WAXD and SAXS data were as far as possible comparable to each other, the WAXD line scan was done 100 µm above the SAXS line scan. 2D WAXD patterns were also analyzed using *FIT2D*. **Figure 5.10** (a) and (b) illustrate the 2D WAXD patterns of fibrotic

tissue and rat tail tendon, respectively. Rat tail tendon was used to show the integration location used for fibrotic tissue. Both fibrotic tissue and rat tail tendon raw data 1D WAXD profiles are shown in **Figure 5.10** (c). While a large q_{WAXD} peak in seen in rat tail tendon, a much smaller peak is visible in the fibrotic tissue (indicated by black arrow in **Figure 5.10** (c)) consistent with our previous observation of the weakly scattering nature of this material. Indeed, the peak in fibrotic tissue, although at the q-value expected for the 0.29 nm tropocollagen amino-acid spacing, is only appearing as a bump or slight intensity elevation in the raw data. Therefore, in order to isolate the peak alone without the contribution from diffuse scattering leading to the intensity fall-off, a linear background subtraction was done on all frames. The effect of linear background subtraction is seen in **Figure 5.10** (d). A clear *q* peak is now visible for the fibrotic tissue plot.

Similar to SAXS analysis, area under the curve, A_{WAXD} (**Figure 5.11** (a)) of all 101 linear background-subtracted frames in the WAXD line scan location (**Figure 5.11** (b)) was calculated. A_{WAXD} of water region was approximately zero, while a larger area under the curve was seen at the locations where fibrotic tissue is expected to be. Similar to A_{SAXS}, A_{WAXD} dips again to zero at the location where the implant used to be, at positions between 1.5 mm and 1.64 mm and rises again corresponding to fibrotic tissue region on the right of the implant.

Intramolecular spacing, d_m which corresponds to the spacing of amino acid residues along the tropocollagen chain can be calculated using the following equation:

$$d_m = \frac{2\pi}{q_{WAXD}}$$

where q_{WAXD} is the peak position of a 1D WAXD profile (illustrated **Figure 5.10** (c)). Peak q_{WAXD} position for rat tail tendon was found to be 21.46 nm^{-1}, corresponding (as expected) to the intra-tropocollagen amino-acid residue spacing of $2\pi/21.46$ nm^{-1} ~ 0.29 nm. This is in agreement with the intramolecular spacing seen in dermis and whole human skin [122] as well as that of collagen

[166]. In Sample R6c, mean peak positions of q_{WAXD} were calculated on both the left and right sides of the implant location. Peak q_{WAXD} positions were found to be slightly higher than that of rat tail tendon with a mean value of 21.59 ± 0.09 nm^{-1} and 21.55 ± 0.14 nm^{-1} on the left and right sides of the implant, respectively. Calculations of the intra-tropocollagen amino-acid residue spacing of fibrotic tissue in Sample R6c using the above equation also returned mean values of 0.29 nm with negligible standard deviation values on both the left and right sides of the implant. Peak q_{WAXD} positions and the corresponding intramolecular spacing, d_m in rat tail tendon and fibrotic tissue on left and right of implant in Sample R6c are summarized in **Table 5.1**. Linear background subtracted curves of rat tail tendon and a fibrotic tissue plot are illustrated in **Figure 5.12** (b). The mean peak positions of *q* are shown in **Figure 5.12** (b).

Sample R6c SAXS and WAXD area under the curve comparison plots (see **Figure 5.13** (a)) show that both SAXS and WAXD can be consistently used to identify the fibrotic tissue location. SAXS and WAXD line scan locations are shown in **Figure 5.13** (c). Peaks in SAXS and WAXD area under the curve at positions of 1.2 mm and 1.7 mm correspond to presence of collagen while regions absent of tissue are indicated by area under the curve of zero. The gradual increase in area under the curve at the tissue-implant interface seems to correspond to the presence of cell layers. The SAXS and WAXD correlation plot in **Figure 5.13** (b) shows a consistent rise in both SAXS and WAXD intensities followed by a plateau in SAXS intensity. As SAXS intensity measures the amount of nanoscale area (in this case corresponding to the area of the fibrils), a plateau in SAXS intensity indicates that no further fibrils are being formed. Conversely, the WAXD intensity measures the intrafibrillar degree of order or crystallinity. As the tropocollagen molecules within the fibrils may continue to become more and more ordered (possibly due to stabilizing processes such as collagen crosslinking) while the outer fibril area remains constant, it is fully consistent that an increase in WAXD intensity is accompanied by a relatively constant SAXS intensity as seen in **Figure 5.13** (a).

***Table 5.1**: Peak q_{WAXD} positions and the corresponding intramolecular spacing, d_m in rat tail tendon and fibrotic tissue on left and right of implant in Sample R6c.*

	q_{WAXD} (Mean ± SD nm^{-1})	d_m (Mean ± SD nm)
Rat tail tendon	21.46	0.29
FT left of implant	21.59 ± 0.09	0.29 ± 0.001
FT right of implant	21.55 ± 0.14	0.29 ± 0.002

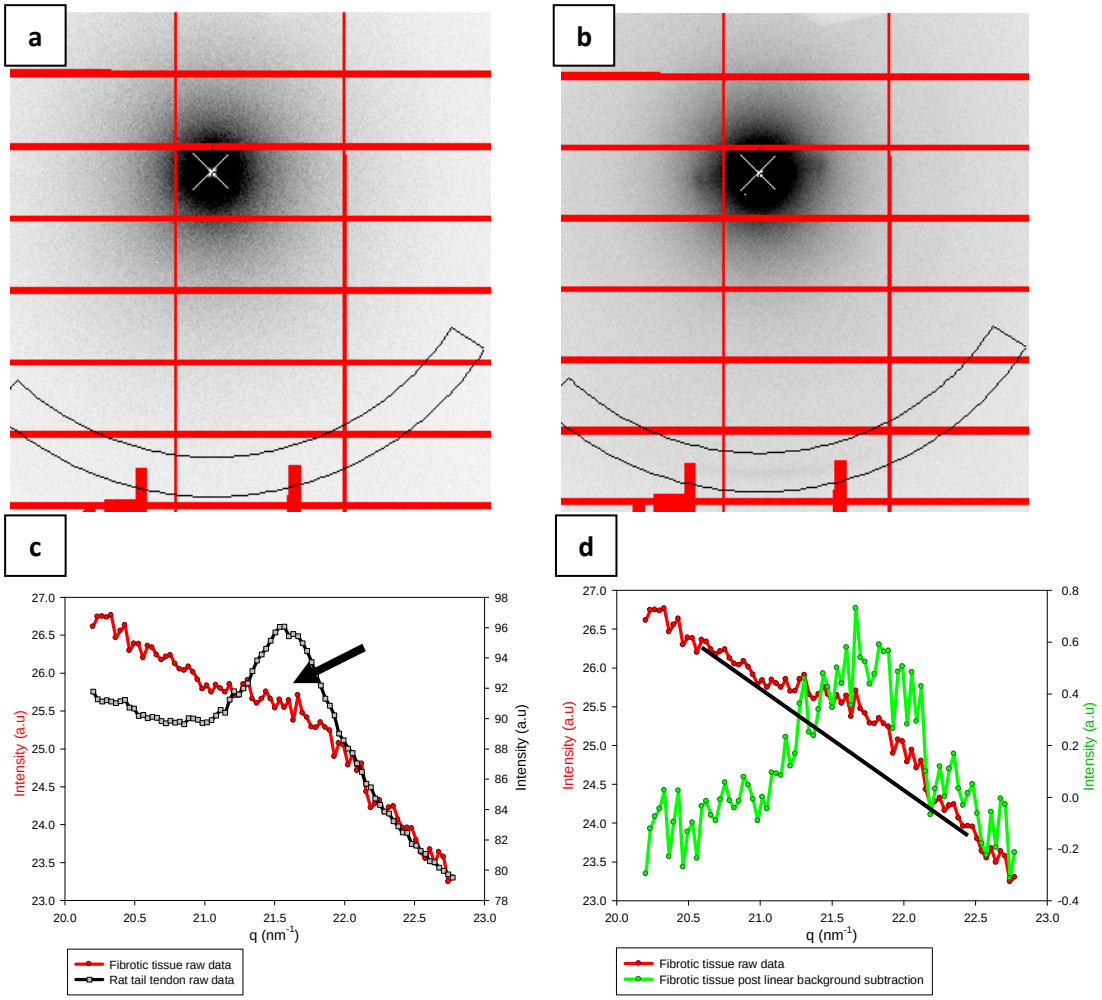

***Figure 5.10:** WAXD results of Sample R6c showing (a) 2D WAXD pattern of fibrotic tissue region, (b) 2D WAXD pattern of rat tail tendon and (c) 1D WAXD profile of rat tail tendon and fibrotic tissue raw data (arrow indicates fibrotic tissue q_{WAXD} peak), and (d) 1D WAXD profile of fibrotic tissue raw data and fibrotic tissue data post linear background subtraction (black solid line indicates linear background subtraction).*

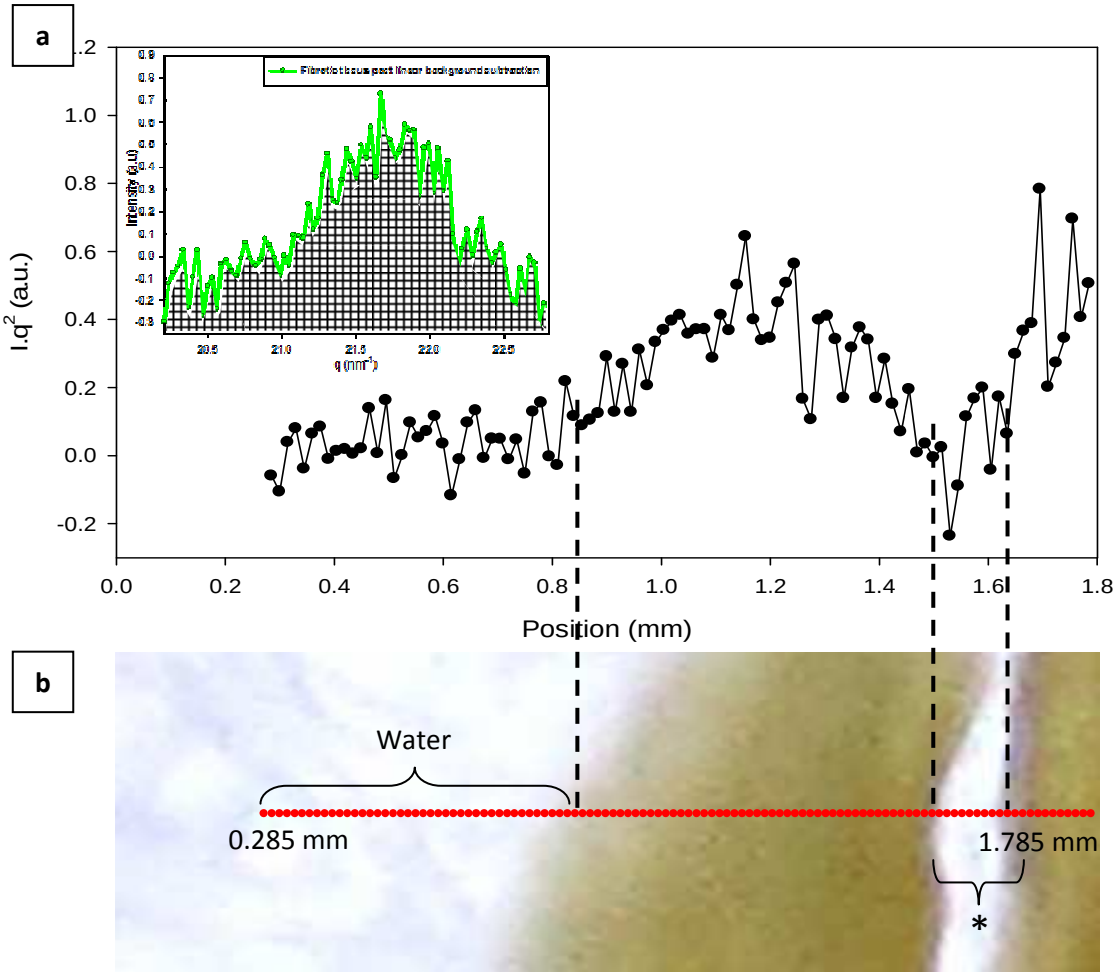

Figure 5.11: *WAXD results of Sample R6c showing (a) area under the curve for WAXD line scan across water and fibrotic tissue region (area under the curve for fibrotic tissue shown inset), and (d) WAXD line scan location with a beamsize of 15 µm (* denotes original implant location).*

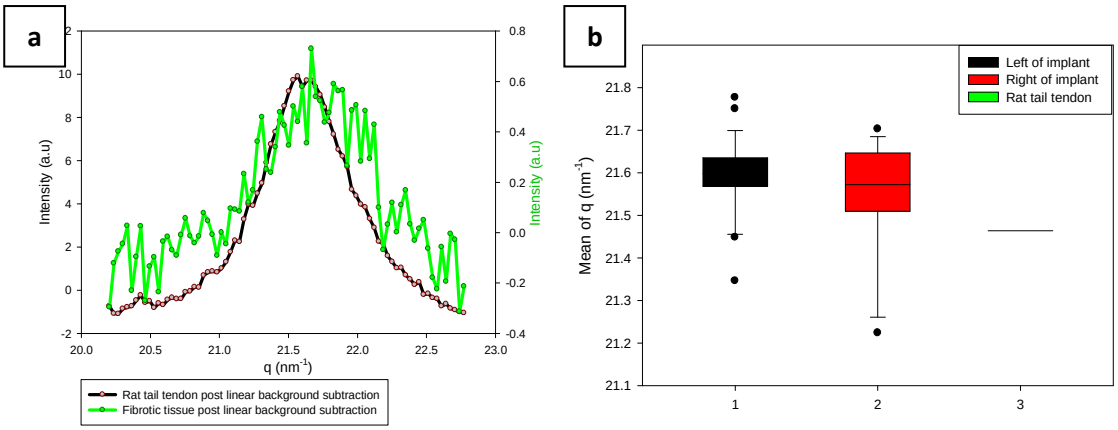

Figure 5.12: *(a) 1D WAXD intensity plots of fibrotic tissue and rat tail tendon post linear background subtraction, and (b) mean peak position of q on left and right of implant as compared to that of rat tail tendon (Error bars above and below the boxes indicate the 90th and 10th percentiles).*

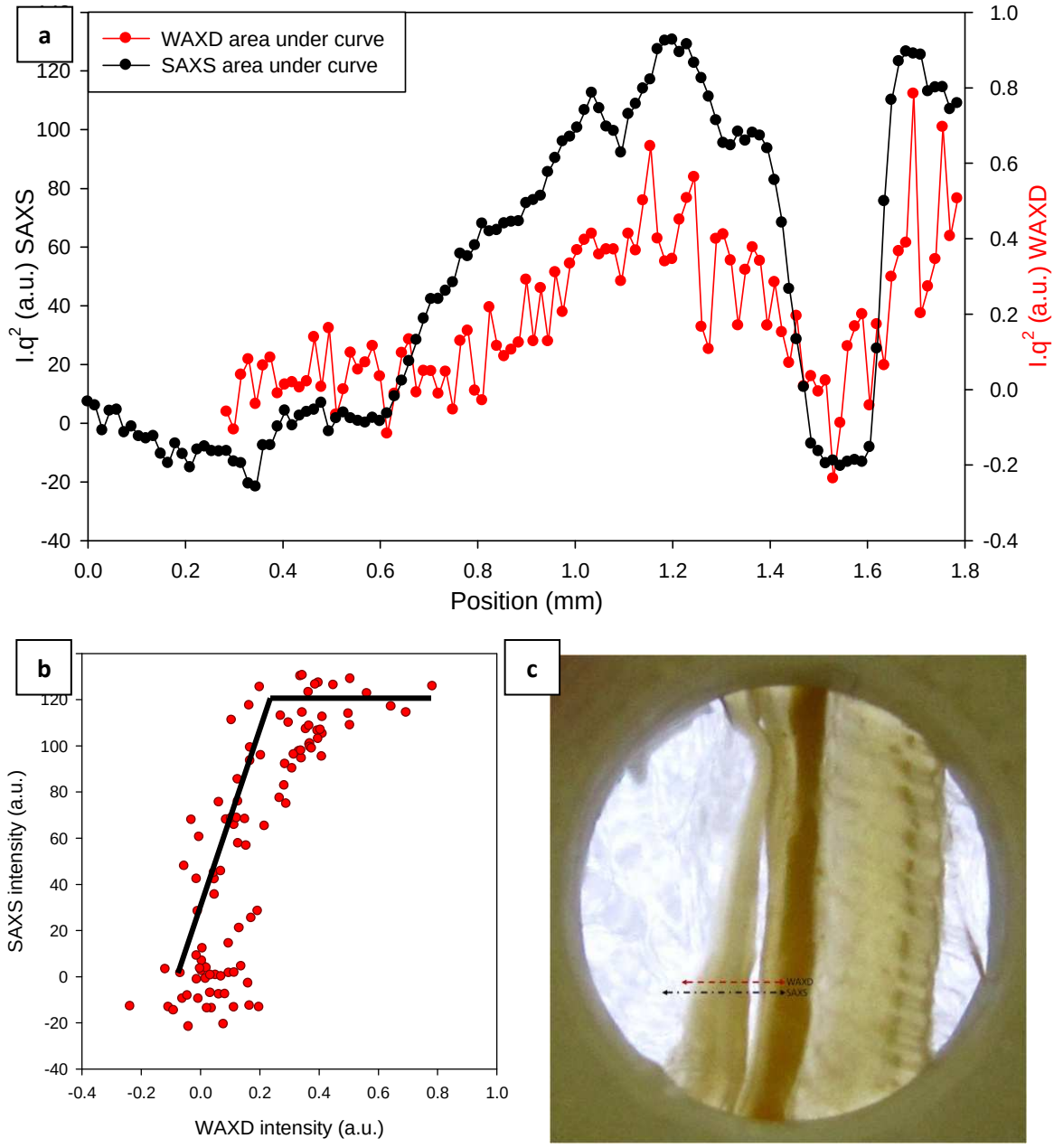

Figure 5.13: *Sample R6c SAXS and WAXD (a) area under curve comparison plot, (b) correlation plot and, (c) line scan locations on sample.*

5.4 Additional Sample Analysis

The SAXS and WAXD analysis discussed above were then applied on 3 other samples of the same implant type (implant type-D: electrospun polyurethane (12%) mesh with a fibre diameter of about 1200 nm); Sample R5e explanted at 9 weeks and Samples R1d and R2b explanted at 4 weeks.

Results of Sample R5e support the findings of Sample R6c. A total of 129 frames and 120 frames were collected in SAXS and WAXD line scans, respectively, spanning across water, fibrotic tissue and natural loose connective tissue (see **Figure 5.16** (b) and (d)). The 1D SAXS profile generated by radially averaging the 2D SAXS patterns is shown in **Figure 5.14** (a). Background correction was carried out to remove any extraneous signal and the resulting fibrotic tissue spectra is illustrated in **Figure 5.14** (b). In **Figure 5.15** (a), the 1D raw-SAXS intensity plots of water background, fibrotic tissue and transition tissue between implant and fibrotic tissue are shown. The equivalent background corrected plots are shown in **Figure 5.15** (b). As was seen in Sample R6c, the area under the SAXS and WAXD curves in Sample R5e shown in **Figure 5.16** (a) and (b), respectively, correspond well to the location of water and fibrotic tissue in **Figure 5.16** (c) and (d), respectively.

The scattering volume of the sample can be interpreted by comparing the area under SAXS curve with the diode intensity at each point along the line scan (see **Figure 5.17**). The diode intensity was measured by using a photon sensitive diode placed between the sample and detector. The measurement line scan was done 15 μm above the SAXS line scan to avoid measuring on an area subjected to radiation damage by the SAXS line scan. The data shows that there is higher x-ray absorbance by the sample as compared to water.

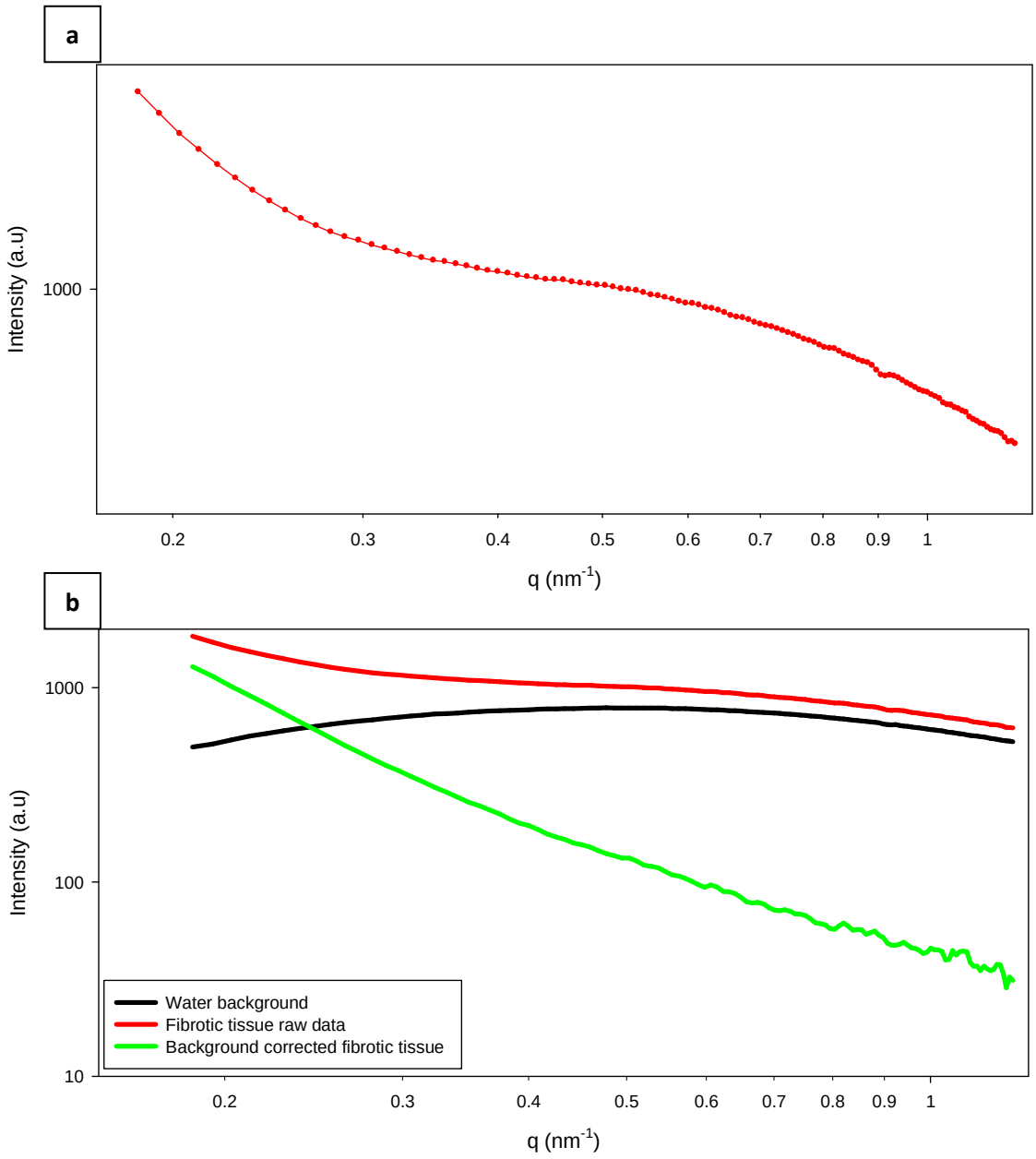

Figure 5.14: *SAXS results of Sample R5e showing (a) 1D SAXS profile of fibrotic tissue raw data with radial integration which provides total scattering intensity, and (b) 1D SAXS profile with radial integration of water background, fibrotic tissue raw data and background corrected fibrotic tissue.*

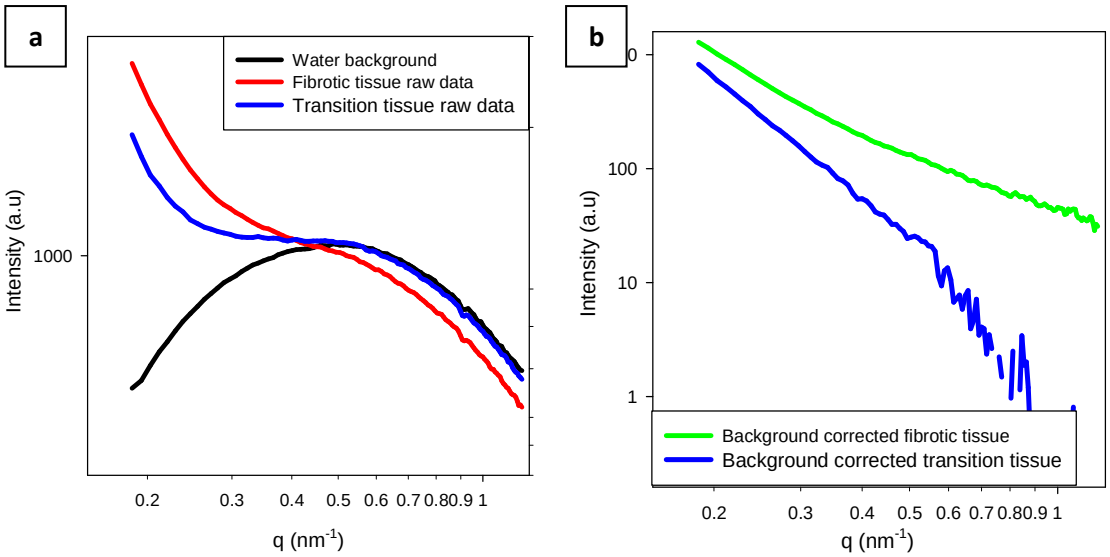

Figure 5.15: *Sample R5e (a) 1D SAXS intensity plots of water background, fibrotic tissue and transition tissue between implant and fibrotic tissue raw data, and (b) 1D SAXS intensity plot of background corrected fibrotic tissue and transition tissue data.*

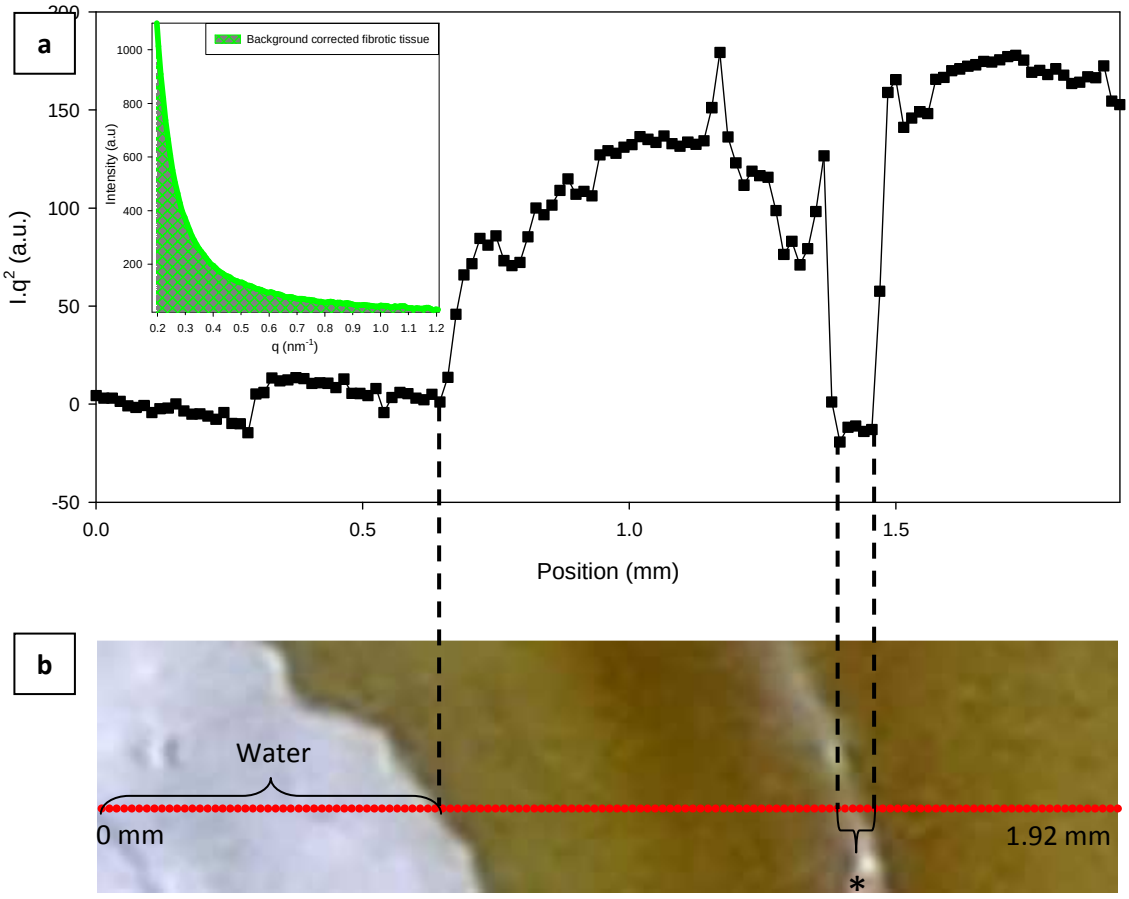

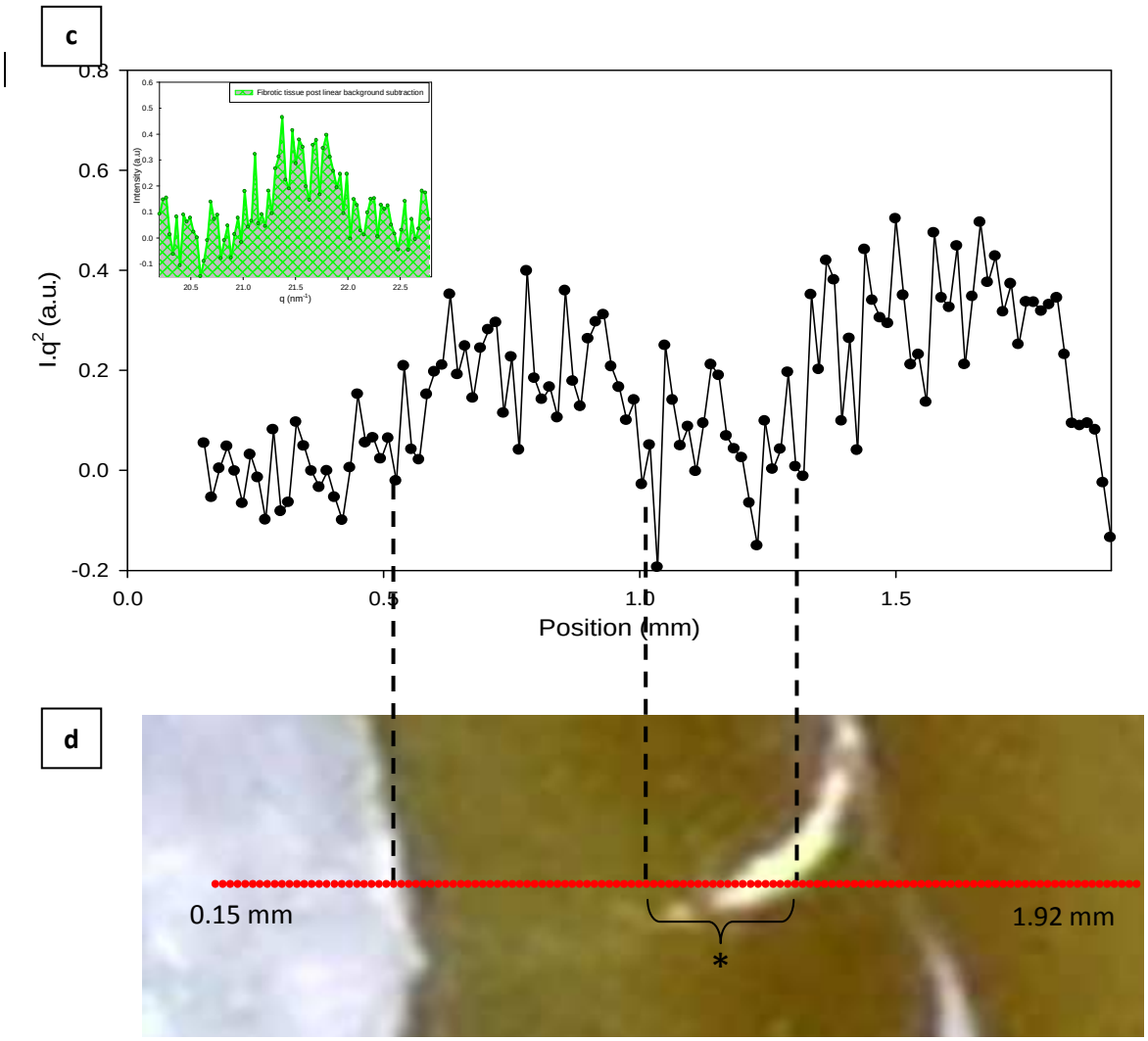

Figure 5.16: *Sample R5e area under the curve across water and fibrotic tissue region (area under the curve for fibrotic tissue shown inset as an example) (a) SAXS line scan and (c) WAXD line scan, and corresponding SAXS (b) and WAXD (d) line scan locations with a beamsize of 15 µm on actual sample (* denotes original implant location).*

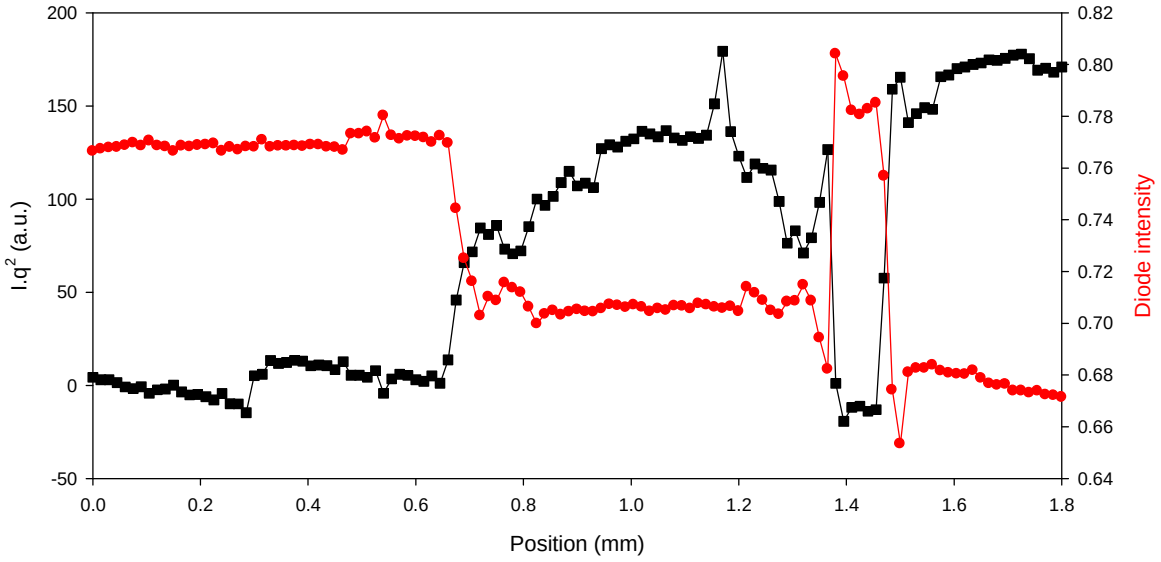

Figure 5.17: *Sample R5e area under SAXS curve and the diode intensities at each point along the line scan.*

Azimuthal integration of 2D SAXS spectra to determine the orientation of collagen fibrils in the fibrotic tissue of Sample R5e results in the 1D SAXS profile seen in **Figure 5.18**. To evaluate the fibril orientation of Sample R5e, the parameter ρ described earlier was calculated. ρ returned a value of 0.848 which indicates that fibrotic tissue is still somewhat anisotropic as seen in Sample R6c.

Analysis of Sample R5e fibrotic tissue 2D WAXD spectra resulted in the 1D profile shown in **Figure 5.19**. Consistent with the findings of Sample R6c WAXD data, a small q_{WAXD} peak is visible in fibrotic tissue (**Figure 5.19** (a)). A clear q peak is visible post linear background subtraction, as seen in **Figure 5.19** (b) and (c). Peak q_{WAXD} positions on the left and right sides of the implant were found to be 21.64 ± 0.88 nm^{-1} and 21.74 ± 0.42 nm^{-1}, respectively. The mean peak positions of q are illustrated in **Figure 5.19** (d). Calculation of the intramolecular spacing, d_m, returned values of 0.29 nm with negligible standard deviation values on both the left and right sides of the implant.

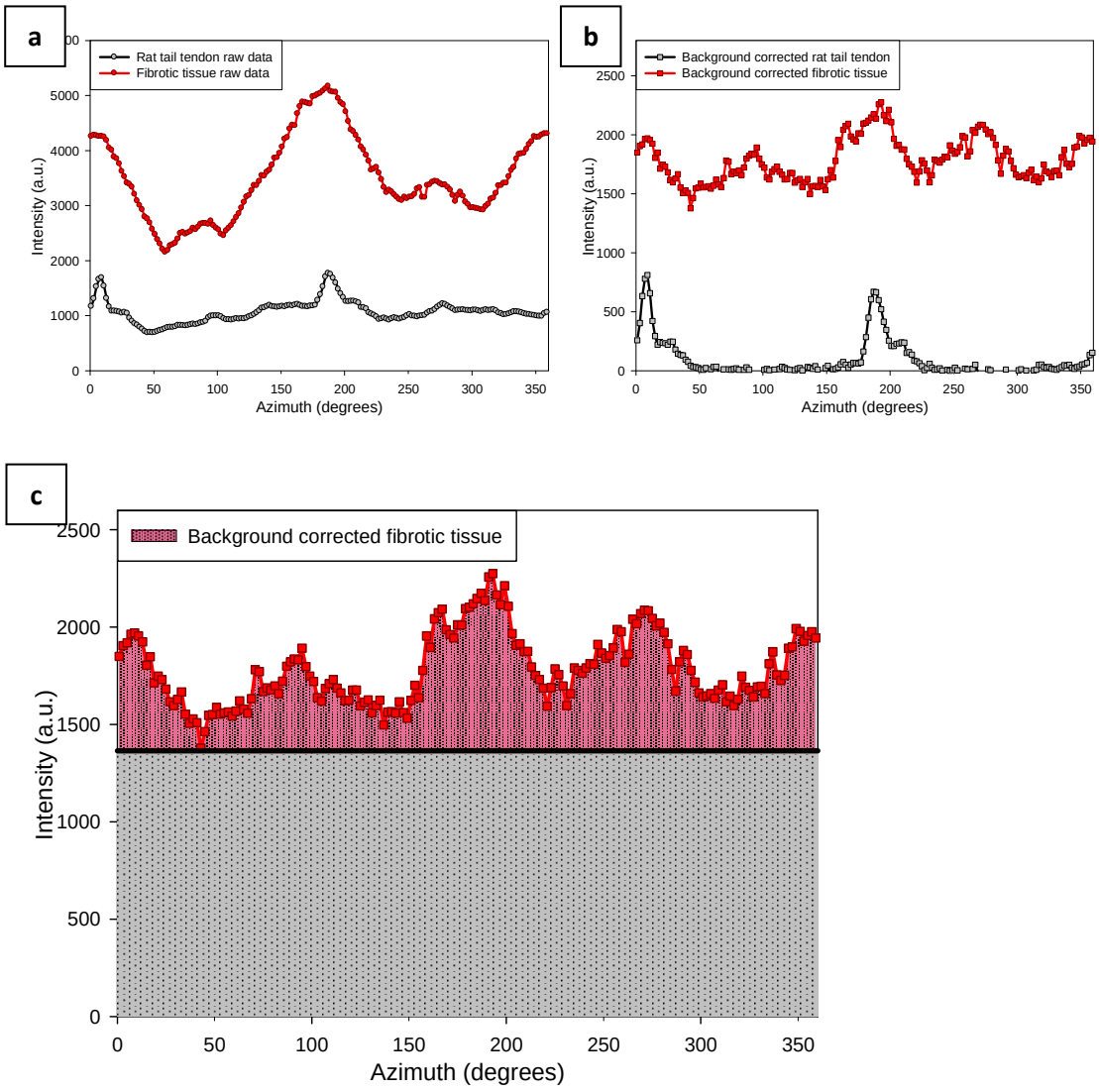

Figure 5.18: *Sample R5e (a) 1D SAXS profiles showing azimuthally averaged scattering intensity of rat tail tendon and fibrotic tissue raw data, (b) 1D SAXS profile post background subtraction of rat tail tendon and fibrotic tissue, and (c) fibrotic tissue post background correction plot.*

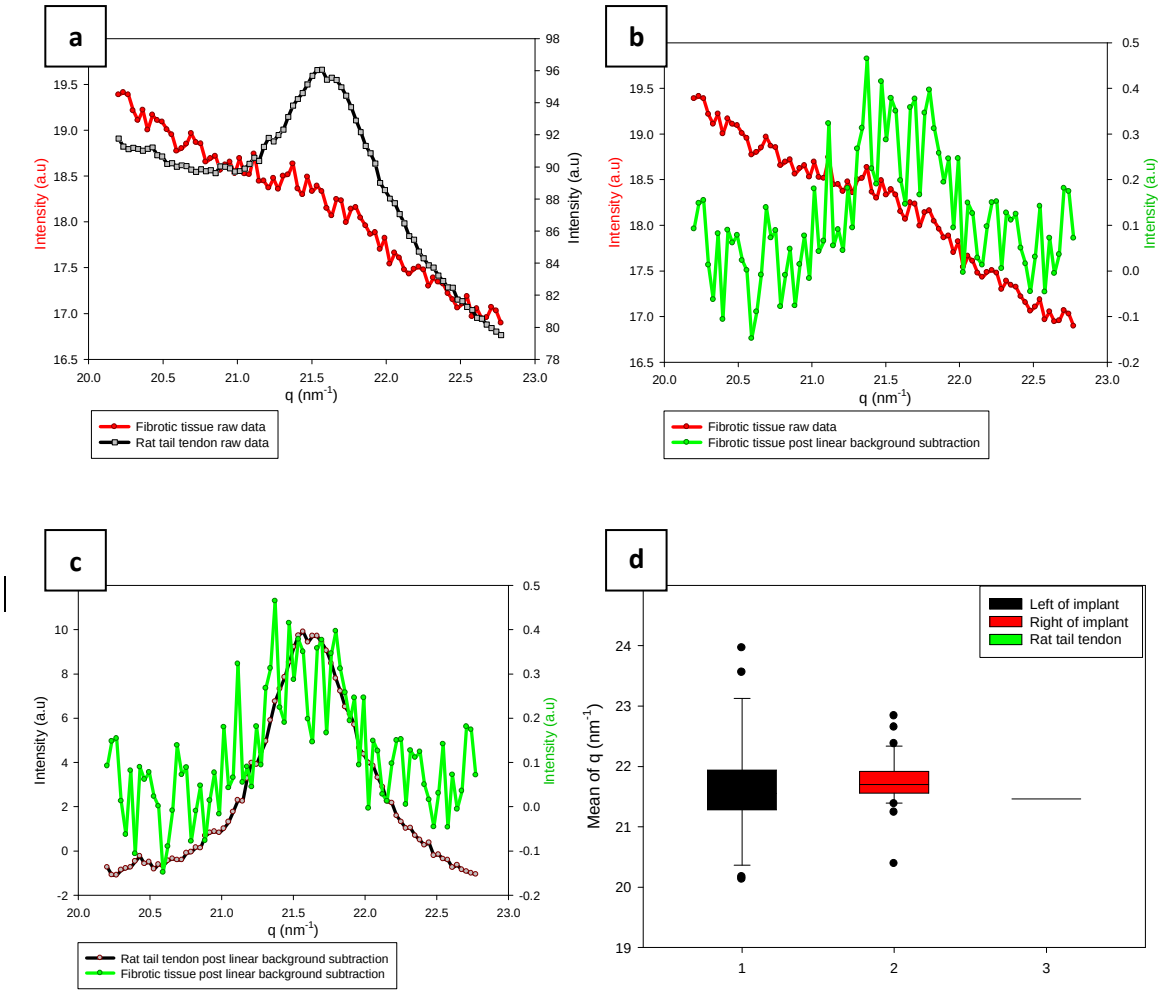

Figure 5.19: *WAXD results of Sample R5e showing (a) 1D WAXD profile of rat tail tendon and fibrotic tissue raw data, (b) 1D WAXD profile of fibrotic tissue raw data and fibrotic tissue data post linear background subtraction (black solid line indicates linear background subtraction), (c) 1D WAXD intensity plots of fibrotic tissue and rat tail tendon post linear background subtraction, and (d) mean peak position of q on left and right of implant as compared to that of rat tail tendon (Error bars above and below the boxes indicate the 90th and 10th percentiles).*

Samples R1d and R2b were explanted at 4 weeks. In both samples the implant was still intact post processing, as seen in **Figure 5.20**. While the implant is visible in optical microscope images post Masson's trichrome staining (**Figure 5.20** (a) and (b)), the implant is not distinguishable from surrounding tissue in optical microscope images of actual samples mounted for testing (**Figure 5.20** (c) and (d)).

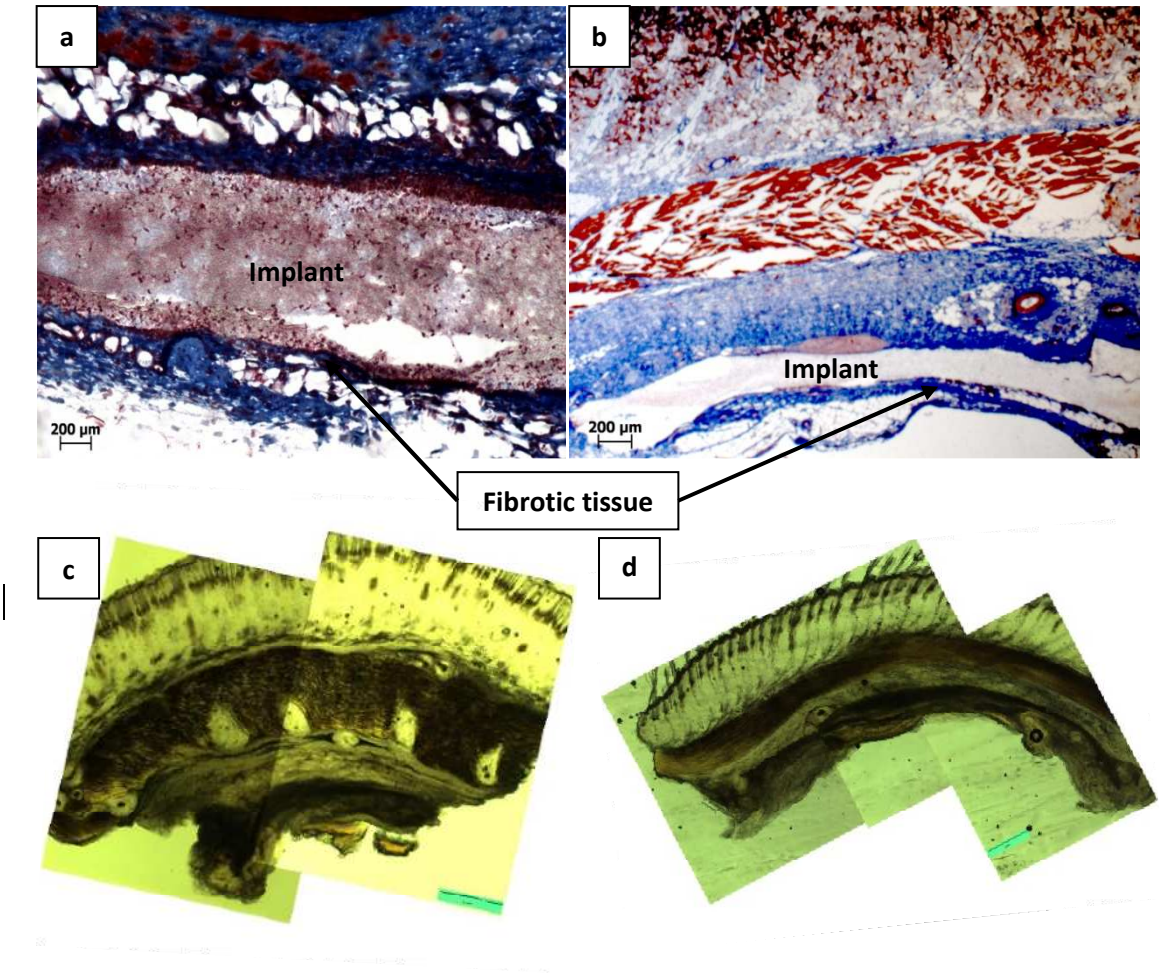

Figure 5.20: *Optical microscope images post Masson's trichrome staining and of samples prior to mounting of Sample R1d ((a) and (c), respectively) and Sample R2b ((b) and (d), respectively).*

A total of 177 frames and 201 frames were collected in SAXS and WAXD line scans, respectively in Sample R1d, and 158 frames and 177 frames, respectively in Sample R2b spanning across water, fibrotic tissue and natural loose connective tissue (see **Figure 5.22** to **Figure 5.25**).

Background correction was carried out to remove any extraneous signal of the radially averaged 2D SAXS patterns. In these 4 week samples, it is difficult to distinguish between fibrotic tissue and the implant as the prominent increase in A_{SAXS} peaks on the left and on the right of the implant is absent. In both samples, the A_{SAXS} peak with the largest value is taken to show the effect of background correction. The raw fibrotic tissue and the resulting background corrected

fibrotic tissue spectra of Sample R1d and Sample R2b are illustrated in **Figure 5.21** (a) and (b), respectively. This helps remove any signal from upstream beamline optics or air-scattering that may overwhelm the signal of interest.

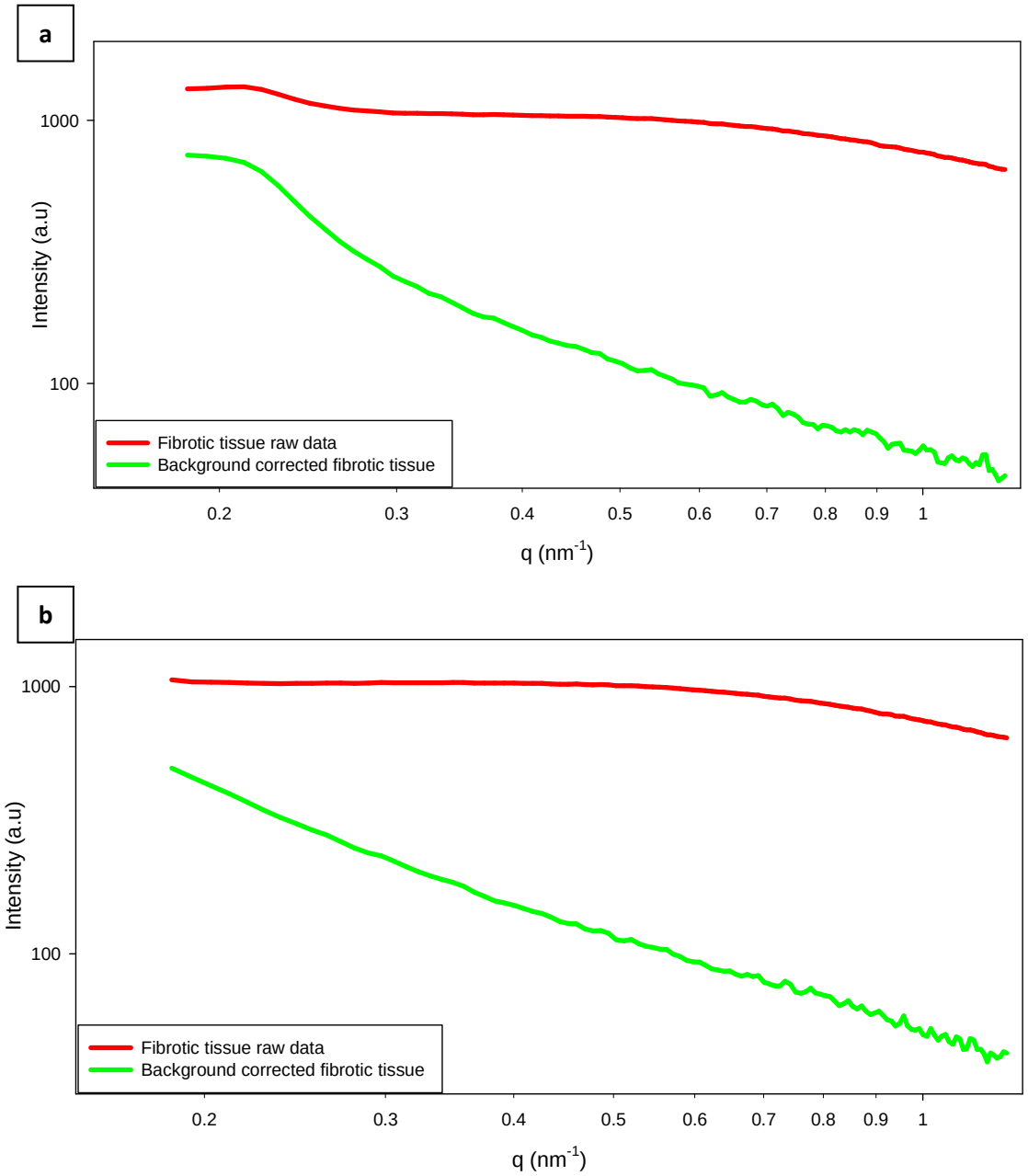

Figure 5.21: *SAXS results of (a) Sample R1d and (b) Sample R2b showing 1D SAXS profile with radial integration of fibrotic tissue raw data and background corrected fibrotic tissue.*

The area under the SAXS curves of Sample R1d and Sample R2b shown in **Figure 5.22** and **Figure 5.23**, respectively, correspond well to the location of water and sample. The area under the WAXD curves of both samples is, however, inconclusive (see **Figure 5.24** and **Figure 5.25**). This could be due to the data processing parameters used. Parameters and limits used for generating the area under the WAXD curves were standardized across samples. As the method used in this work is novel, further analysis using a different set of parameters may be necessary for samples of different time points. Based on the preliminary analysis done above for 4 week samples, it is difficult to further analyse the samples to check for anisotropy and to establish the fibril orientation of fibrotic tissue as well as to establish the intramolecular spacing. This is due to the fact that the fibrotic tissue location cannot be established.

The scattering volume of the sample, however, can be interpreted by comparing the area under SAXS curve with the diode intensity at each point along the line scan (see **Figure 5.26**). The data shows that there is higher x-ray absorbance by the sample as compared to water, in agreement with that seen in Sample R5e.

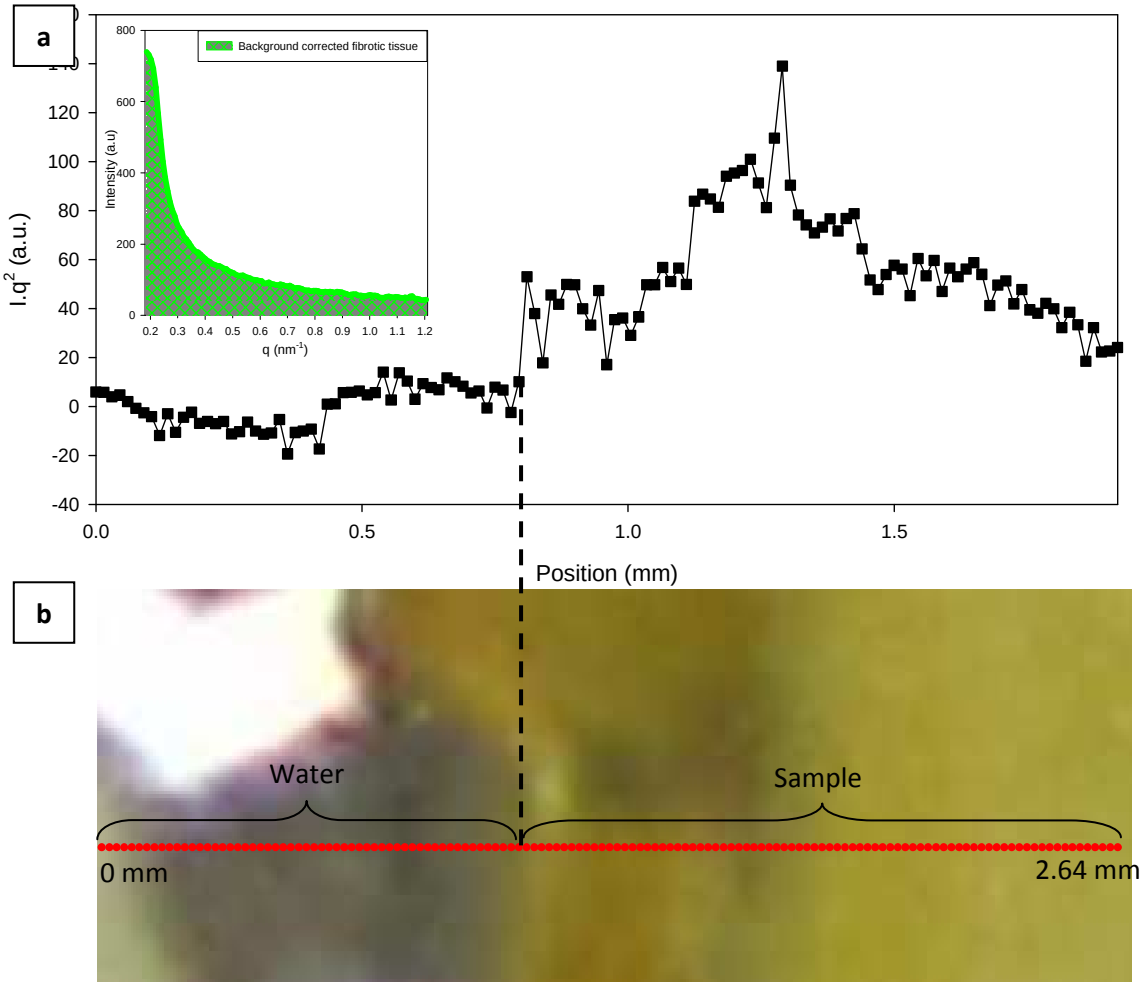

Figure 5.22: *Sample R1d area under the curve across water and fibrotic tissue region (area under the curve for fibrotic tissue shown inset as an example) (a) SAXS line scan and corresponding SAXS line scan location (b) with a beamsize of 15 µm on actual sample (* denotes original implant location).*

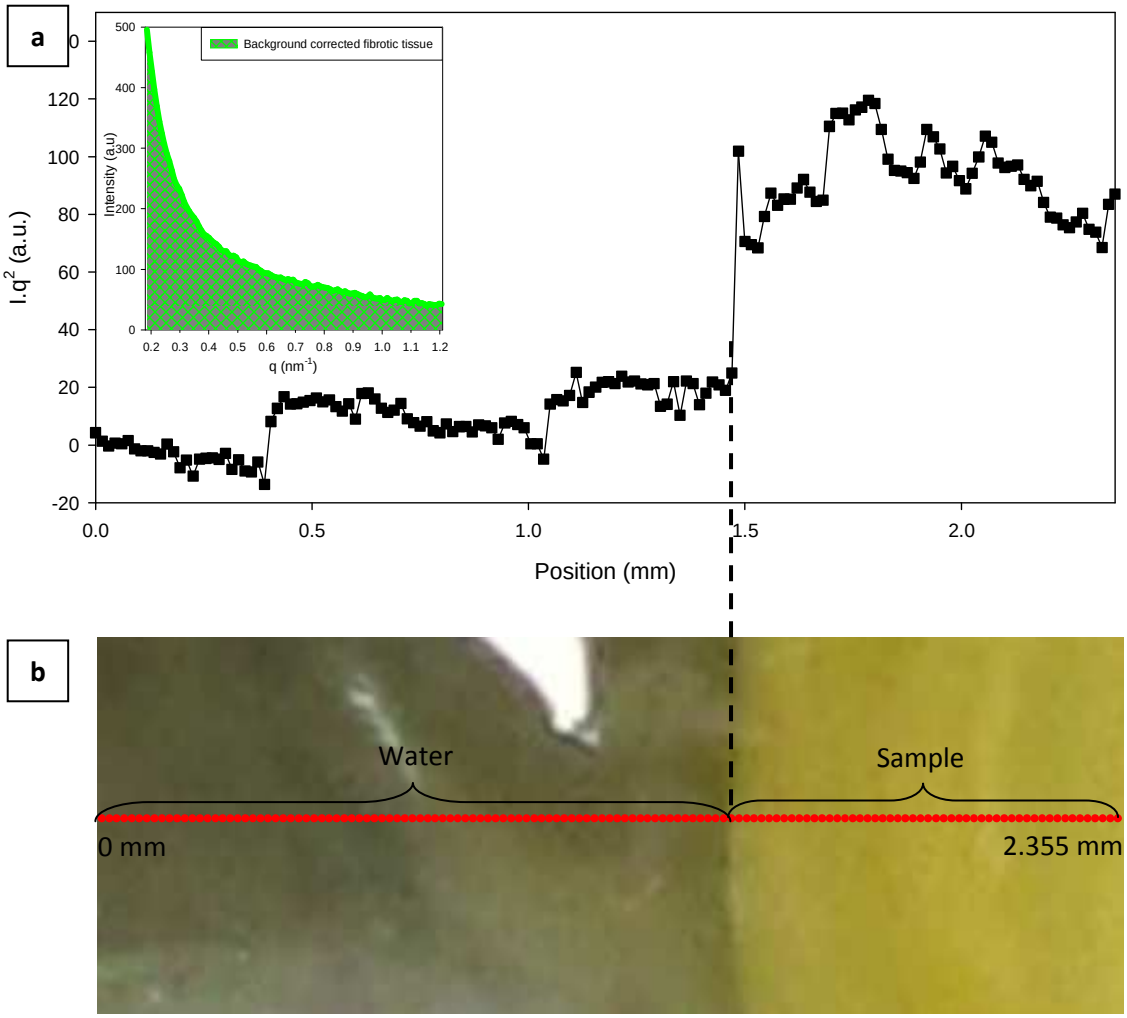

Figure 5.23: *Sample R2b area under the curve across water and fibrotic tissue region (area under the curve for fibrotic tissue shown inset as an example) (a) SAXS line scan and corresponding SAXS line scan location (b) with a beamsize of 15 µm on actual sample (* denotes original implant location).*

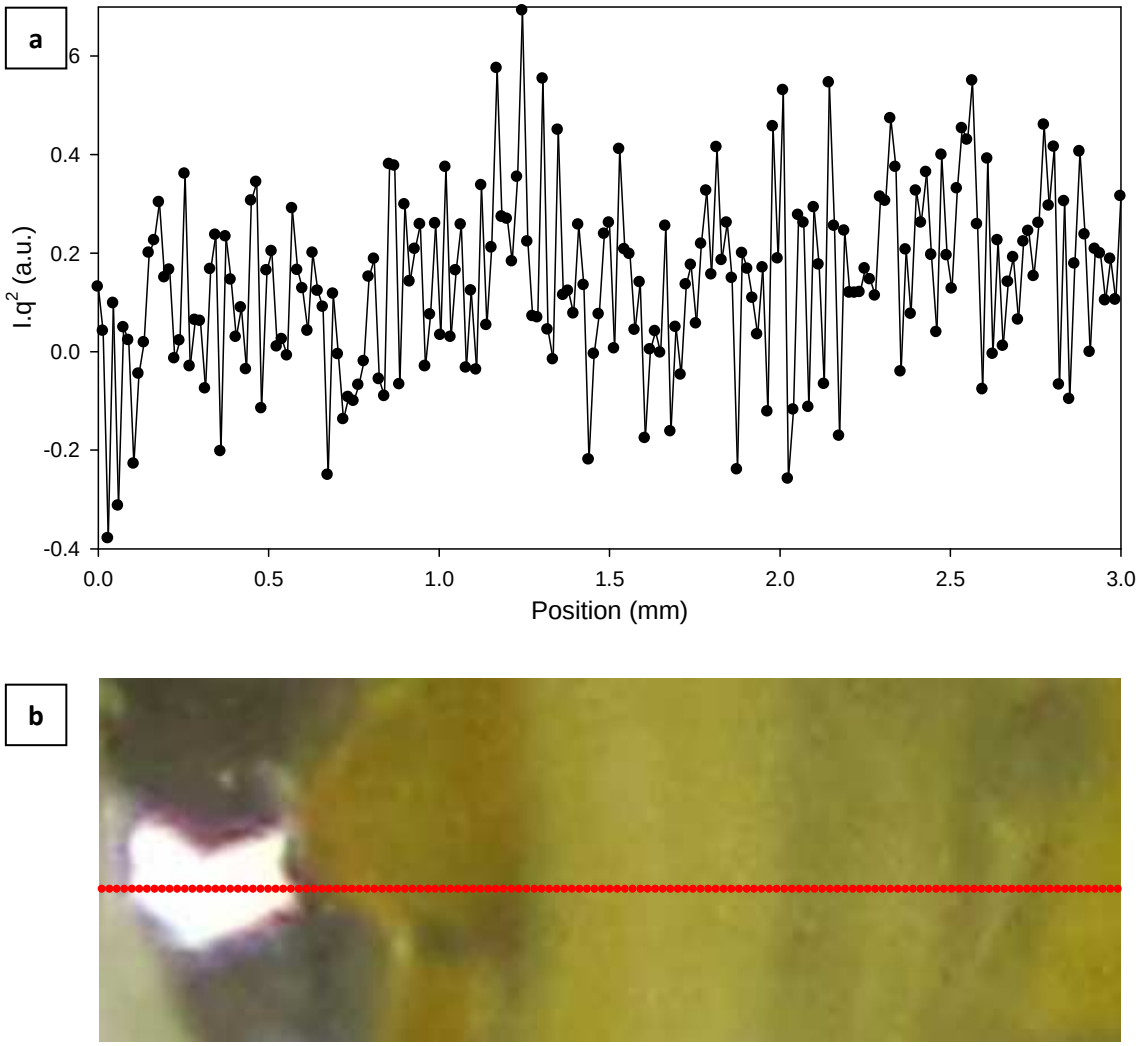

Figure 5.24: *Sample R1d area under the curve across water and fibrotic tissue region (area under the curve for fibrotic tissue shown inset as an example) (a) WAXD line scan and corresponding WAXD line scan location (b) with a beamsize of 15 µm on actual sample (* denotes original implant location).*

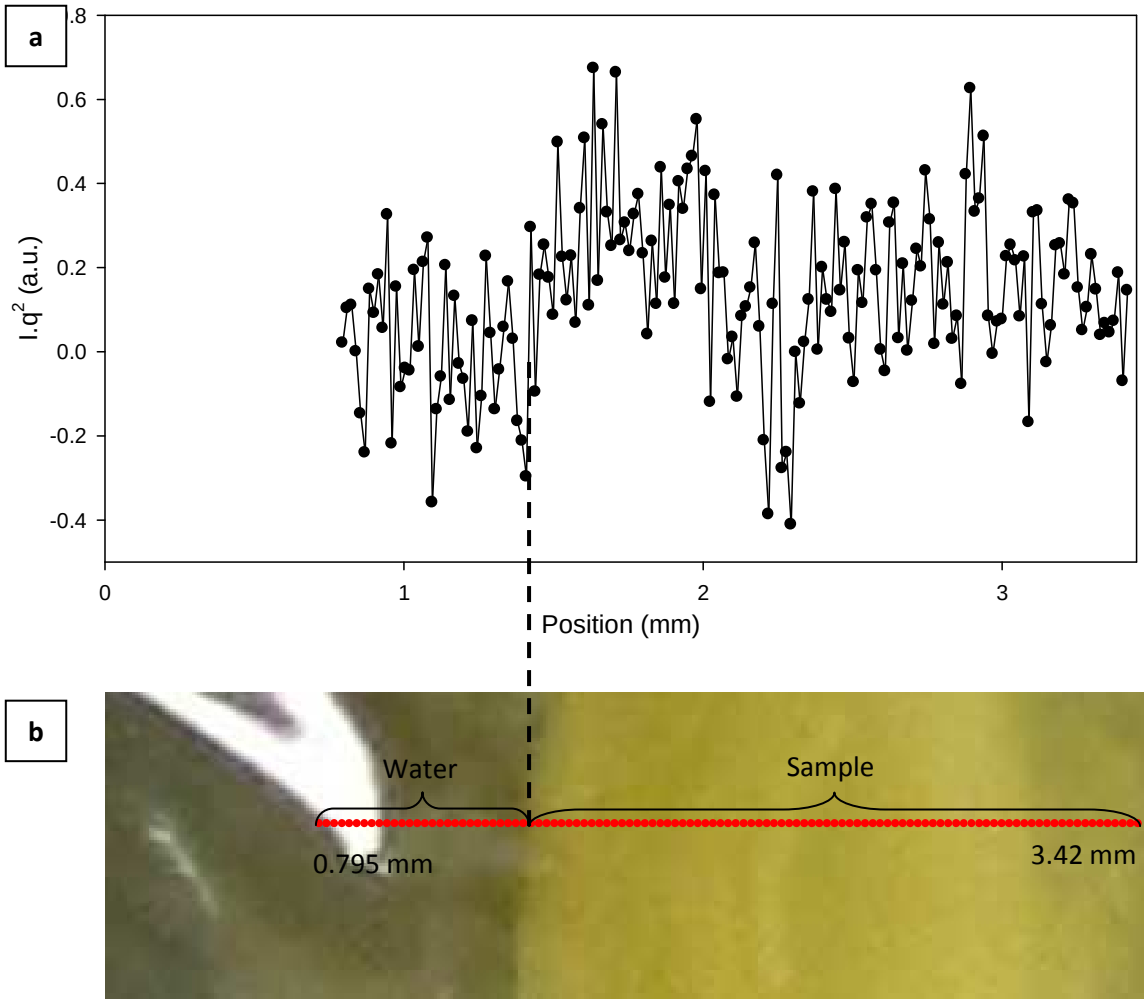

Figure 5.25: *Sample R2b area under the curve across water and fibrotic tissue region (area under the curve for fibrotic tissue shown inset as an example) (a) WAXD line scan and corresponding WAXD line scan location (b) with a beamsize of 15 µm on actual sample (* denotes original implant location).*

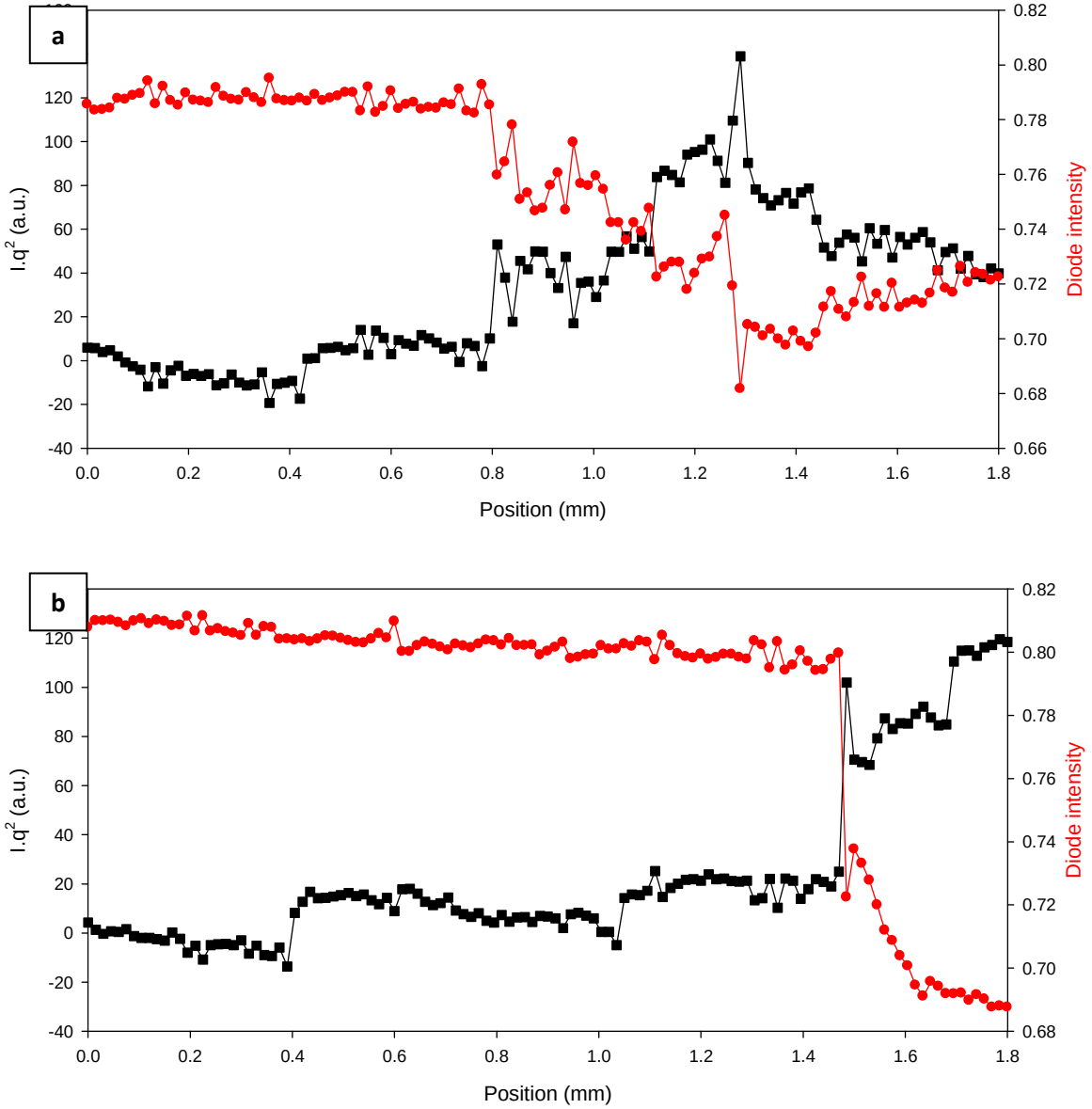

Figure 5.26: *(a) Sample R1d and (b) Sample R2b area under SAXS curves and the diode intensities at each point along the line scans.*

6 Conclusions

The facts resulting from the measurements and data evaluations are as follows:

1. Synchrotron scanning SAXS and WAXD can be used to identify fibrotic tissue location in tissue sections with subcutaneous implants, which is not visible in optical microscopy. Based on the data presented here, this is only true for tissue sections explanted at 9 weeks. The maturity of the fibrotic tissue development is critical in identifying its location.
2. Fibrotic tissue SAXS and WAXD intensities are relatively weak when compared to more conventional and strongly scattering samples like bone and tendon. Hence, careful background correction is crucial to eliminate any extraneous signal (coming from upstream beamline optics, air-scattering or other contributions) which will otherwise overwhelm the signal of interest from the tissue itself.
3. SAXS data indicate that there is some degree of fibrillar orientation in fibrotic tissue.
4. Analysis of WAXD data show that the intra-tropocollagen amino-acid residue spacing of fibrotic tissue is 0.29 nm, which is in agreement with that seen in other collagenous tissue like rat tail tendon, dermis, and whole human skin.
5. SAXS and WAXD intensity comparison show an increase in WAXD intensity accompanied by a relatively constant SAXS intensity, indicating that the tropocollagen molecules within the fibrils may continue to become more and more ordered while the outer fibril area remains constant.
6. While the D-periodicity of fibrotic tissue was yet undetermined, it is clear that it is different from the 67 nm periodicity seen in Type I collagen.

The results presented in this thesis are proof-of-principle that combining SAXS and WAXD with synchrotron radiation microfocus beam in a position-resolved mode is useful for characterizing

the hierarchical structure of fibrotic tissue formed surrounding subcutaneous implants. They serve as a basis for more quantitative models of the fibrotic nanostructure, and can be used as the baseline data to compare with future *in-situ* deformation studies.

7 Future Work

The future work of this project can be divided into two parts:

1. Applying the methods described above on available samples with variable implant type and age-points. This combined with modelling of the SAXS and WAXD diffraction patterns using established physical principles will lead to an important contribution to the knowledge of the nanostructure of fibrotic tissue in wound healing. In terms of the SAXS analysis, the remaining gap is that the D-periodicity of all samples will need to be established. A shape function which is determined from power-law fits can be used to ascertain the shape, size distribution and spatial arrangement of collagen fibrils [132]. This will enable an understanding of the development of fibrotic tissue at different time points as well as the effect of different implant types and implant chemistry on the orientation and molecular spacing of the collagen fibrils. It would also be of interest to establish if a longer implantation time would result in a more ordered fibril arrangement as seen in corneal fibrotic tissue [125].
2. One key area of interest in the study of fibrotic tissue is the biophysical aspect of fibrotic layer development. *In situ* mechanical deformation of the fibrotic tissue and implant interface combined with microfocus synchrotron scanning SAXS and WAXD can be carried out to obtain a quantitative model of the dynamic fibrotic tissue deformation mechanisms under *in vivo* type loading. This can be achieved by utilizing the micro-mechanical tester described in **Section 4.4**. SAXS and WAXD measurements can be done in combination with the application of constant strain in order to understand the micromechanical deformation of the fibrotic layer. Full analysis of the resulting SAXS and WAXD measurements will provide understanding on the effect of micromotion as a function of implant type, chemistry and implantation time. This can be combined with nanoindentation scanning to obtain reduced indentation moduli at locations at/near

where the SAXS and WAXD spectra were collected. This will establish a reference mechanical set using a standard technique (nanoindentation) to benchmark the results from the nanomechanical SAXS data, and will lead to a deeper understanding of the micromechanical properties of the fibrotic layer.

References

1. Gurtner, G., et al., *Wound repair and regeneration.* Nature, 2008. **453**(7193): p. 314-321.
2. Aarabi, S., M.T. Longaker, and G.C. Gurtner, *Hypertrophic scar formation following burns and trauma: new approaches to treatment.* PLoS medicine, 2007. **4**(9): p. e234.
3. Bartoli, C., M. Nadar, and J. Godleski, *Capsule Thickness Correlates With Vascular Density and Blood Flow Within Foreign Body Capsules Surrounding Surgically Implanted Subcutaneous Devices.* Artificial Organs, 2010.
4. Benghuzzi, H., *Cytological evaluation of capsular tissue surrounding TCPL implant in adult rats.* Biomedical sciences instrumentation, 1996. **32**: p. 81.
5. Butler, K., et al., *One year histopathological evaluation of fibrous tissue surrounding TCPL implants using adult rats as a model.* Biomedical sciences instrumentation, 1997. **33**: p. 233.
6. Galante, J.O., et al., *The biologic effects of implant materials.* Journal of Orthopaedic Research, 1991. **9**(5): p. 760-775.
7. Thomson, H., *The fate of the pseudosheath pocket around silicone implants.* Plastic and Reconstructive Surgery, 1973. **51**(6): p. 667.
8. Ferguson, M.W.J. and S. O'Kane, *Scar–free healing: from embryonic mechanisms to adult therapeutic intervention.* Philosophical Transactions of the Royal Society of London. Series B: Biological Sciences, 2004. **359**(1445): p. 839-850.
9. Thompson, S.A., et al., *Mechanical Coupling Between Myofibroblasts and Cardiomyocytes Slows Electric Conduction in Fibrotic Cell Monolayers.* Circulation, 2011. **123**(19): p. 2083-U71.
10. deBakker, J.M.T., et al., *Fractionated electrograms in dilated cardiomyopathy: Origin and relation to abnormal conduction.* Journal of the American College of Cardiology, 1996. **27**(5): p. 1071-1078.
11. Jugdutt, B.I., *Limiting fibrosis after myocardial infarction.* New England Journal of Medicine, 2009. **360**(15): p. 1567-1569.
12. Ueki, T., et al., *Hepatocyte growth factor gene therapy of liver cirrhosis in rats.* Nature Medicine, 1999. **5**(2): p. 226-230.
13. Corrao, G. and S. Aricò, *Independent and combined action of hepatitis C virus infection and alcohol consumption on the risk of symptomatic liver cirrhosis.* Hepatology, 1998. **27**(4): p. 914-919.
14. Bataller, R. and D.A. Brenner, *Liver fibrosis.* J Clin Invest, 2005. **115**(2): p. 209-218.

15. Ginès, P., et al., *Management of cirrhosis and ascites.* New England Journal of Medicine, 2004. **350**(16): p. 1646-1654.
16. King Jr, T.E., A. Pardo, and M. Selman, *Idiopathic pulmonary fibrosis.* The Lancet, 2011.
17. Crouch, E., *Pathobiology of pulmonary fibrosis.* American Journal of Physiology-Lung Cellular and Molecular Physiology, 1990. **259**(4): p. L159-L184.
18. Baum, C.L. and C.J. Arpey, *Normal cutaneous wound healing: clinical correlation with cellular and molecular events.* Dermatologic surgery, 2005. **31**(6): p. 674-686.
19. Paris, O., et al., *A new experimental station for simultaneous X-ray microbeam scanning for small-and wide-angle scattering and fluorescence at BESSY II.* Journal of Applied Crystallography, 2006. **40**: p. s466-s470.
20. Fratzl, P., *Collagen: structure and mechanics*. 2008, New York: Springer. xviii, 506 p.
21. Veis, A., *Collagen fibrillar structure in mineralized and nonmineralized tissues.* Current Opinion in Solid State and Materials Science, 1997. **2**(3): p. 370-378.
22. Scott, J.E., *Supramolecular organization of extracellular matrix glycosaminoglycans, in vitro and in the tissues.* The FASEB journal, 1992. **6**(9): p. 2639-2645.
23. Miller, A., *Collagen - The Organic Matrix of Bone.* Philosophical Transactions of the Royal Society of London Series B-Biological Sciences, 1984. **304**(1121): p. 455-477.
24. Scott, J.E., *Elasticity in extracellular matrix 'shape modules' of tendon, cartilage, etc. A sliding proteoglycan-filament model.* Journal of Physiology-London, 2003. **553**(2): p. 335-343.
25. Parry, D.A.D. and J.M. Squire, *Fibrous proteins: coiled-coils, collagen and elastomers*. Vol. 70. 2005: Academic Press.
26. Wang, J.H.C., Q. Guo, and B. Li, *Tendon Biomechanics and Mechanobiology—A Minireview of Basic Concepts and Recent Advancements.* Journal of Hand Therapy, 2011.
27. Fratzl, P., I. Burgert, and H.S. Gupta, *On the role of interface polymers for the mechanics of natural polymeric composites.* Physical Chemistry Chemical Physics, 2004. **6**(24): p. 5575-5579.
28. Van Der Rest, M. and R. Garrone, *Collagen family of proteins.* The FASEB journal, 1991. **5**(13): p. 2814-2823.
29. Shoulders, M.D. and R.T. Raines, *Collagen structure and stability.* Annual review of biochemistry, 2009. **78**: p. 929.
30. Birk, D.E. and P. Bruckner, *Collagen suprastructures.* Collagen, 2005: p. 185-205.
31. Gelse, K., E. Pöschl, and T. Aigner, *Collagens--structure, function, and biosynthesis.* Advanced drug delivery reviews, 2003. **55**(12): p. 1531-1546.

32. Kadler, K., *Extracellular Matrix 1: fibril forming collagens.* Protein Profile, 1995. **2**: p. 491-619.
33. Hulmes, D.J.S., *Building collagen molecules, fibrils, and suprafibrillar structures.* Journal of structural biology, 2002. **137**(1): p. 2-10.
34. Nagarajan, V., S. Kamitori, and K. Okuyama, *Structure analysis of a collagen-model peptide with a (Pro-Hyp-Gly) sequence repeat.* Journal of biochemistry, 1999. **125**(2): p. 310.
35. Kadler, K.E., et al., *Collagen fibril formation.* Biochemical Journal, 1996. **316**(Pt 1): p. 1.
36. Brodsky, B. and J.A.M. Ramshaw, *The collagen triple-helix structure.* Matrix biology, 1997. **15**(8-9): p. 545-554.
37. Cameron, G., et al., *Structure of type I and type III heterotypic collagen fibrils: an X-ray diffraction study.* Journal of Structural Biology, 2002. **137**(1-2): p. 15-22.
38. Wang, J.H.C., *Mechanobiology of tendon.* Journal of Biomechanics, 2006. **39**(9): p. 1563-1582.
39. Fratzl, P., *Cellulose and collagen: from fibres to tissues.* Current Opinion in Colloid & Interface Science, 2003. **8**(1): p. 32-39.
40. Holmes, D.F., et al., *Corneal collagen fibril structure in three dimensions: structural insights into fibril assembly, mechanical properties, and tissue organization.* Proceedings of the National Academy of Sciences, 2001. **98**(13): p. 7307-7312.
41. Baselt, D.R., J.P. Revel, and J.D. Baldeschwieler, *Subfibrillar structure of type I collagen observed by atomic force microscopy.* Biophysical journal, 1993. **65**(6): p. 2644-2655.
42. Ottani, V., M. Raspanti, and A. Ruggeri, *Collagen structure and functional implications.* Micron, 2001. **32**(3): p. 251-260.
43. Brodsky, B., E.F. Eikenberry, and K. Cassidy, *Unusual collagen periodicity in skin.* Biochimica Et Biophysica Acta, 1980. **621**(1): p. 162-166.
44. Marchini, M., et al., *Differences in the fibril structure of corneal and tendon collagen. An electron microscopy and X-ray diffraction investigation.* Connective Tissue Research, 1986. **15**(4): p. 269-281.
45. Yamamoto, S., et al., *The subfibrillar arrangement of corneal and scleral collagen fibrils as revealed by scanning electron and atomic force microscopy.* Archives of histology and cytology, 2000. **63**(2): p. 127-135.
46. Parry, D.A.D., *The molecular fibrillar structure of collagen and its relationship to the mechanical properties of connective tissue.* Biophysical chemistry, 1988. **29**(1): p. 195-209.

47. Zhang, G., et al., *Development of tendon structure and function: regulation of collagen fibrillogenesis.* J Musculoskelet Neuronal Interact, 2005. **5**(1): p. 5-21.

48. Hwang, W.S., et al., *Collagen fibril structure of normal, aging, and osteoarthritic cartilage.* J Pathol, 1992. **167**(4): p. 425-33.

49. Jeffery, A., et al., *Three-dimensional collagen architecture in bovine articular cartilage.* Journal of Bone & Joint Surgery, British Volume, 1991. **73**(5): p. 795-801.

50. Lamoureux, F., et al., *Proteoglycans: key partners in bone cell biology.* Bioessays, 2007. **29**(8): p. 758-771.

51. Ellis, R., E. Green, and C.P. Winlove, *Structural Analysis of Glycosaminoglycans and Proteoglycans by Means of Raman Microspectrometry.* Connective Tissue Research, 2009. **50**(1): p. 29-36.

52. Prydz, K. and K.T. Dalen, *Synthesis and sorting of proteoglycans.* Journal of cell science, 2000. **113**(2): p. 193.

53. Comper, W.D. and T.C. Laurent, *Physiological function of connective tissue polysaccharides.* Physiological reviews, 1978. **58**(1): p. 255.

54. Hardingham, T. and A. Fosang, *Proteoglycans: many forms and many functions.* The FASEB journal, 1992. **6**(3): p. 861.

55. Wight, T.N., *Versican: a versatile extracellular matrix proteoglycan in cell biology.* Current Opinion in Cell Biology, 2002. **14**(5): p. 617-623.

56. Carrino, D.A., J.M. Sorrell, and A.I. Caplan, *Age-related changes in the proteoglycans of human skin.* Archives of Biochemistry and Biophysics, 2000. **373**(1): p. 91-101.

57. Kirker, K.R., et al., *Glycosaminoglycan hydrogel films as bio-interactive dressings for wound healing.* Biomaterials, 2002. **23**(17): p. 3661-3671.

58. Prathiba, V. and P.D. Gupta, *Cutaneous wound healing: Significance of proteoglycans in scar formation.* Current Science, 2000. **78**(6): p. 697-+.

59. Poole, A.R., *Proteoglycans in health and disease: structures and functions.* Biochemical Journal, 1986. **236**(1): p. 1.

60. Kjellen, L. and U. Lindahl, *Proteoglycans: structures and interactions.* Annual review of biochemistry, 1991. **60**(1): p. 443-475.

61. Robert, L., *Elastin, past, present and future.* Pathologie Biologie, 2002. **50**(8): p. 503-511.

62. Debelle, L. and A.J.P. Alix, *The structures of elastins and their function.* Biochimie, 1999. **81**(10): p. 981-994.

63. Debelle, L. and A.M. Tamburro, *Elastin: molecular description and function.* International Journal of Biochemistry & Cell Biology, 1999. **31**(2): p. 261-272.

64. Daamen, W.F., et al., *Elastin as a biomaterial for tissue engineering.* Biomaterials, 2007. **28**(30): p. 4378-4398.

65. Baldock, C., et al., *Shape of tropoelastin, the highly extensible protein that controls human tissue elasticity.* Proceedings of the National Academy of Sciences, 2011. **108**(11): p. 4322.

66. Alberts B, J.A., Lewis J, et al., *Molecular Biology of the Cell*, in *The Extracellular Matrix of Animals*. 2002, Garland Science: New York.

67. Vrhovski, B. and A.S. Weiss, *Biochemistry of tropoelastin.* European Journal of Biochemistry, 1998. **258**(1): p. 1-18.

68. Hinek, A., *The 67 kDa spliced variant of beta-galactosidase serves as a reusable protective chaperone for tropoelastin*, in *Molecular Biology and Pathology of Elastic Tissues*, D.J. Chadwick and J.A. Goode, Editors. 1995, John Wiley & Sons Ltd: Chichester. p. 185-196.

69. Gacko, M., *Elastin: Structure, properties and metabolism.* Cell Mol Biol Lett, 2000. **5**: p. 327-348.

70. Mithieux, S.M. and A.S. Weiss, *Elastin.* Advances in protein chemistry, 2005. **70**: p. 437-461.

71. Urry, D., et al., *Elastin: a representative ideal protein elastomer.* Philosophical Transactions of the Royal Society of London. Series B: Biological Sciences, 2002. **357**(1418): p. 169-184.

72. Wynn, T.A., *Cellular and molecular mechanisms of fibrosis.* Journal of Pathology, 2008. **214**(2): p. 199-210.

73. Meneghin, A. and C.M. Hogaboam, *Infectious disease, the innate immune response, and fibrosis.* Journal of Clinical Investigation, 2007. **117**(3): p. 530-538.

74. Diegelmann, R. and M. Evans, *Wound healing: an overview of acute, fibrotic and delayed healing.* Front Biosci, 2004. **9**(1): p. 283-289.

75. Anderson, J.M., *Biological responses to materials.* Annual Review of Materials Research, 2001. **31**(1): p. 81-110.

76. Irvin, T.T., *Wound healing : principles and practice*. 1981, London: Chapman and Hall. 221p.,2p. of plates.

77. Ratner, B.D., *Biomaterials science: an introduction to materials in medicine*. 2004: Academic press.

78. Epstein, F.H., A.J. Singer, and R.A.F. Clark, *Cutaneous wound healing.* New England Journal of Medicine, 1999. **341**(10): p. 738-746.

79. Martin, E.A., *Concise medical dictionary*. 6th ed. / [editor: Elizabeth A. Martin] ed. 2002, Oxford: Oxford University Press.

80. Weber, K.T., C.G. Brilla, and J.S. Janicki, *Myocardial fibrosis: functional significance and regulatory factors.* Cardiovascular research, 1993. **27**(3): p. 341.

81. Schwarz, M., *Idiopathic pulmonary fibrosis.* The Western journal of medicine, 1988. **149**(2): p. 199.

82. Michaelson, J.E., S.M. Aguayo, and J. Roman, *Idiopathic Pulmonary Fibrosis.* Chest, 2000. **118**(3): p. 788-794.

83. Hardie, W.D., S.W. Glasser, and J.S. Hagood, *Emerging Concepts in the Pathogenesis of Lung Fibrosis.* American Journal of Pathology, 2009. **175**(1): p. 3-16.

84. Gross, T.J. and G.W. Hunninghake, *Idiopathic pulmonary fibrosis.* New England Journal of Medicine, 2001. **345**(7): p. 517-525.

85. Margaritopoulos, G.A., et al., *Recent advances in the pathogenesis and clinical evaluation of pulmonary fibrosis.* European respiratory review : an official journal of the European Respiratory Society, 2012. **21**(123): p. 48-56.

86. Rosenblum, L.B., *Idiopathic Pulmonary Fibrosis.* 2009.

87. Katzenstein, A.L.A. and J.L. Myers, *Idiopathic pulmonary fibrosis. Clinical relevance of pathologic classification.* American journal of respiratory and critical care medicine, 1998. **157**(4): p. 1301.

88. Díez, J., et al., *Clinical aspects of hypertensive myocardial fibrosis.* Current opinion in Cardiology, 2001. **16**(6): p. 328.

89. Borer, J.S., et al., *Myocardial Fibrosis in Chronic Aortic Regurgitation.* Circulation, 2002. **105**(15): p. 1837-1842.

90. Jugdutt, B.I., *Ventricular remodeling after infarction and the extracellular collagen matrix - When is enough enough?* Circulation, 2003. **108**(11): p. 1395-1403.

91. Daskalopoulos, E.P., B.J.A. Janssen, and W.M. Blankesteijn, *Myofibroblasts in the infarct area: concepts and challenges.* Microscopy and microanalysis : the official journal of Microscopy Society of America, Microbeam Analysis Society, Microscopical Society of Canada, 2012. **18**(1): p. 35-49.

92. Van Rooij, E., et al., *Dysregulation of microRNAs after myocardial infarction reveals a role of miR-29 in cardiac fibrosis.* Proceedings of the National Academy of Sciences, 2008. **105**(35): p. 13027.

93. Weber, K.T., *Cardiac interstitium in health and disease: the fibrillar collagen network.* Journal of the American College of Cardiology, 1989. **13**(7): p. 1637-1652.

94. Whyte, G., et al., *Post-mortem evidence of idiopathic left ventricular hypertrophy and idiopathic interstitial myocardial fibrosis: is exercise the cause?* British journal of sports medicine, 2008. **42**(4): p. 304-305.

95. Lindsay, M.M. and F.G. Dunn, *Biochemical evidence of myocardial fibrosis in veteran endurance athletes.* British journal of sports medicine, 2007. **41**(7): p. 447-452.

96. Weber, K. and C.G. Brilla, *Pathological hypertrophy and cardiac interstitium. Fibrosis and renin-angiotensin-aldosterone system.* Circulation, 1991. **83**(6): p. 1849-1865.

97. Sabbah, H. and S. Goldstein, *Ventricular remodelling: consequences and therapy.* European Heart Journal, 1993. **14**(suppl C): p. 24.

98. Schnee, J.M. and W.A. Hsueh, *Angiotensin II, adhesion, and cardiac fibrosis.* Cardiovascular research, 2000. **46**(2): p. 264-268.

99. Williams, D.F., *The Williams dictionary of biomaterials*. 1999: Liverpool Univ Pr.

100. Wynn, T.A., *Common and unique mechanisms regulate fibrosis in various fibroproliferative diseases.* Journal of Clinical Investigation, 2007. **117**(3): p. 524-529.

101. Butler, K., H. Benghuzzi, and A. Puckett, *Cytological evaluation of the tissue-implant reaction associated with S/C and I/P implantation of ALCAP and HA bioceramics in vivo.* Pathology Research and Practice, 2001a. **197**(1): p. 29-39.

102. Butler, K.R., H.A. Benghuzzi, and A. Puckett, *Morphometric evaluation of tissue-implant reaction associated with ALCAP and TCP bioceramics in vivo.* Journal of Investigative Surgery, 2001b. **14**(3): p. 139-152.

103. Butler, K., H. Benghuzzi, and S. Tucci, *Tissue-implant response following soft tissue implantation of poly-L-lysine coated UHMW-polyethylene into adult male rats.* Biomedical sciences instrumentation, 2001c. **37**: p. 19-24.

104. Butler, K., A. Puckett, and H. Benghuzzi, *Quantitative analysis of the cellular components of the fibrous tissue matrix surrounding ALCAP, HA, and TCP bioceramics using adult male rats as a model.* Biomedical sciences instrumentation, 1999. **35**: p. 267-72.

105. Benghuzzi, H., *Cytological evaluation of capsular tissue surrounding TCPL implant in adult rats.* Biomedical sciences instrumentation, 1996. **32**: p. 81-6.

106. Suska, F., et al., *In Vivo Evaluation of Noble Metal Coatings.* Journal of Biomedical Materials Research Part B-Applied Biomaterials, 2010. **92B**(1): p. 86-94.

107. Park, J.B. and R.S. Lakes, *Biomaterials: an introduction*. 1992: Plenum Pub Corp.

108. Zeplin, P.H., et al., *Phosphorylcholine-Coated Silicone Implants Effect on Inflammatory Response and Fibrous Capsule Formation.* Annals of Plastic Surgery, 2010. **65**(6): p. 560-564.

109. Eltze, E., et al., *Influence of local complications on capsule formation around model implants in a rat model.* Journal of Biomedical Materials Research Part A, 2003. **64A**(1): p. 12-19.

110. Picha, G.J. and R.F. Drake, *Pillared-surface microstructure and soft-tissue implants: Effect of implant site and fixation.* Journal of Biomedical Materials Research, 1996. **30**(3): p. 305-312.

111. Ward, W.K., et al., *The effect of microgeometry, implant thickness and polyurethane chemistry on the foreign body response to subcutaneous implants.* Biomaterials, 2002. **23**(21): p. 4185-4192.

112. Jansson, E., et al., *On the formation of fibrous capsule and fluid space around machined and porous blood plasma clot coated titanium.* Journal of Materials Science-Materials in Medicine, 2001. **12**(10-12): p. 1019-1024.

113. Prasad, B.R., et al., *Controlling cellular activity by manipulating silicone surface roughness.* Colloids and Surfaces B-Biointerfaces, 2010. **78**(2): p. 237-242.

114. Chen, S., et al., *Characterization of topographical effects on macrophage behavior in a foreign body response model.* Biomaterials, 2010. **31**(13): p. 3479-3491.

115. Hilborn, J. and L.M. Bjursten, *A new and evolving paradigm for biocompatibility.* Journal of tissue engineering and regenerative medicine, 2007. **1**(2): p. 110-119.

116. Singer, A.J., J.E. Hollander, and J.V. Quinn, *Evaluation and management of traumatic lacerations.* New England Journal of Medicine, 1997. **337**(16): p. 1142-1148.

117. Aarabi, S., et al., *Mechanical load initiates hypertrophic scar formation through decreased cellular apoptosis.* Faseb Journal, 2007. **21**(12): p. 3250-3261.

118. Costa, A.M.A., et al., *Mechanical forces induce scar remodeling - Study in non-pressure-treated versus pressure-treated hypertrophic scars.* American Journal of Pathology, 1999. **155**(5): p. 1671-1679.

119. Martin, P. and S.M. Parkhurst, *Parallels between tissue repair and embryo morphogenesis.* Development, 2004. **131**(13): p. 3021-3034.

120. Colwell, A.S., M.T. Longaker, and H.P. Lorenz, *Fetal wound healing.* Frontiers in Bioscience, 2003. **8**(Cited June 27, 2003): p. 1240-1248.

121. Khorasani, H., et al., *A Quantitative Approach to Scar Analysis.* American Journal of Pathology, 2011. **178**(2): p. 621-628.

122. Cócera, M., et al., *Characterisation of skin states by non-crystalline diffraction.* Soft Matter, 2011. **7**(18): p. 8605-8611.

123. Brodsky, B. and J.A.M. Ramshaw, *Collagen organization in an oriented fibrous capsule.* International Journal of Biological Macromolecules, 1994. **16**(1): p. 27-30.

124. Brodsky, B. and E.F. Eikenberry, *Characterization of fibrous forms of collagen.* Methods in enzymology, 1982. **82**: p. 127-174.

125. Rawe, I.M., et al., *Structure of corneal scar tissue: an X-ray diffraction study.* Biophysical journal, 1994. **67**(4): p. 1743-1748.

126. Delfour, C., et al., *RCL2, a new fixative, preserves morphology and nucleic acid integrity in paraffin-embedded breast carcinoma and microdissected breast tumor cells.* Journal of Molecular Diagnostics, 2006. **8**(2): p. 157-169.

127. Kiernan, G.L.K.J.A., ed. *Education Guide - Special Stains and H & E*. 2 ed. 2010, Dako North America: Carpinteria, California.

128. Faoláin, E.Ó., et al., *Raman spectroscopic evaluation of efficacy of current paraffin wax section dewaxing agents.* Journal of Histochemistry & Cytochemistry, 2005. **53**(1): p. 121.

129. Nobelprize.org. *The Nobel Prize in Physics 1901*. 1901 25 Mar 2012]; Available from: http://www.nobelprize.org/nobel_prizes/physics/laureates/1901/.

130. Nobelprize.org. *The Nobel Prize in Physics 1914*. 1914 25 Mar 2012]; Available from: http://www.nobelprize.org/nobel_prizes/physics/laureates/1914/.

131. Cullity, B.D., *Elements of x-ray diffraction*. 2d ed. Addison-Wesley series in metallurgy and materials. 1978, Reading, Mass.: Addison-Wesley Pub. Co. xii, 555 p.

132. Guinier, A., *X-ray crystallographic technology*. 1952, London,: Hilger and Watts, Hilger Division. 330 p.

133. Nobelprize.org. *The Nobel Prize in Physics 1915*. 1915 25 Mar 2012]; Available from: http://www.nobelprize.org/nobel_prizes/physics/laureates/1915/.

134. Fratzl, P., et al., *Position-resolved small-angle X-ray scattering of complex biological materials.* Journal of Applied Crystallography, 1997. **30**(5): p. 765-769.

135. Lichtenegger, H., et al., *Variation of Cellulose Microfibril Angles in Softwoods and Hardwoods--A Possible Strategy of Mechanical Optimization.* Journal of Structural Biology, 1999. **128**(3): p. 257-269.

136. Zizak, I., et al., *Investigation of bone and cartilage by synchrotron scanning-SAXS and-WAXD with micrometer spatial resolution.* Journal of Applied Crystallography, 2000. **33**(3): p. 820-823.

137. Paris, O., et al., *Analysis of the hierarchical structure of biological tissues by scanning X-ray scattering using a micro-beam.* Cellular and molecular biology (Noisy-le-Grand, France), 2000. **46**(5): p. 993.

138. Paris, O., et al., *The internal structure of single carbon fibers determined by simultaneous small-and wide-angle scattering.* Journal of Applied Crystallography, 2000. **33**(3): p. 695-699.

139. Paris, O., *From diffraction to imaging: New avenues in studying hierarchical biological tissues with x-ray microbeams (Review).* Biointerphases, 2008. **3**(2).

140. Balta\-Calleja, F.J. and C.G. Vonk, *X-ray scattering of synthetic polymers*. 1989: Elsevier.

141. Glatter, O. and O. Kratky, *Small angle x-ray scattering*. 1982, London: Academic Press.

142. Heidelbach, F., C. Riekel, and H.R. Wenk, *Quantitative texture analysis of small domains with synchrotron radiation X-rays.* Journal of Applied Crystallography, 1999. **32**(5): p. 841-849.

143. Ramachandran, G.N., *Molecular Structure of Collagen.* International review of connective tissue research, 1963. **1**: p. 127-82.

144. Rich, A. and F.H. Crick, *The molecular structure of collagen.* Journal of molecular biology, 1961. **3**: p. 483-506.

145. Sasaki, N. and S. Odajima, *Stress-strain curve and Young's modulus of a collagen molecule as determined by the X-ray diffraction technique.* Journal of Biomechanics, 1996. **29**(5): p. 655-658.

146. Woodhead-Galloway, J. and P.A. Machin, *Modern theories of liquids and the diffuse equatorial X-ray scattering from collagen.* Acta Crystallographica Section A: Crystal Physics, Diffraction, Theoretical and General Crystallography, 1976. **32**(3): p. 368-372.

147. McBride, D.J., et al., *Altered collagen structure in mouse tail tendon lacking the [alpha] 2 (I) chain1.* Journal of molecular biology, 1997. **270**(2): p. 275-284.

148. Müller, B., et al., *Scanning x-ray scattering: Evaluating the nanostructure of human tissues.* Eur J Nanomed 2010; 3: 30, 2010. **3**.

149. Prewitt, C., et al., *New opportunities in synchrotron X-ray crystallography.* Science, 1987. **238**(4825): p. 312-319.

150. Ltd, D.L.S. *Components of the machine*. 2012 24/08/2010 [cited 2012 15/05/2012]; Available from: http://www.diamond.ac.uk/Home/Technology/Components.html.

151. Gupta, H.S., et al., *Cooperative deformation of mineral and collagen in bone at the nanoscale.* Proceedings of the National Academy of Sciences of the United States of America, 2006. **103**(47): p. 17741-17746.

152. Gourrier, A., et al., *Scanning X-ray imaging with small-angle scattering contrast.* Journal of Applied Crystallography, 2007. **40**: p. S78-S82.

153. Burger, C., et al., *Lateral packing of mineral crystals in bone collagen fibrils.* Biophysical journal, 2008. **95**(4): p. 1985-1992.

154. Bunk, O., et al., *Multimodal x-ray scatter imaging.* New Journal of Physics, 2009. **11**.

155. Boote, C., et al., *Collagen fibrils appear more closely packed in the prepupillary cornea: Optical and biomechanical implications.* Investigative Ophthalmology & Visual Science, 2003. **44**(7): p. 2941-2948.

156. Quantock, A.J., et al., *Small-angle fibre diffraction studies of corneal matrix structure: a depth-profiled investigation of the human eye-bank cornea.* Journal of Applied Crystallography, 2007. **40**: p. S335-S340.

157. Malmqvist, J., R. Axelsson, and M. Johansson. *A comparative analysis of the theory of inventive problem solving and the systematic approach of pahl and beitz*. 1996.

158. Fernández, M., et al., *Small-angle x-ray scattering studies of human breast tissue samples.* Physics in medicine and biology, 2002. **47**: p. 577.

159. Sidhu, S., et al., *Mapping structural changes in breast tissue disease using x-ray scattering.* Medical physics, 2009. **36**: p. 3211.

160. Sidhu, S., et al., *Classification of breast tissue using a laboratory system for small-angle x-ray scattering (SAXS).* Physics in medicine and biology, 2011. **56**: p. 6779.

161. Conceição, A.L.C., M. Antoniassi, and M.E. Poletti, *Analysis of breast cancer by small angle X-ray scattering (SAXS).* Analyst, 2009. **134**(6): p. 1077-1082.

162. Hayes, S., et al., *Riboflavin/UVA Collagen Cross-Linking-Induced Changes in Normal and Keratoconus Corneal Stroma.* PloS one, 2011. **6**(8): p. e22405.

163. Quantock, A.J., et al., *A synchrotron x-ray diffraction study of developing chick corneas.* Biophysical journal, 1998. **74**(2): p. 995-998.

164. Hammersley, A., *FIT2D: An introduction and overview.* European Synchrotron Radiation Facility Internal Report ESRF97HA02T, 1997.

165. Purslow, P.P., T.J. Wess, and D.W.L. Hukins, *Collagen orientation and molecular spacing during creep and stress-relaxation in soft connective tissues.* Journal of Experimental Biology, 1998. **201**(1): p. 135-142.

166. Pauling, L. and R.B. Corey, *The structure of fibrous proteins of the collagen-gelatin group.* Proceedings of the National Academy of Sciences of the United States of America, 1951. **37**(5): p. 272.

167. Rowlands, C. and S. Elliott, *Automated algorithm for baseline subtraction in spectra.* Journal of Raman Spectroscopy, 2010.

168. Movasaghi, Z., S. Rehman, and I.U. Rehman, *Raman spectroscopy of biological tissues.* Applied Spectroscopy Reviews, 2007. **42**(5): p. 493-541.

169. Połomska, M., et al., *Fourier Transform Near Infrared Raman Spectroscopy in Studies on Connective Tissue.* Acta Physica Polonica A, 2010. **118**: p. 136-140.

170. Frushour, B.G. and J.L. Koenig, *Raman-scattering of collagen, gelatin, and elastin.* Biopolymers, 1975. **14**(2): p. 379-391.

171. Wang, Y.N., C. Galiotis, and D.L. Bader, *Determination of molecular changes in soft tissues under strain using laser Raman microscopy.* Journal of Biomechanics, 2000. **33**(4): p. 483-486.

Appendices

Appendix A: SAXS and WAXD Data Analysis using FIT2D and SigmaPlot

FIT2D (version 12.077) an open-source software was used in the course of this study to evaluate the SAXD and WAXD measurements. 2D SAXS patterns were exported in the form of a chiplot (.chi) for further analysis using SigmaPlot. Beam centre was calculated by “circle coordinate” calibration by using silver behenate in SAXS configuration and silicon in WAXD configuration. This requires careful selection of at least 3 points on the diffraction ring to produce an accurate beam centre which will be used for the analysis of all SAXS and WAXD data. Sample to detector distance calibration was done using rat tail tendon. The integration of all 2D patterns was done using the “cake” function by defining the start and end azimuth angles (degrees), the inner and outer radial limit (pixels), as well as the number of azimuthal and radial bins. The integrated data is saved as a chiplot wherein the first column corresponds to the q-spacing or azimuth angle (depending on the type of integration performed) and the second column is the intensity in arbitrary units. Data processing was then performed using SigmaPlot by importing the chiplots. All data was corrected for background followed by the appropriate transformation and fitting.

Appendix B: Raman Spectroscopy Analysis

Raman scattering analysis was carried out on one scaffold in the form of a thin sheet (10 mm x 10 mm x 3mm) with a collagen-NDGA (nordihydroguaiaretic acid) implant surrounded by fibrotic tissue in rat. Optical microscope images post Masson's trichrome staining are illustrated in **Figure B.1**. Tissue section was explanted 28 days after implantation. The tissue section, embedded in paraffin wax, was provided by Dr Krishna Burugapalli from the Brunel Institute of Bioengineering, Brunel University. Wax was removed using the protocol described earlier in **Table 4.4**. Sample was then dried overnight prior to Raman spectroscopy. Raman spectra were collected using Nicolet Almega XR dispersive Raman spectrometer (Thermo Fisher Scientific Inc, WI USA) with an integrated Olympus BX-51 microscope using 10x objective. Sample was placed on a stainless steel substrate on a motor-controlled stage, and manually focussed onto the dermis, fibrotic tissue and collagen-NDGA implant. A 785 nm laser wavelength was used as the excitation source. Laser power was set at 100%, while the exposure time and number of exposures were set at 1 second and 128, respectively. Background spectra was collected and automatically subtracted from the sample spectra. OMNIC software (v.7.2a Thermo Electron Corporation) was used to collect spectra and configure Raman machine settings.

The resulting Raman spectra of the dermis, fibrotic tissue and collagen-NDGA implant are shown in **Figure B.2**. High florescence was noted in Raman signal which required automated baseline subtraction. A cubic polynomial method baseline subtraction method was adapted from Rowlands et al. [167] and applied to all three spectra. Rowlands et al. proposed that values of the first derivative, i.e. the slope of the spectrum will change significantly in areas of interest in a spectrum, for example, near a peak. In These values will change slowly in areas that are just due to baseline drift. The absolute value of the second derivative at any given point will indicate if the point is a likely peak; wherein a large value indicates a slope that is varying rapidly and points to a feature of interest in the spectrum. A small absolute value of the second derivate indicates a

drift in the baseline. Baseline subtraction was done by first applying a running average of the original spectrum, followed by the generation and smoothening of the first derivative. The first derivative is then smoothened out by once again applying a running average. This process is repeated for the second derivative. The smoothening of the spectra and the first derivative is important to avoid producing a second derivative which is dominated by noise. Peaks were then identified by looking at the negative peak of the second derivative at a predetermined threshold level, such that points with an absolute second derivative value larger than the threshold value are classified as part of a peak and values below the threshold as part of the baseline. Finally, a simple cubic polynomial in which the start and end points are known is used and is expressed as:

$$y = ax^3 + bx^2 + cx + d$$

where x = 0 is the start of the gap and x = 1 is the end of the gap. The start and end derivatives are taken by averaging derivatives on the baseline close to the gap, assuming that any changes in the first derivative of the baseline are negligible over short distances. The starting point, starting first derivative, ending point and ending first derivative are expressed as *p, q, r* and *s*, respectively. The gap width in the spectrum is denoted as *n*. Parameters *a, b, c* and *d* can then be solved as follows:

$$d = p$$

$$c = qn$$

$$a = sn - 2(r - p - qn) - qn$$

$$b = r - p - qn - a$$

Fitting this cubic polynomial results in the complete baseline subtraction from the original spectrum and leads to a corrected spectrum [167] (see **Figure B.2** (b)). Peak positions and

intensity differences were seen between fibrotic tissue and surrounding tissue, as summarized in **Table B.1**.

While these results were promising, there was a major concern that they were not reproducible. Preliminary Raman spectroscopy tests were done using bovine Achilles tendon in order to show sample reproducibility and effectiveness of the baseline subtraction method used above. Raman spectra were collected on the same sample using the same machine parameters. Data was collected over a period of several days to check for machine stability. Baseline subtraction was applied to the raw Raman spectra. The results are shown in **Figure B.3**. While the baseline subtraction method successfully produced useable spectra, repeated Raman scattering data collection of Bovine Achilles tendon clearly does not show reproducibility. Is it unclear if this is due to a machine issue.

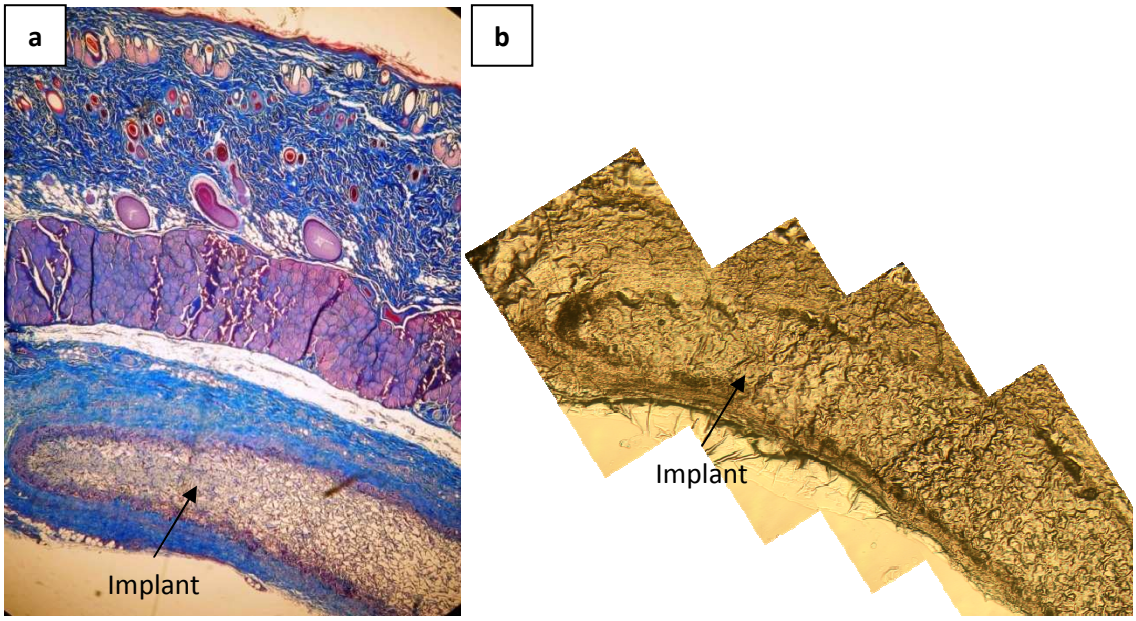

***Figure B.1**: Optical microscope image of the tissue section with collagen-NDGA implant; (a) 4x objective post Masson's trichrome staining (image provided by Dr Krishna Burugapalli), and (b) optical microscope image of a 30 µm section at 5x objective.*

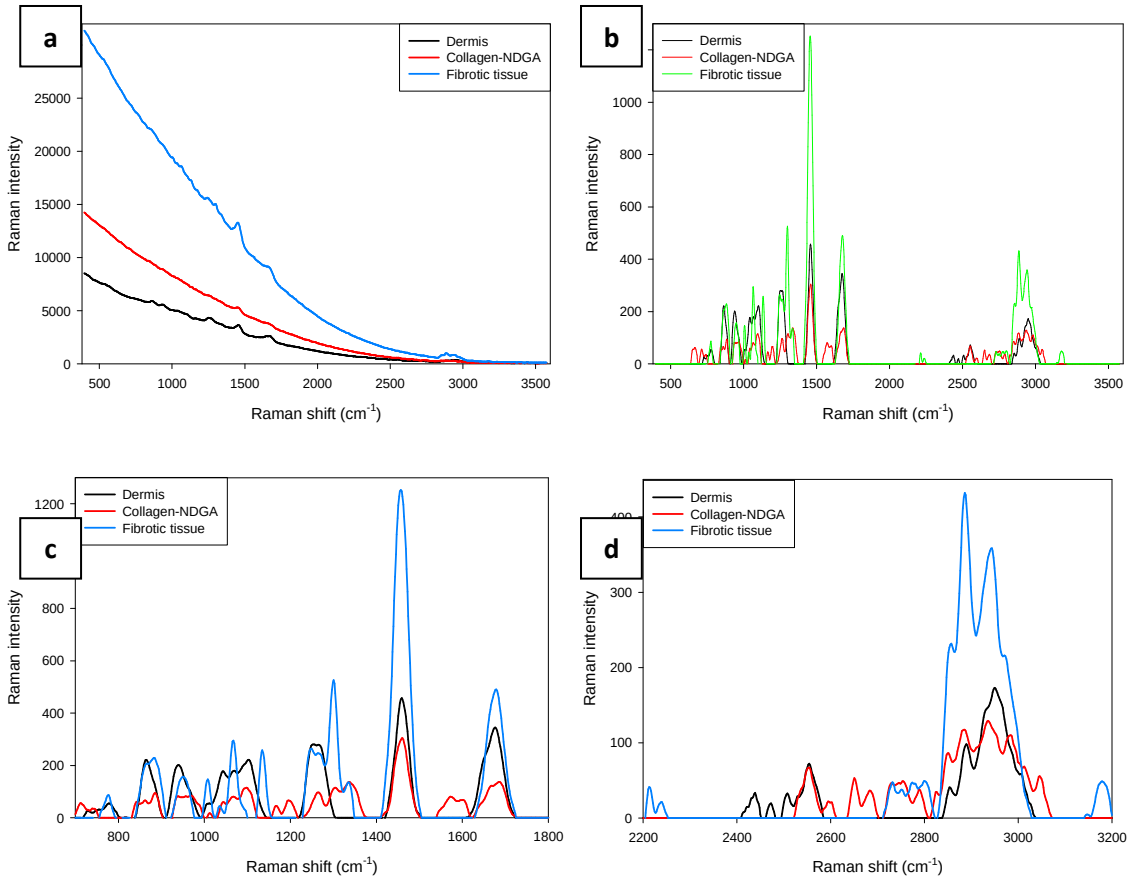

***Figure B.2**: (a) Raw Raman spectra of skin tissue, collagen-NDGA implant and fibrotic layer; (b), (c) and (d) are spectra post-baseline subtraction.*

***Table B.1:** Peaks and assignments in FL and skin tissue [168-169] (ν – stretching; δ – deformation)*

Fibrotic layer	Skin tissue
866 - 884 cm^{-1} (ν(C–C) of proline ring; Collagen I)	864 cm^{-1} (C-C stretching)
949 cm^{-1} (ν(CH_3) symmetric)	940 cm^{-1} (C-C stretch backbone)
1067 cm^{-1} (Proline (collagen assignment))	1044 -1096 cm^{-1} (Proline ; $\nu(C–C)_{trans}$ phospholipids)
1248 - 1300 cm^{-1} (Amide III)	1254 cm^{-1} (Amide III)
1456 cm^{-1} (δ(CH_2); δ(CH_3))	1458 cm^{-1} (δ(CH_2); δ(CH_3))
1678 cm^{-1} (Amide I)	1676 cm^{-1} (Amide I)
2885 cm^{-1} (ν(CH_3)symmetric)	2853 cm^{-1} (ν(CH_2)symmetric)
2941 cm^{-1} (ν(CH_2); ν(CH_3))	2949 cm^{-1} (ν(CH_2); ν(CH_3))

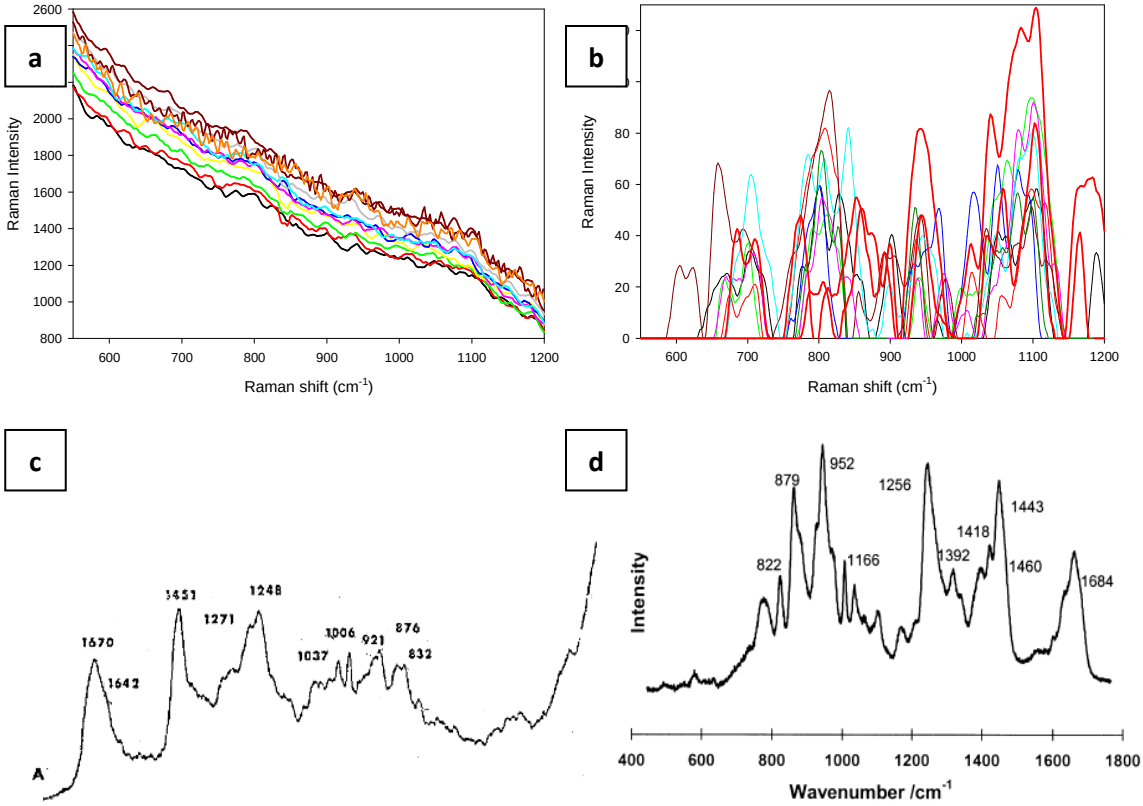

***Figure B.3**: (a) Raw Raman spectra of bovine Achilles tendon, (b) baseline subtracted spectra, and reference spectrum of (c) bovine Achilles tendon [170] and (d) rat tail tendon [171].*

Appendix C: School of Engineering and Materials Science Research Student Poster Presentation 2010

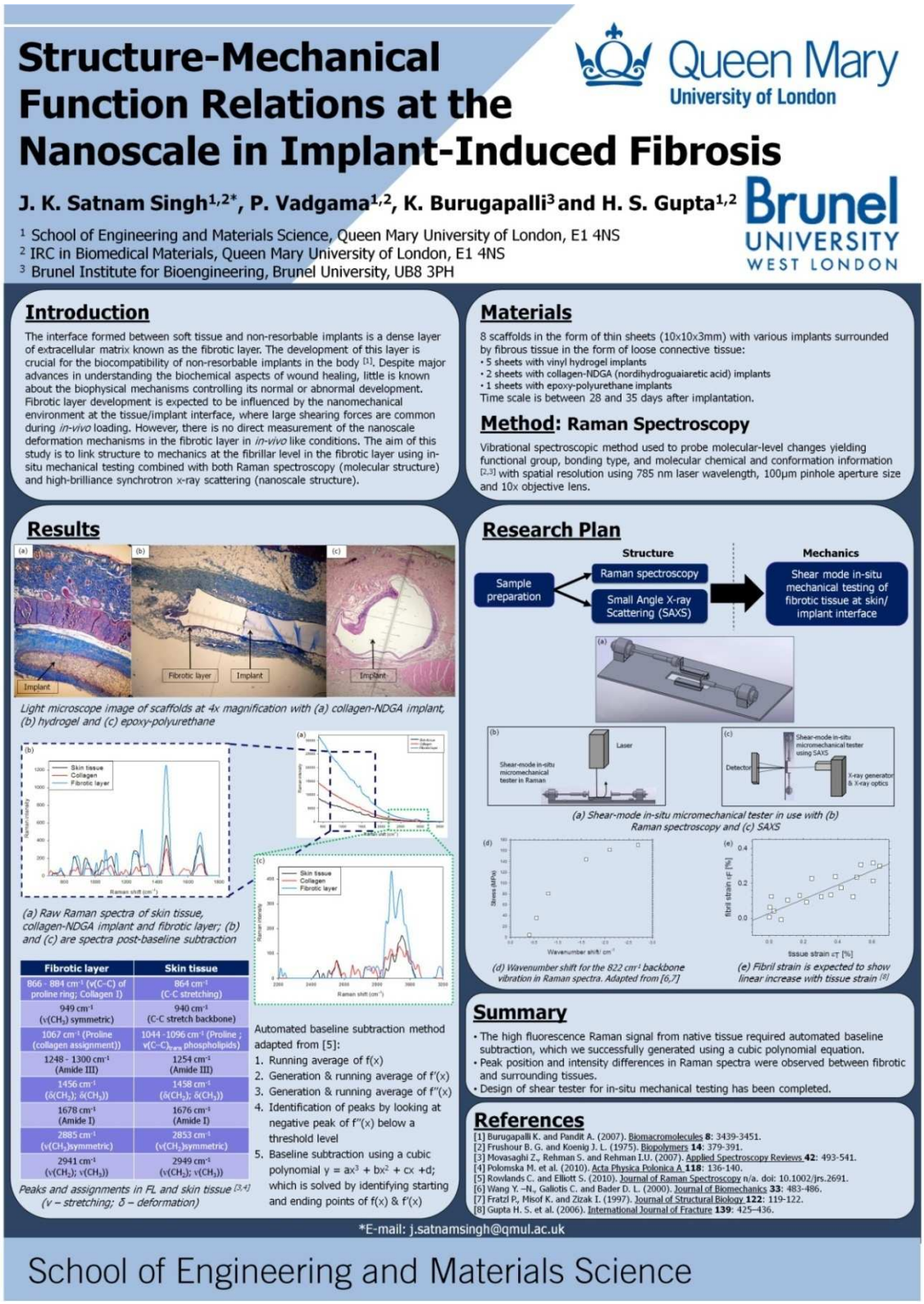

***Figure C.1**: Poster submitted for School of Engineering and Materials Science Research Student Poster Presentation 2010.*